UNIVERSITÀ DEGLI STUDI DI TORINO
DIPARTIMENTO DI FISICA
Scuola di Scienze della Natura

Tesi di Laurea Magistrale in Astrofisica e Fisica Teorica

Magnetic Fields in the Solar Corona: Diagnostics from polarimetric observations of Total Eclipse

Candidata: **Jessica Girella**
Relatore: **Dott. Silvano Fineschi**
Correlatori: **Dott. Alessandro Bemporad, Dott. Gerardo Capobianco**
Controrelatore: **Dott. Silvano Massaglia**

Anno Accademico 2013-2014

To my beloved Rudy, Emanuele and to my family.
You are my greatest strength.

Abstract

Magnetic fields are known to govern much of the morphology and the dynamics of the solar corona. The most direct diagnostic of the magnetic field, that is currently known, is the measurement of linear polarization in the forbidden spectral emission lines in the wavelength range of visible-light. Emission profiles from these transitions contain information on physical parameters such as temperature, density, plasma bulk velocities and turbulence. Observations of polarized light in coronal spectral lines carry also information about the strength and orientation of the magnetic field vector. A good choice for magnetic field investigations is Fe XIV line at 530.3 nm because of the good compromise between line intensity and the degree of polarization relative to the continuum background of the K-corona. This background is due to Thomson scattering of photospheric light by coronal electrons. The coronal FeXIV line is linearly polarized by resonance scattering of the photospheric light anisotropically illuminating coronal Fe^{+13} ions. In the presence of a magnetic field, the FeXIV line linear polarization is modified by the "saturated"Hanle effect. This effect changes the direction of the polarization vector depending on the angle between the magnetic field vector and the local solar vertical of the scattering volume. The linear polarization of the FeXIV forbidden emission interpreted in terms of "saturated" Hanle effect can be used as a diagnostics tool of the coronal magnetic field.

The overall goal of my thesis is to apply this diagnostics to the polarized coronal images of the FeXIV line-emission acquired by the INAF-Turin Coronal Magnetograph ("CorMag") during the total solar eclipse of 11/07/2010 in Tatakoto Atoll (French Polynesia). This thesis work includes the post eclipse calibration and the implementation of the control software of the CorMag instrument, in view of its integration to the Lomnicky Zeiss coronagraph (Slovakia). CorMag comprises a linear polarimeter and a Lyot filter optimized for the spectropolarimetry of the FeXIV emission line ("E-corona line emission").

The interpretation of the line linear polarization through the Hanle effect permits to map the topology and the dynamics of the coronal magnetic field. Some insight into magnetic field topology is provided in this thesis by the comparison between the observed line polarization and that one computed from models of the coronal magnetic fields, derived from force-free measurements of the photospheric field extrapolated up to the coronal levels with a numerical code for forward-modelling ("FORWAD") developed by the High Alti-

tude Observatory. According to the Thomson scattering theory, the polarization vector of the K-corona continuum emission is insensitive to the magnetic field and is tangent to the solar limb. This characteristic of the Thomson scattering was exploited to calibrate out all the instrumental and environmental background from polarized acquired images. The linear polarization vector of the E-corona emission-line is directed radially (magnetic dipole emission). As predicted by the Hanle effect theory, variations from radial direction of the linear polarization vector are due to the presence of the magnetic field.

This thesis reports the first detection of the Hanle effect in a coronal forbidden line-emission observed during an eclipse with an electro-optical spectro-polarimeter. From the analysis of the polarization vector image have been derived unique information about the topology of the magnetic field.

In particular, the result of this thesis work shows the presence of the Hanle effect in the line-emission of the Fe^{+13} ions in the coronal plasma surrounding a prominence. This information can be used to discriminate different models of magnetic field in solar prominences.

Contents

List of Figures

Chapter 1

The Sun

1.1 Introduction

The Sun is the nearest star to the Earth, the centre of our solar system and one of the 100,000 million stars, which goes to make up our galaxy, the Milky Way. Thanks to its proximity, the Sun is the star we know best and its study has contributed to the understanding of the mechanisms that govern the Universe.

It is placed from Earth at a mean distance of $149 \cdot 10^6$ km, the so-called *astronomical unit* (AU), which sets the scale for measuring distances all across the solar system.

The Sun is a Population I, or heavy-element-rich, star. The formation of the Sun may have been triggered by shock-waves from one or more nearby supernovae. Chemically it is composed primarily of hydrogen (70%)and helium (28%), with traces of heavier elements including oxygen, carbon, neon and iron, among others (2%). From a spectroscopic point of view, using the Harvard classification, the Sun is a star of class G2V, where G2 indicates that its surface temperature is of approximately 5778 K, and V indicates that the Sun, like most stars, is a main-sequence star, and thus generates its energy by nuclear fusion of hydrogen nuclei into helium [Ferrari, 2011].

In its core, the Sun fuses 620 million metric tons of hydrogen each second. As the core hydrogen is used up, the nuclear burning will take place in a growing shell surrounding the exhausted core. The star will continue to grow brighter and when the burning shell approaches the surface, the Sun will enter the red giant phase, producing an enormous shell that may extend as far as Venus or even Earth. Fortunately, the Sun will require billions of years to reach this state. After this phase it will blow up into a planetary

nebula. The final naked core temperature will be over 100,000 K, after which the remnant will cool towards a white dwarf. The planetary nebula will disperse in about 10,000 years, but the white dwarf will survive for trillions of years before fading to black.

1.2 The structure of the Sun

To understand the Sun it is necessary to describe its own structure. It can be divided in different regions (Figure 1.1):

1. The core;
2. The radiative zone;
3. The convective zone;
4. The photosphere;
5. The chromosphere;
6. The transition region;
7. The corona;

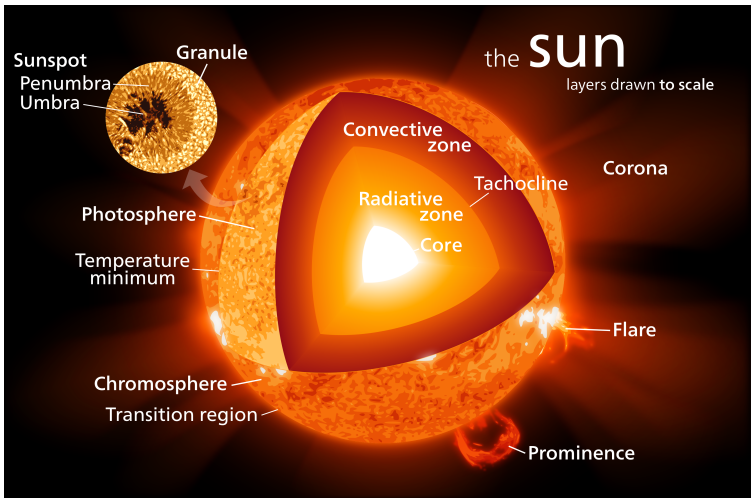

Figure 1.1: A representation of different Sun's layers.

1.2.1 The Core

The core, inside 0.24 $R_{\odot}$, generates 99% of the fusion power of the Sun. Fortunately for life on Earth, the Sun's energy output is just about constant, so we do not see much change in its brightness or the heat it gives off.

The Sun's core has a very high temperature, more than 15 million K, and has a density of up to 150 g/cm^3.

It is a combination of these two properties that creates an environment just right for nuclear fusion reactions to occur. In stars like the Sun the nuclear burning takes place through a three step process called the proton-proton or p-p chain (Figure 1.2)[Ferrari, 2011]. In the *first* step two protons collide to produce deuterium, a positron and a neutrino.

In the *second* step a proton collides with the deuterium to produce a He^3 nucleus and a gamma ray. In the *third* step two He^3 collide to produce a He^4 nucleus with the release of two protons. These ones release energy in two forms, light (electromagnetic radiation) and particles (in particular neutrinos).

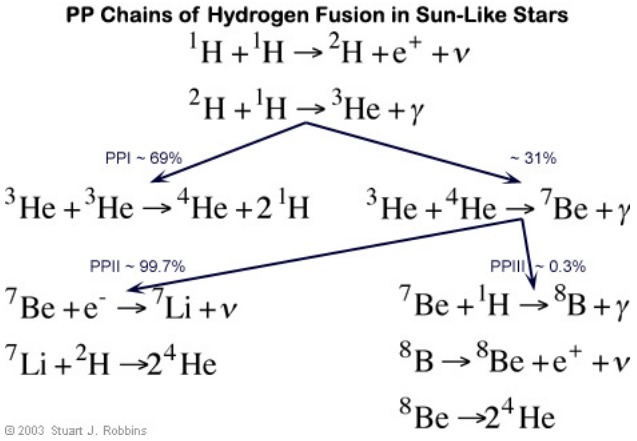

Figure 1.2: PP chain of Hydrigen fusion.

Both the temperature and the density decrease as one moves outward from the centre of the Sun. At the center of the Sun, fusion power is estimated by models to be about 276.5 watts/m^3.

The nuclear burning is almost completely shut off beyond the outer edge of the core (about

25 ٪ of the distance to the surface). At that point the temperature is only half its central value and the density drops to about 20 g/cm^3.

1.2.2 The Radiative and Convective zone

The radiative zone extends outward from the outer edge of the core to the interface layer or tachocline at the base of the convection zone (from 25٪ of the distance to the surface to 70٪ of that distance). The radiative zone is characterized by the method of energy transport : *radiation*. The energy generated in the core is carried by light (photons) that bounces from particle to particle. The density drops from 20 g/cm^3 down to only 0.2 g/cm^3 from the bottom to the top of the radiative zone.
The convection zone is the outer-most layer of the solar interior. It extends from a depth of about 200,000 km right up to the visible surface. At the base of the convection zone the temperature is about 2,000,000 K. This is cool enough for the heavier ions to hold onto some of their electrons and makes the material more opaque so that it is harder for radiation to get through. This mechanism traps heat that ultimately makes the fluid unstable and it starts to "boil"or convect. These convective motions carry heat quite rapidly to the surface. The fluid expands and cools as it rises. At the visible surface the temperature has dropped to 5700 K and the density is only 0.2 g/cm^3.

1.2.3 The Photosphere

The Sun's photosphere, is a 500 km thick region, from which most of the Sun's radiation escapes outward.
It has a temperature between 4,500 and 6,000 K with an effective temperature of 5,777 K and a density of about $2 \cdot 10^{-1} g/cm^3$. It is composed of convection cells called *granules cells* of plasma each approximately 1000 km in diameter with hot rising plasma in the centre and cooler plasma falling in the narrow spaces between them. Each granule has a lifespan of only about eight minutes, resulting in a continually shifting "boiling" pattern. A larger, undisputed pattern called super-granulation is a network of outward velocity flows, each about 30,000 km across, which is probably tied to the big convective zone rather than to the relatively small granules. The flow concentrates the surface magnetic fields to the super-granulation-cell boundaries, creating a network of magnetic-field elements.

The photospheric magnetic fields extend up into the atmosphere, where the supergranular pattern dominates the conducting gas. The photosphere is also marked by dark, cool sunspots, which emerge when the sun's magnetic field breaks through the surface. Sunspots appear to move across the Sun's disk. The observation of this motion led astronomers to realize that the Sun rotates on its axis.In the Sun different regions rotate at different rates. The Sun's equatorial regions rotate in about 25 days (sideral rotation), while the polar regions take more than 35 days (sideral rotation) to make a complete rotation. This phenomena is called *differential rotation.*

1.2.4 The Chromosphere

The parts of the Sun above the photosphere are referred to collectively as the solar atmosphere.

The chromosphere represents the dynamic transition between the cool temperature minimum of the outer photosphere and the diffuse million-degree corona above. It derives its name and pink colour from the red Hα line of hydrogen at 6562.8 Å. In chromosphere density decreases with height more rapidly than magnetic field strength and for this reason the magnetic field dominates the chromospheric structure, which reflects the extension of the photospheric magnetic fields.

When the Sun is viewed through a spectrograph or a filter that isolates the Hα emission, a wealth of new features can be seen. These features include the chromospheric network of magnetic field elements, bright plage around sunspots, dark filaments across the disk and prominences above the limb.

Because it strongly emits the high excitation lines of helium, the chromosphere was originally thought to be hot. Radio measurements, a particularly accurate means of measuring the temperature, show it to be only 8,000 K, somewhat hotter than the photosphere. Detailed radio maps show that hotter regions coincide with stronger magnetic fields.

The chromosphere is also visible in the light emitted by ionized calcium, CaII, in the violet part of the solar spectrum at a wavelength of 3934 Å(the Calcium K-line)

1.2.5 The Transition region

The transition region is a thin and very irregular layer of the Sun's atmosphere that separates the hot corona from the much cooler chromosphere.

Heat flows down from the corona into the chromosphere and in the process produces this thin region where the temperature changes rapidly from 1,000,000 K down to about 10,000 K (Figure 1.3).

This way, the solar transition region is believed to play an important role in coronal heating and solar wind acceleration. Hydrogen is ionized at these temperatures and is therefore difficult to see. Instead of hydrogen, the light emitted by the transition region is dominated by ions such as C^3, O^5 and Si^4.[Peter, 2001]

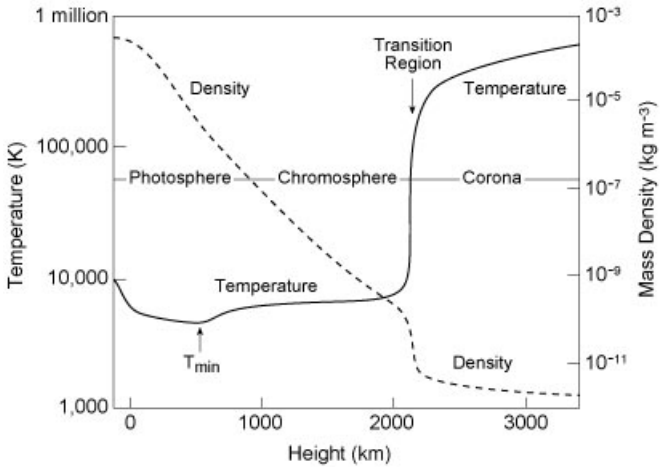

Figure 1.3: Variation of temperature and density in the transition region [Avrett, 2008].

1.2.6 The Corona

The inner corona, starting from the solar surface out to heliocentric distances of 5–10 $R_\odot$, is believed, at the present, to be the region where the imprint of the physical processes responsible for heating the coronal plasma and accelerating the solar wind is the most pronounced.

It is the critical region where the solar magnetic field undergoes the most dramatic changes as it evolves from the photosphere to the solar outward into interplanetary space. The inner corona establishes the connection between the Sun and the heliosphere.

Prior to the space age, total solar eclipses provided the only opportunities for exploring the plasma properties of the inner corona through imaging and spectroscopy, as the sky brightness is significantly reduced to level below the intensity of most emission lines out to 2-3 $R_{\odot}$.

The corona aspect presents systematic variations with solar cycle. During the minimum period of activity it has a less extension and semi-regular shape, with *streamers* mostly at low latitudes instead, during maximum periods it is more extended but at the same time more irregular, with *streamers* at all latitudes [Landi, 2008, chap. 5]. Optical radiation from corona can be divided in tree different components:

1. **The K Corona** (from *Kontinuum*);
2. **The F Corona** (from *Fraunhofer*);
3. **The E Corona** (from *Emission*);

The K-Corona

This component of the solar corona dominates at few distances from the edge. Its spectrum is flat, without Fraunhofer lines and with an intense linear polarization. These characteristics identify it like photospheric radiation diffused for *Thomson scattering* from electrons presents in corona. Considering that coronal plasma has a typical temperature of $10^6 K$,it is possible to obtain that its electrons have thermal velocity of $10^3 Km/s$. From systematic observations of K-Corona it is possible to have informations about electronic density of the region.[Landi, 2008]

The F-Corona

This region dominates at greater distances from solar disk at about 2-3 $R_{\odot}$. The radiation is not polarized and the spectrum shows Fraunhofer lines. These features leads to the conclusion that this part of corona is due to the *Mie scattering* from particles of dust that have smaller velocities than electrons.[Landi, 2008]

The E-Corona

It is due to atomic emission processes resulting in spectral lines. These ones are lines of high order ions and the more intense are:

1. The *red line* of FeX at 6374.5 Å
2. The *green line* of FeXIV at 3302.9 Å
3. The *yellow line* of CaXV at 5694.5 Å
4. The *infrared line* of FeXIII at 10746.9 Å

These emission lines violate the selection rule of Laporte[1] because they come from magnetic dipole transitions between energetic levels belonging to the same configuration. Corona can be observed in these lines through a corograph or a narrow band filter. The Sun's corona is characterised from different structures like *coronal holes*, *helmet streamers*, *coronal loops*, *protuberance* and *CME*.

Coronal holes are wide areas without X-emission (for this reason appear dark in X-observations, see Figure 1.4) that are mainly concentrated in the polar regions even if they can extend till the equator. Here the X-emission is due to the *bremsstrahlung* that is proportional to the square of density. These holes delineate open force lines of the magnetic field from which the fast solar wind originates.

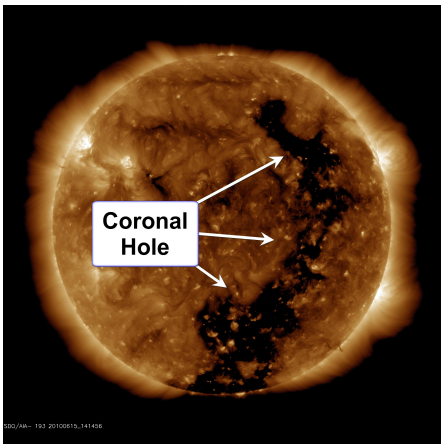

Figure 1.4: Coronal hole.

[1]The Laporte rule is a spectroscopic selection rule that only applies to centrosymmetric molecules (those with an inversion centre) and atoms. It states that electronic transitions that conserve parity, either symmetry or asymmetry with respect to an inversion centre are forbidden.

Helmet streamers(Figure 1.5)are large cap-like coronal structures with long pointed peaks that usually overlie sunspots and active regions. Helmet streamers are formed by a network of magnetic loops that connect the sunspots in active regions and help suspend the prominence material above the solar surface. The closed magnetic field lines trap the electrically charged coronal gases to form these relatively dense structures. The pointed peaks are formed by the action of the solar wind blowing away from the Sun in the spaces between the streamers.

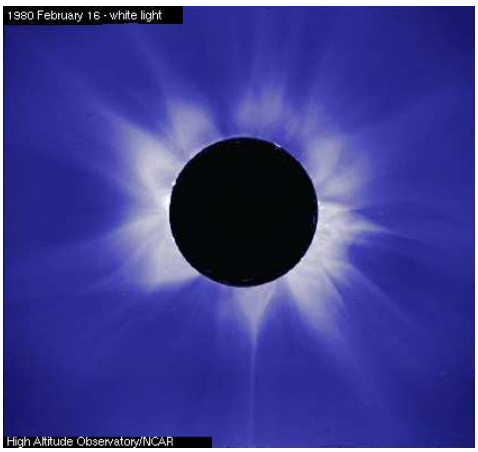

Figure 1.5: Helmet streamer(Credits: HAO/NCAR).

Coronal loops are immense arches of hot gas on the surface of the Sun,associated with the closed magnetic field lines that connect magnetic regions on the solar surface. They are visible at x-ray ultraviolet and white light wavelengths.

Protuberances Gas clouds that stretch out from the chromosphere of the Sun in the corona, up to heights that sometimes exceeds 500,000 km. These structures are observable trough coronographs during eclipses, in white light or better with Hα filters. They can be divided in *quiescent* and *eruptive*. The first ones are very stable and visible for a long time, during which they maintain their own shape. The second protuberances are so called for their sudden disappearance. Protuberances don't have an homogeneous structure, but they mainly show an arc structure. The arc is anchored to the photosphere

at its two extremes, said "feet" of prominence, and rises in the central region at heights typical of the order of 30,000 km. The protuberance is formed along a so-called neutrality photospheric region, that separates one area of the solar surface where the magnetic field has a certain polarity from that one with the opposite polarity.

Coronal mass ejections(CMEs) (Figure 1.6) are important sources of adverse space weather effects and they are often associated with dramatic changes of coronal magnetic fields. A CME is a large eruption of magnetized plasma from the Suns corona, that propagates outward into interplanetary space. The CME is one of the main transient features of the Sun. Although it is known to be formed by explosive reconfigurations of solar magnetic fields through the process of *magnetic reconnection*, its exact formation mechanism is not yet understood. Coronal mass ejections are often associated with solar flares and prominence eruptions but they can also occur in the absence of either of these processes. The frequency of CMEs varies with the sunspot cycle. At solar minimum we observe about one CME a week. Near solar maximum we observe an average of 2 to 3 CMEs per day.

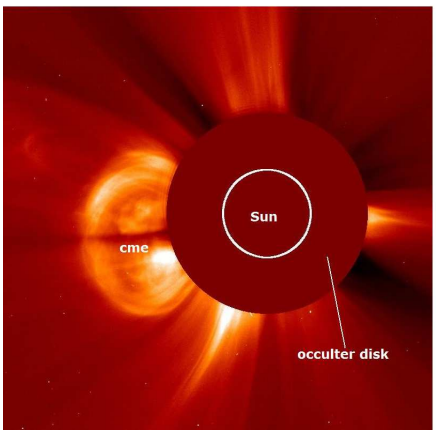

Figure 1.6: Coronal mass ejection (Credits: Nasa/Marshall Solar Physics).

Solar wind is a stream of charged particles released from the upper atmosphere of the Sun. As a result of thermal collisions, the particles within the inner corona have a range

and distribution of speeds described by a Maxwellian distribution. The mean velocity of these particles is about 145 km/s, which is well below the solar escape velocity of 618 km/s. However, a few of the particles achieve energies sufficient to reach the terminal velocity of 400 km/s, which allows them to feed the solar wind. At the same temperature, electrons, due to their much smaller mass, reach escape velocity and build up an electric field that further accelerates ions, charged atoms, away from the Sun.

The solar wind (Figure 1.7) is divided into two components, respectively termed the *slow* solar wind and the *fast* solar wind.

The slow solar wind has a velocity of about 400 km/s (measured at 1 AU), a temperature of $1.4–1.6 \cdot 10^6$ K and a composition that is a close match to the corona.

By contrast, the fast solar wind has a typical velocity of 750 km/s (measured at 1 AU), a temperature of $8 \cdot 10^6$ K and it nearly matches the composition of the Sun's photosphere.

The slow solar wind appears to originate from a region around the Sun's equatorial belt that is known as the "streamer belt".

The fast solar wind is thought to originate from coronal holes. Such open lines are particularly prevalent around the Sun's magnetic poles.[Landi, 2008]

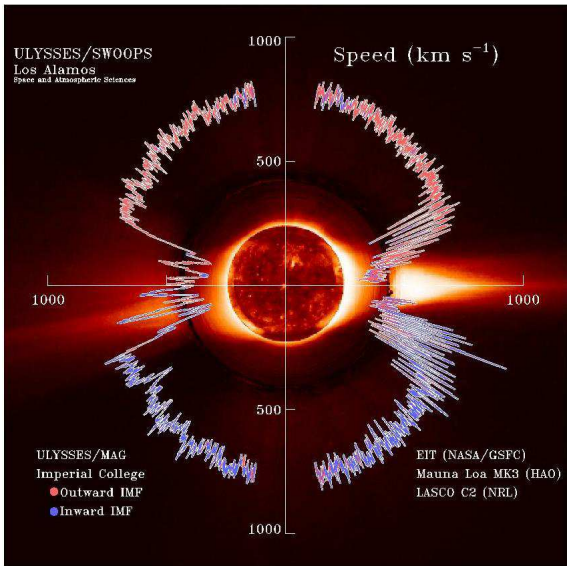

Figure 1.7: Solar wind velocities (Credits: Nasa/Marshall Solar Physics).

1.2.7 Ground-based coronal observation

At optical wavelengths, the corona of the Sun can be studied most conveniently during a total solar eclipse or with the help of a *coronagraph*.
The **coronagraph** (Figure 1.8) was invented by the French astronomer Bernard Lyot in 1939, to enable astronomers to observe corona without having to wait for total solar eclipses. This one imitates the effects of the Moon by placing an occulting disk at the focal position of the Sun's image to block it out, thus creating a pseudo-eclipse and enabling observation of the faint rays of the corona.
The objective lens is subjected to the intense rays of the Sun and so reflected light from the surface of the lens as well as light scattered by scratches, internal bubbles and striations are easily generated. This scattered light avoids the observation of the faint corona.
Preventing this phenomenon requires use of a single lens made from high-grade optical glass that resists air bubbles and striations. To obviate this drawback, in the focal plane of the first objective lens have, as well as a blackout disc, a field lens.[Landi, 2008] This lens forms an image of the objective lens edge on a circular diaphragm, called *Lyot stop*.
It is necessary that the Lyot stop is positioned in the conjugate point of the first objective lens with respect to the field one.
The second objective lens then converge the image of the blackout disk and corona in the focal plane of the instrument where is placed the detector.
Unfortunately, the incoming light at the telescope pupil is, in practice, disturbed by atmospheric turbulence. Coronagraphs should be located at fairly high altitudes, to minimize diffusion phenomena due to the Earth atmosphere, in regions where frequent precipitations clean the air of accumulated contamination.
The invention of coronagraph enabled daily observations in unpolarized and polarized white light and in some of the corona forbidden lines such as FeX at 637.4 nm, FeXIII at 1074.7 nm and FeXIV at 530.3 nm.
However, imaging and spectroscopy with a coronagraph remained limited to distances above 1.05 solar radii due to the diffraction above the edge of the occulter.[Sivaramakrishnan et al., 2001]

Lyot also co-invented (with Y. Öhman) the *birefringent filter*, which enabled to take monochromatic pictures of coronal and chromospheric phenomena.
The principle of the filter relies on the interference produced between the ordinary and

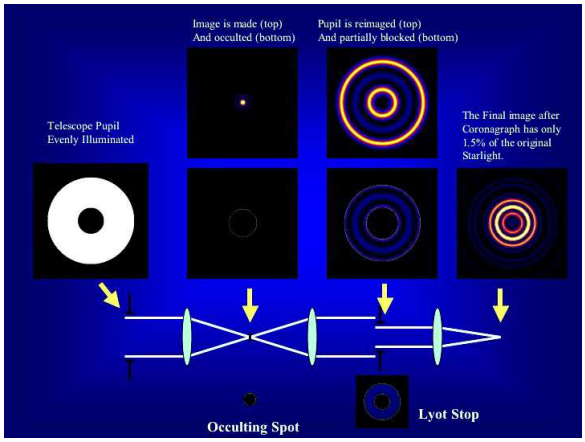

Figure 1.8: Diagram of the Lyot's coronagraph (adapted from [Sivaramakrishnan et al., 2001]).

extraordinary rays passing through a birefringent crystal such as calcite. Since the refractive index of the crystal differs for the two rays, they emerge with a phase difference that depends (for a given calcite thickness) on the wavelength of the light (Figure 1.9).

$$\delta = \frac{2\pi l(n_o - n_s)}{\lambda} \tag{1.1}$$

with l the length of the crystal,n_o the ordinary refractive index and n_s the extraordinary one.

Transmission is minimal for wavelengths at which the block of calcite yields a phase difference of π. A real filter consists of several calcite elements separated by polarizing filters. The passband $\Delta\lambda$ is given by:

$$\Delta\lambda = \frac{\lambda_0}{2^{k-1}m} \tag{1.2}$$

where k is the number of crystals and m in an integer. The birefringent filter can be built to produce narrow passbands 0.25 Å or less with a few percent transmission, uniform over a field of view of roughly 1° [Landi, 2008].

1.3 Observations of the Sun from space

The desire to study the Sun, its phenomena and its structures beyond the limitations characteristics of ground-based observations led to the lunch of numerous space missions. Among the most important there are:

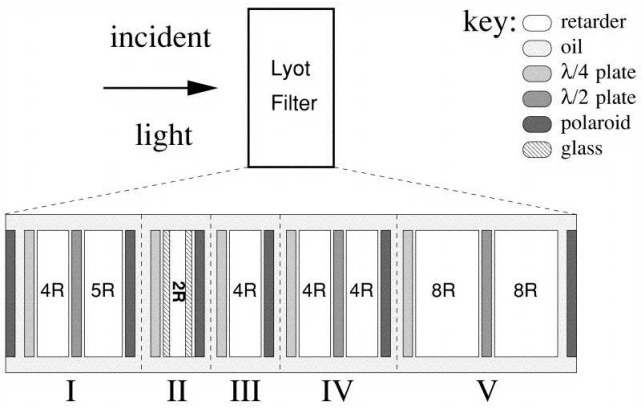

Figure 1.9: Basic structure of the proposed five-stage Lyot filter [Bland-Hawthorn et al.,2001]

- Two probes, *Helios 1 and 2*, were launched in November 1974 and January 1976 to make the first studies of the Sun.
  Their looping orbits took them to within a third of the distance of the Earth from the Sun, sending back information on solar plasma, the solar wind, cosmic rays, and cosmic dust, plus data about its magnetic-field.

- *Ulysses* was launched from the space shuttle Discovery in October, 1990. It flew via Jupiter to be sent on a path that would carry it to high solar latitudes from where it could look down on the Sun.
  Ulysses operated for 12 years, returning data that helped scientists understand the nature of the Sun's environment, called the heliosphere, and the forces active in its outer atmosphere.

- In December 1995, a joint NASA/ESA probe called *SOHO* (the Solar and Heliospheric Observatory) was launched from Cape Canaveral, Florida, to study the Sun from its core to the outer corona and solar wind. With an original two-year mission, this highly successful satellite is still going today, orbiting the Sun in step with the Earth.

- *Cluster* is a constellation of four spacecraft, launched in two pairs in 2000 by Russian Soyuz rockets to fly in formation around Earth. Together they sent back detailed 3D data about how the solar wind affects our planet.

- In February 2002, NASA launched one of its Small Explorer Missions, called *RHESSI* (The Reuven Ramaty High Energy Solar Spectroscopic Imager) which focused on

studying explosive solar flares.

- One of the major space observatories currently observing the Sun is *Hinode*, a joint project between Japan, the US and the UK, which was launched in September 2006 from Uchinoura Space Center, Japan.
  The spacecraft carries three science instruments with which to watch our home star: *the Solar Optical Telescope, X-ray Telescope and Extreme Ultraviolet Imaging Spectrometer.*
  They work together to study how magnetic energy is generated and travels from the visible surface, or photosphere, of the Sun to the corona plus how that energy is released into the Sun's outer atmosphere.

- In October 2006 there was the launch from Cape Canaveral of NASA's *STEREO* (Solar Terrestrial Relations Observatory) mission,two nearly identical observatories which are giving us, as their name suggests, a three-dimensional view of the Sun.
  This was achieved by placing one of the telescopes ahead of Earth in its orbit with the other trailing behind our planet.
  STEREO has helped scientists understand much more about the flow of energy and matter from the Sun to Earth by revealing the 3D structure of coronal mass ejections, those violent eruptions of matter from the sun that can disrupt satellites and power grids.

- Launched in November 2009, ESA's low-cost *Proba-2* was launched into orbit around the Earth from the Plesetsk Cosmodrome, Russia, carrying two instruments to observe the Sun - a Large Yield Radiometer (LYRA) and an extreme-ultraviolet telescope (SWAP) - plus two more Czech experiments to monitor space weather.

- A French satellite called *PICARD* launched from Russia in June 2010 to measure solar irradiance, the diameter and solar shape, and to probe the Sun's interior using seismological techniques.

- The last major space telescope to go into action was NASA's *Solar Dynamics Observatory* which launched in February 2010 from Cape Canaveral. The Solar Dynamics Observatory is the first mission to be launched for NASA's Living With a Star (LWS) Program, a program designed to understand the causes of solar variability and its impacts on Earth. SDO is designed to help to understand the Sun's influence on

Earth and Near-Earth space by studying the solar atmosphere on small scales of space and time and in many wavelengths simultaneously.
SDO will fly three scientific experiments:

- Atmospheric Imaging Assembly (AIA)
- EUV Variability Experiment (EVE)
- Helioseismic and Magnetic Imager (HMI)

Each of these experiments perform several measurements that characterize how and why the Sun varies. These three instruments will observe the Sun simultaneously, performing the entire range of measurements necessary to understand the variations on the Sun.[Lemen et al., 2011]

Next projected missions are:

- ESA's *Solar Orbiter* is due to launch in 2017 on a seven-year mission to study the Sun and how it drives space weather. The spacecraft's orbit will take it closer to the Sun than the planet Mercury, at a distance of 42 million kilometres.
  Solar Orbiter will coordinate with a NASA mission to send six Solar Sentinels to watch the star. Four identical probes called Inner Heliospheric Sentinels will sit inside the orbits of Venus and Mercury to taste energetic particles streaming in the solar wind. They will be aided by a Near-Earth Sentinel, a single probe orbiting Earth which will observe the corona, and a Farside Sentinel that will watch the other side of the Sun.

- Most daring mission is one planned by NASA for launch in 2018, called *Solar Probe Plus*. This spacecraft will fly closer to the Sun than any has before in a bid to find out how its corona is heated and how the solar wind is accelerated.

Chapter 2

Physical properties of solar corona

2.1 Introduction

The matter also in the external part of the solar atmosphere is in the state of plasma, at very high temperature (a few million Kelvins) and at very low density (of the order of 10^{16} - $10^{14} g/cm^3$). The corona emits radiation mainly in the X-rays and EUV.
Particles are so isolated, for their low density, that almost all the photons can leave the Sun's surface without interacting with the matter above the photosphere: in other words, the corona is transparent to the radiation and the emission of the plasma is optically-thin.
In an optically-thin plasma the matter is not in a thermodynamical equilibrium with the radiation, because collisions between particles and photons are very rare. The result is that the emission spectrum does not fit the spectral distribution of a blackbody radiation, but it depends on those collisional processes which occur in a very rarefied plasma.
While the Fraunhofer lines coming from the photosphere are absorption lines, principally produced from ions which absorb photons of the same frequency of the transition to an upper energy level, coronal lines are emission lines produced by ions which had been excited to a superior state by collisional and radiative processes.
Many spectral lines, emitted by highly ionized atoms, can be formed only at certain temperatures and therefore their individuation in solar spectra is a strong indication of the emitting plasma temperature.
Some of these spectral lines can be forbidden on the Earth: in fact, collisions between particles can excite ions to metastable states; in a dense gas these ions immediately collide with other particles and so they de-excite with an allowed transition to an intermediate

level, while in the corona it is more probable that these ions remain in a metastable state, until they encounter photons of the same frequency of the forbidden transition to the lower state.
These photons induce the ions to emit with the same frequency by stimulated emission. Forbidden transitions from metastable states are often called as satellite lines.
In this chapter will be analysed some of the most interesting properties of the solar corona such as the formation of emission lines,heating mechanism and magnetic field.

2.2 Radiation from hot plasma

Hot plasmas, such as coronal gas, radiate energy efficiently, especially if the gas contains any appreciable fraction of heavy elements such as oxygen and iron.
The relative unimportance of hydrogen and helium in the emission process is due to their almost complete ionization at coronal temperatures. The heavier elements have all of their outer electrons stripped, but the inner shell electrons require higher energies for removal and for those elements the ionization process is not yet total at coronal temperatures.
The abundance of all elements heavier than helium in the solar atmosphere is very small relative to hydrogen. At the temperatures and densities found in the corona the elements which dominate the radiative emissions are Fe, Si, S and O, which together make up only 0.03% by the numbers of the atoms in the coronal gas.
In corona, emission in a spectral line of some element X occurs by transition from a level j to a level i ($j > i$):

$$X_j^{+m} \rightarrow X_i^{+m} + h\nu_{ij} \tag{2.1}$$

where X^{+m} indicates an atom of element X with m electrons removed. This process is often called "bound-bound" emission since it occurs from one bound state to another.
The photon is emitted at a frequency ν_{ij} corresponding to the energy difference between levels i and j. If measurement is made at a particular frequency then we need to take into account the fact that the shape of the spectral line s not an infinitely sharp δ-function, but rather that the photons are emitted over range of wavelengths.
This spread is called the *emission profile* ψ_ν and it is typically a sharply-peaked function roughly centred about ν_{ij}
The spectral profile of the line is essentially characterized by the Doppler broadening given by the high temperatures of the plasma. Due to the component parallel to the line of sight

of the velocity **v** of the emitting ion, the photon is issued for the Doppler effect in a range of frequencies $\Delta\nu$ centred around the ν_{ij} .

The velocity **v** will be mainly due to the velocity of thermal agitation of ion and to micro-turbulence or to the motion of the plasma accelerated in the solar wind into interplanetary space.

Under the assumption of a Maxwellian distribution of velocities, the relative broadening $\Delta\lambda$ for a plasma temperature T is given by:

$$\Delta\lambda \simeq \frac{v\lambda}{c} \simeq \frac{\lambda}{c}\sqrt{\frac{2k_BT}{m}} \tag{2.2}$$

where k_B is Boltzmann's constant, m the mass of the emitting ion and c the speed of light. The emissivity of the plasma at wavelength per volume unit of plasma, given in $ergcm^{-3}sec^{-1}Hz^{-1}$, is:

$$P_\nu = N_j(X^{+m})A_{ji}h\nu_{ij}\psi_\nu \tag{2.3}$$

where $N_j(X^{+m})$ is the number density of atoms of the ion species X^{+m} which are in level j, and A_{ji} is the Einstein emission coefficient. ψ_ν is normalized to unity.

The total power, in $ergcm^{-3}sec^{-1}$, emitted in this transition per volume unit of coronal plasma is:

$$P_{ij} = N_j(X^{+m})A_{ji}h\nu_{ij} \tag{2.4}$$

Here P_{ij} is P_ν integrated over all frequencies. The flux detected at the Earth in the emission line is given by:

$$F_{ij} = \frac{1}{4\pi R^2}\int P_{ij}dV \tag{2.5}$$

where R is 1 A.U and the units of F_{ij} are $ergcm^{-2}s^{-1}$.

The major unknown quantity is the number density $N_j(X^{+m})$. Its value is obtained by a series of steps from the more easily determined electron density Ne.

The steps involved are:

- determination of the hydrogen abundance relative to electron density $N(H)/Ne$;
- determination of the abundance of element X relative to hydrogen, $N(X)/N(H)$;
- determination of the fraction of the element X in ionization stage +m, $N(X^{+m})/N(X)$;
- determination of the fraction of atoms of element X in ionization stage +m which are in level j, $N_j(X^{+m})/N(X)$;

The term $N(X^{+m})/N(X)$ gives the fraction of element X which is m-times ionized. For a volume of plasma which is in equilibrium at some temperature T, the degree of ionization depends upon the balance between processes which cause the atom to have the particular number m electrons stripped away, and those processing which decrease the number of atoms having exactly m electrons removed

In a low density and high temperature plasma, such as solar corona, ionization generally proceeds by collisions with free electrons. This process requires that the ambient electrons have velocities comparable to those of the bound ones which they are supposed to remove from the atoms. Therefore the ionization process proceeds to the point at which the binding energy needed for ionization is comparable with the energy of the thermal electron.

Since the inner electrons have progressively larger binding energies, the higher ionization stage species are produced in hotter plasmas. The lower ionization species then disappear by excitation upward to the more ionized species. It is possible to calculate the term $N(X^{+m})/N(X)$ taking into account the most effective processes in terms of coronal plasma:

Collisional ionization

Mainly due to the collision of atoms with thermal electrons, is described by the process

$$X^{+m} + e^- \rightarrow X^{+m+1} + 2e^- \tag{2.6}$$

In a ionization state X^{+m} of the element X, there is a electronic temperature $T_e(+m)$ of maximum efficiency of the process of collisional ionization, which is called "temperature of maximum formation"; for $T = T_e(+m)$ there is a maximum of X^{+m} ionization curve whereas for $T \neq T_e(+m)$ the abundance N(X^{+m}) decreases going ideally toward zero.

Dielectronic recombination and autoionization

When a free electron is captured by the ion, but in resonance with one of the inner electrons to an energy corresponding to a state of ionization of the ion itself; the result is that both electrons are at the end in an excited state.

At this point the reaction can follows two directions: or occurs the process of *autoionization* and the ion returns at the previous state of the electron capture or the electron innermost of the two can release a radiative transition falling to a lower level and thus emitting a photon.[Golub et al., 2010]

2.2.1 Level population: the coronal approximation

An electron of an atom at ionization stage $+m$ may be found in the ground level g of that stage or in any of the infinite number of available excited levels. The electron may be excited up to a level j by any number of processes. The level can be depopulated by either spontaneous or stimulated emission to a lower level.
Spontaneous emission is the process by which a quantum system such as an atom, molecule, nanocrystal or nucleus in an excited state undergoes a transition to a state with a lower energy and emits a quanta of energy.
It is the predominant emission process in the coronal plasma. The probability of spontaneous emission is much greater than the probability of stimulated emission and collisional excitation, even in the case of magnetic dipole transitions or electric quadrupole which give rise to the forbidden lines not visible in a laboratory plasma and which represented one of the more difficulty in identifying the coronal spectrum.
In general, the population density of the *j-th* level must be calculated by summing over a number of adjacent levels and taking into account all of these various collisional and radiative excitation and de-excitation mechanisms.
Under conditions usually found in the solar corona, it is often possible to use a simplified calculation, the so-called *coronal approximation.*
Here we assume that level j is populated exclusively from the ground level g, by collisions with thermal electrons and rarely by radiative excitation.
The collisional excitation occurs when an ion in the ground state g collide with an electron of kinetic energy sufficient to bring the ion in an excited state j. It is dominant for almost all the coronal lines.
The process of radiative excitation consists in the absorption, by an coronal ion in the ground state g, of a photon coming from the atmosphere below with a frequency corresponding to the frequency ν_{gj} of the transition considered. Level j is taken to be depopulated exclusively by radiative decay to the lower levels. Collisional de-excitations are neglected. Also, population of level j by cascade from higher levels is neglected.[Golub et al., 2010]
As a consequence of the increased efficiency of the spontaneous decay from the excitation process we have that the fundamental level of the population is much greater than the population excited level. The rate of excitation to the upper level j is then given by the product of ground state population N_g with the electron density N_e and with the electron

collisional excitation rate coefficient C^e:

$$R_u = N_g(X^{+m})N_e C^e_{gj} \tag{2.7}$$

The upper level is depopulated by spontaneous emission to the lower levels, whose rate is given by:

$$R_d = N_j(X^{+m}) \sum_{k<j} A_{jk} \tag{2.8}$$

2.3 Coronal magnetic field

The origin of eruptive phenomena in the solar corona is related to the coronal magnetic field as magnetic forces dominate over other forces in the corona.

It is widely believed that the Sun's magnetic field is generated by a magnetic dynamo within the Sun. The fact that the Sun's magnetic field changes dramatically over the course of just a few years, and the fact that it changes in a cyclical manner indicates that the magnetic field continues to be generated within the Sun.

Magnetic fields are produced by electric currents. These currents are generated within the Sun by the flow of the Sun's hot, ionized gases. We observe a variety of flows on the Sun's surface and within its interior. Nearly all of these flows may contribute in one way or another to the production of the Sun's magnetic field.

Magnetic fields are a little like rubber bands. They consist of continuous loops of lines of force that have both tension and pressure. Like rubber bands, magnetic fields can be strengthened by stretching them, twisting them, and folding them back on themselves. This stretching, twisting, and folding is done by the fluid flows within the Sun.

Early models of the Sun's magnetic dynamo worked on the idea that the dynamo activity occurs throughout the entire convection zone. It was soon realized, however, that magnetic fields within the convection zone would rapidly rise to the surface and would not have enough time to experience either the alpha or the omega effect. Since a magnetic field exerts a pressure on its surroundings, regions with a magnetic field should push aside the surrounding gas and make a bubble that would continue to rise all the way to the surface.

This buoyancy is not produced in the stable layer below the convection zone. Within the radiative zone the magnetic bubble would rise only a short distance before it would find

itself just as dense as its surroundings. This led to the idea that the Sun's magnetic field is being produced in the interface layer between the radiative zone and the convection zone. This interface layer is also a place where there are found rapid changes in rotation rate looking inward or outward across it.

Reliable high accuracy magnetic field measurements are only available in the photosphere. These measurements,called *vector magnetograms*, provide the magnetic field vector in the photosphere. To get insights regarding the structure of the coronal magnetic field one way is to compute 3D magnetic field models, which use the measured photospheric magnetic field as the boundary condition.

This procedure is often called *extrapolation of the coronal magnetic field from the photosphere.*

An important quantity is the plasma value β, a dimensionless number which is defined as the ratio between the plasma pressure and the magnetic pressure,

$$\beta = 2\mu_0 \frac{p}{B^2} \tag{2.9}$$

The plasma β value changes with height in the solar atmosphere. As one can see in figure 2.1 a region with $\beta \ll 1$ is sandwiched between the photosphere and the upper corona, where β is about unity or larger. In regions with $\beta \ll 1$ the magnetic pressure dominates over the plasma pressure and plasma is draggeg by magnetic field instead where $\beta \gg 1$ plasma is dominated by thermal phenomena and magnetic field lines are frozen into it [Landi, 2008].

As a first approximation it can be assumed that the corona does not have electrical currents, so:

$$rot\vec{B} = 0 \tag{2.10}$$

Current free (potential) fields are the simplest assumption for the coronal magnetic field. The line-of-sight (LOS) photospheric magnetic field which is routinely measured with magnetographs are used as boundary conditions to solve the Laplace equation for the scalar potential ϕ,

$$\triangle\, \phi = 0 \tag{2.11}$$

where the Laplacian operator $\triangle$ is the divergence of the gradient of the scalar field and

$$\vec{B} = -\nabla\phi \tag{2.12}$$

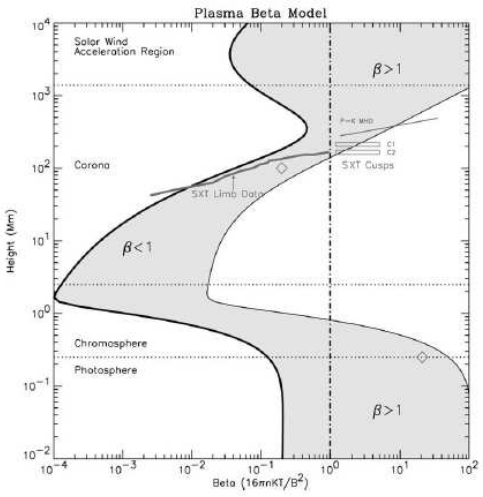

Figure 2.1: Plasma β model over active regions [Gary, 2001].

The magnetic vector B in this case is called *potential magnetic field*.

Introducing a reference system (x,y,z) with the z-axes directed along the vertical, the magnetogram provides, as function of x and y, the magnetic field component B_z at the hight, z=0, at witch the magnetographic line is used to form.

This component can be related with the density of magnetic monopoles, σ_m:

$$\sigma_m = \frac{1}{2\pi} B_z \tag{2.13}$$

In an arbitrary point of the corona with coordinates $\vec{r}$, the magnetic field is given by:

$$\vec{B}(\vec{r}) = -grad[\frac{1}{2\pi} \int \frac{B_z(\vec{r'})}{|\vec{r} - \vec{r'}|} d\Sigma'] \tag{2.14}$$

where $\vec{r'}$ is the coordinate of a point which belong to the plane z=0 and where the integral should be extended to the plane itself.

The approximation of potential field is however rather restrictive because it implies that there are no electric currents in the corona.

A second hypothesis is to assume that currents can only flow along the magnetic field force lines without exerting force on coronal plasma.

This way it is possible to obtain a magnetic field called *force-free* characterised by the expression:

$$\nabla \times \vec{B} = \alpha \vec{B} \tag{2.15}$$

$$\vec{B} \cdot \nabla \alpha = 0 \tag{2.16}$$

where α is called the *force-free parameter* or force-free function. From the horizontal photospheric magnetic field components (B_{x0}, B_{y0}) the vertical electric current density is given by:

$$\mu_0 j_{z0} = \frac{\partial B_{y0}}{\partial x} - \frac{\partial B_{x0}}{\partial y} \tag{2.17}$$

and the corresponding distribution of the force-free function $\alpha(x, y)$ in the photosphere is:

$$\alpha(x, y) = \mu_0 \frac{j_{z0}}{B_{z0}} \tag{2.18}$$

Parameter α can be a function of position, but Equation (1.19) requires that α be constant along every field line. If α is constant everywhere in the volume under consideration, the field is called linear force-free field (LFFF), otherwise it is non-linear force-free field (NLFFF).

Equations (1.18) and (1.19) constitute partial differential equations of mixed elliptic and hyperbolic type [Wiegelmann et al., 2012].

They can be solved as a well-posed boundary value problem by prescribing the vertical magnetic field and for one polarity the distribution of α at the boundaries.

As shown by Bineau [Bineau, 1972] these boundary conditions ensure the existence and uniqueness of NLFFF solutions at least for small values of α and weak non-linearities.

Techniques of extrapolation of photospheric magnetic fields to the corona, although very interesting, are far from giving a satisfactory description of the coronal field because, in a few cases it is found that the extrapolated field force lines coincide with those that are bounded from visible coronal structures.

It is believed that this is due to the lack of spatial resolution of available magnetographs.

2.4 Coronal Heating

The coronal heating problem is one of the longest running solar physics topic and is still a highly controversial topic. The corona is not energetically isolated from the other regions of the atmosphere, such as the chromosphere, but instead the whole of the solar atmosphere forms a highly coupled system, with both energy and mass transferred in both directions between the chromosphere and corona through the transition region. The chromosphere has very different plasma properties to the corona and so explaining the heating of the solar atmosphere is now recognised to be considerably more complicated than had

been appreciated during much of the twentieth century. The coronal heating problem first arose following the work of Grotrian [Grotrian, 1939] and Edlén [Edlèn et al., 1954] who discovered that emission lines observed during a total solar eclipse in 1869 were not due to a new element called coronium, but were the result of highly ionised iron. The temperature of the corona is in excess of a million degrees Kelvin. In comparison, the temperature near the Sun's surface, the photosphere, is just 6,000 K. At the same time the density falls by six orders of magnitude from the photosphere to the corona. The structure of the magnetic field is highlighted in coronal images because heat is spread efficiently along field lines, but transport across them is greatly inhibited. In the corona, the combined radiative and conductive losses in active regions are 10^7 $ergcm^2s^{-1}$ and in the quiet-Sun are $3 \cdot 10^5$ $ergcm^2s^{-1}$, whereas in the chromosphere they are $2 \cdot 10^7$ $ergcm^2s^{-1}$ and $4 \cdot 10^6$ $ergcm^2s^{-1}$ in active regions and the quiet-Sun, respectively [Withbroe et al.,1977]. The source of this energy is convective churning of the plasma at and below the photosphere. These motions continuously move the footpoints of the ubiquitous magnetic fields that thread through the surface of the Sun with the timescale of these motions, relative to the end-to-end Alfvén travel time, leading to one of two fundamental types of heating mechanism. *Slow*(long timescale) motions result in a quasi-static stressing of the field, whilst *fast*(short timescale) motions generate waves. The dissipation of magnetic stresses, which typically manifest themselves in the form of current sheets, leads to magnetic reconnection and is known as DC heating, whilst the dissipation of waves is referred to as AC heating. In both cases the actual dissipation will occur at kinetic scales, since the Lundquist number (the ratio of the Ohmic dissipation time to the Alfvén crossing time) is very large ($\approx 10^{10-13}$). Current parallel computers have neither the memory nor the power to permit well resolved models on all scales and current imagining telescopes have neither the required spatial and temporal resolution nor the sensitivity to see anything at the kinetic scale. Additional difficulties arise in the form of the coupling between the dense interior and tenuous outer atmosphere which require very different physics and, for open magnetic field regions, mechanisms must also account for the mass flux loss due to the solar wind. With all these difficulties it is not surprising that, to date, researchers have been unable to properly explain the solar heating problem. Since the identification of the hot solar atmosphere, there have been a huge number of heating mechanisms proposed that involve reconnection or magnetic waves.

Chapter 3

Study of polarized light

3.1 Introduction

Measurements of the magnetic field vector components in the solar corona can potentially yield critical information to our understanding of coronal structure dynamics and heating. Forbidden coronal emission lines of magnetic dipole M1 appear to have the highest potential to address outstanding problems in coronal physics especially those related to the storage and the release of magnetic free energy.

In atomic physics most radiative transitions are electric dipole (E1) transitions, satisfying the selection rule: 'ΔJ=$\pm$1, 0'; there is a change in parity, where ΔJ is the change in angular momentum of the atom. In contrast, a magnetic dipole (M1) transition satisfies the selection rule: 'ΔJ=$\pm$1, 0'; there is no change in parity. A relativistic M1 transition is a radiative M1 transition between states of the same parity but with orthogonal spatial wavefunctions-a highly forbidden transition in atomic physics. Interest in forbidden transitions was, for a long time, restricted to astrophysics, where collisional de-excitation can be sufficiently slow to allow metastable states to live out their natural life, to then die a natural death with the emission of one (or more) photons.

Measurements of the full Stokes profile of M1 lines can constrain both the line of sight LOS field strength $B_{\shortparallel}$ through the longitudinal Zeeman effect seen in Stokes V profiles and the direction of the vector field projected onto the plane of the sky POS through the analysis of resonance scattering induced by linear polarization seen in Stokes Q and U in the so called strong field regime of the Hanle effect.

A good choice for magnetic field investigations is FeXIV line at 530.3 nm because of

good compromise between line intensity and polarization relatively to the photospheric background, see Figure 3.1[Edlèn et al., 1954].

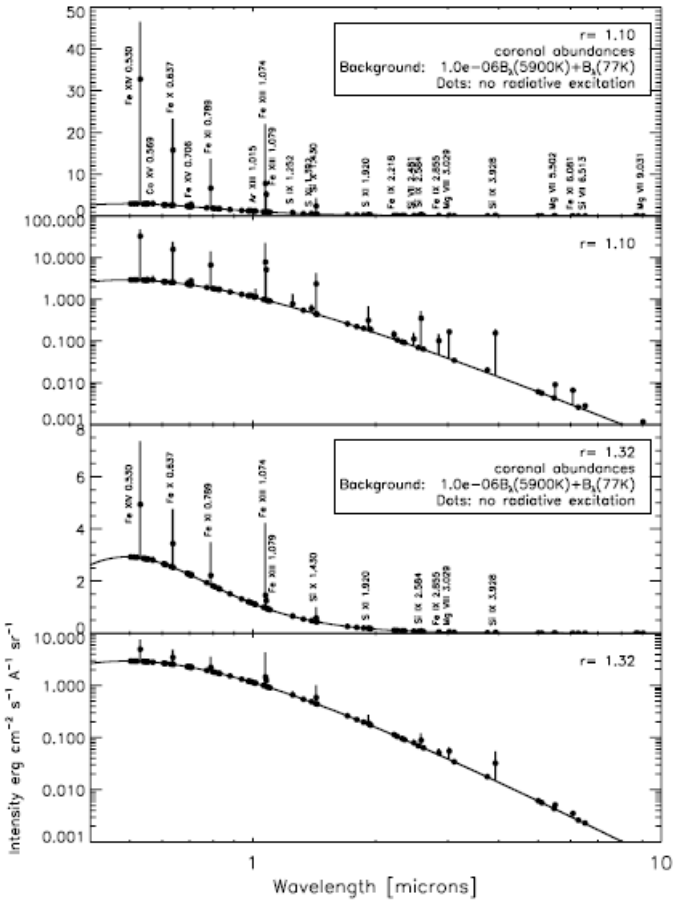

Figure 3.1: Synthetic emission line intensity spectra evaluated at and solar radii. Line identifications are marked for lines whose peak intensities exceed 20% of the neighboring background intensity [Judge et al., 2011].

The ground term of Fe XIV has a $3s^2 3p$ configuration, with a $^2P^0_{1/2}$ ground state and a $^2P^0_{3/2}$ excited state (Figure 3.3).

As it will be better explained in the next paragraphs, linear polarization signal in this line is completely dominated by the anomalous Hanle effect that modifies the polarization vector depending on the magnetic field of the surrounding plasma. The interpretation of the line linear polarization through the Hanle effect permits to map the topology and

Ion	λ (nm)	I (ergs cm^{-2} s^{-1} sr^{-1})	P/I	$\|V/I\|$
Fe XIII...	1074.7	1.05E1	4.2E-2	2.9E-5
	1079.8	4.68E0	2.9E-3	2.8E-5
Si IX...	3934.6	1.97E-1	2.0E-3	7.9E-5
Fe X...	637.4	4.48E-1	0.00E0	1.6E-5
Fe XIV...	530.3	6.50E0	8.3E-3	1.4E-5
Si X...	1430.1	2.95E0	1.6E-2	2.9E-5

Figure 3.2: A Comparison of Polarization Properties for Several M1 Lines [Judge et al., 1998], where P/I is the degree of linear polarization and V/I is the degree of circular polarization.

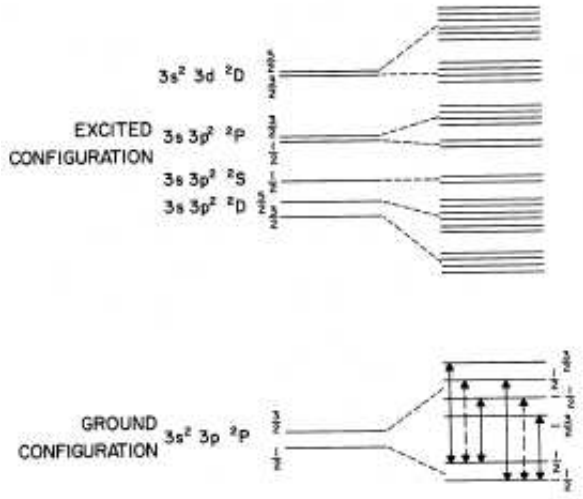

Figure 3.3: Energy level structure in ground and excited configurations of FeXIV ion [House, 1974].

the dynamics of the magnetic field in the E corona. Some insight into magnetic field topology is provided by the comparison between the observed line polarization and that one computed from models of the coronal magnetic fields, derived from force-free measurements of the photospheric field extrapolated up to the coronal levels with a numerical code (″FORWAD ‶) developed by the High Altitude Observatory.

3.2 Light polarization

Emitted light travels in electromagnetic plane waves from an astrophysical source towards the Earth.

Plane waves are described by oscillating electric ($\vec{E}$) and magnetic ($\vec{B}$) fields, whose field vectors are generally orthogonal to each other and the direction of propagation.

By convention, astronomers describe the polarization of light only in terms of the electric field vector (because $\vec{E}$ and $\vec{B}$ are orthogonal) [Hecht, 1975].

Defined a set of three Cartesian coordinates, where the z-axis represents the direction of propagation of the wave, the electric field lies in the xy plane; for a monochromatic wave with constant intensity its components are:

$$E_x(t) = E_{0x}\cos(\omega t + \delta_x(t))E_y(t) = E_{0y}\sin(\omega t + \delta_y(t)) \tag{3.1}$$

where the relative phase is:

$$\delta(t) = \delta_x(t) - \delta_y(t) \tag{3.2}$$

If the relative phase is constant in time, the radiation is completely polarized: *E(0,t)* is described by a Lissajous curve called "polarization ellipse".

The orientation of the ellipse of polarization is given by the angle ψ:

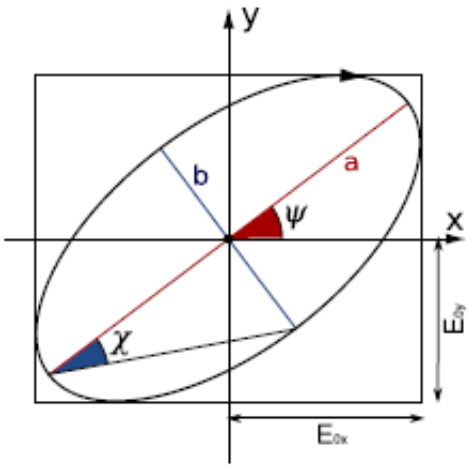

Figure 3.4: Polarization ellipse [Balboni, 2009].

$$\tan 2\psi = \frac{2E_{0x}E_{0y}}{E_{0x}^2 - E_{0y}^2}\cos\delta \tag{3.3}$$

The shape of the ellipse is instead described by the angle χ said "angle of ellipticity":

$$\tan\chi = \frac{\pm b}{a} \tag{3.4}$$

For $\delta = 0$, the ellipse degenerates into a segment ($\chi = 0$), the radiation is linearly polarized with the direction:

$$\tan\alpha = \frac{E_{0y}}{E_{0x}} \tag{3.5}$$

If $\delta = \pi/2$ and $E_{0x} = E_{0y}$ the ellipse degenerates into a circle. In this case, radiation is circularly polarized (Figure 3.5).

When the relative phase is not constant in time but several randomly, for which the time average worth $\langle\delta(t)\rangle = 0$, the light is completely not polarized and it is an incoherent superposition of linearly polarized light. Between these two extremes there is the case of the partially polarized light which is a superposition of a completely polarized part with a completely unpolarized one, whose degree of polarization is given by the ratio of the amplitudes of the two components.

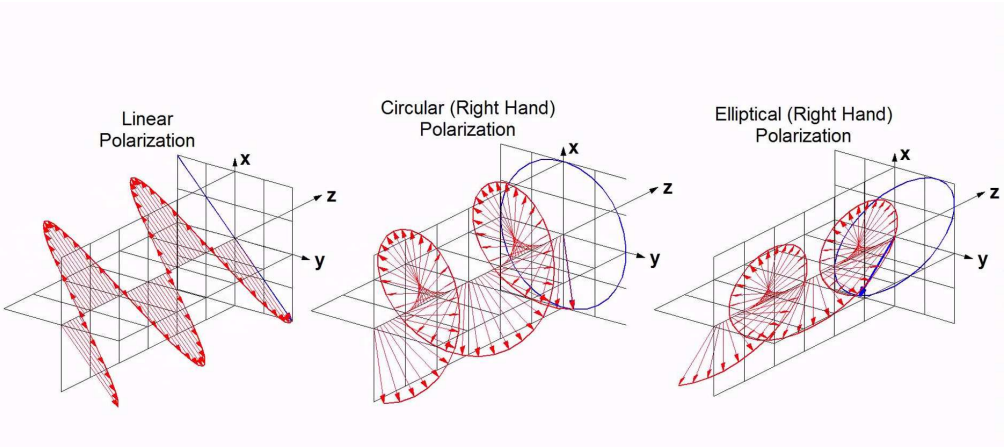

Figure 3.5: Different kinds of light polarization.

3.2.1 Stokes Parameter

In 1852, Stokes introduced four parameters $[I\ Q\ U\ V]$, to describe the polarization of light defined from radiation intensity values, experimentally measured:

$$I = E_{0x}^2 + E_{0y}^2 \tag{3.6}$$

$$Q = E_{0x}^2 - E_{0y}^2 \tag{3.7}$$

$$U = 2E_{0x}E_{0y}\cos\delta \tag{3.8}$$

$$V = 2E_{0x}E_{0y}\sin\delta \tag{3.9}$$

Their physical meanings are:

- I is the radiation total intensity;
- Q is the difference between the intensity of vertical polarized radiation and the horizontal one;
- U is the difference between the intensities of radiation polarized at $\pm\frac{\pi}{4}$;
- V is given by the difference between the light with right circular polarization and the light with left circular polarization;

Stokes parameters can be organized in a column matrix called *Stokes vector*:

$$S = \begin{bmatrix} I \\ Q \\ U \\ V \end{bmatrix} \tag{3.10}$$

For the root of Stokes parameters vector is valid the relation:

$$I \geqslant \sqrt{Q^2 + U^2 + V^2}$$

if

$$I = \sqrt{Q^2 + U^2 + V^2}$$

polarization in called *completely polarized* [Landi, 2008].
Defined the intensity of linearly polarized light as

$$pI \equiv \sqrt{Q^2 + U^2} \tag{3.11}$$

it is possible to define the direction of polarization β (from Eq. 3.3 with $\psi = \beta$) and the degree of linear polarization p as:

$$\beta = \frac{1}{2}\arctan(\frac{U}{Q}) \tag{3.12}$$

$$p = \frac{pI}{I} \tag{3.13}$$

Defined the properties of light through the four Stokes polarimetric parameters described above, it is possible to express any polarimetric element via a 4×4 matrix, said Muller matrix M, for which we will have:

$$S^{'} = M \cdot S \tag{3.14}$$

where S is the Stokes'vector on the radiation incident on a polarimetric element instead $S^{'}$ is the one related to the outgoing radiation. In the case of more than one polarimetric element, it's necessary to consider in the previous equation the product of all elements Muller matrix M_i, from the one nearest to the detector to the farthest:

$$S^{'} = \prod_{i=1}^{n} M_i \cdot S \tag{3.15}$$

Once the Muller matrix is known it is possible to derive Stokes parameters of the light incident on the polarimeter.

In general considering ρ_k, with $k \in [0, 3]$ three different angles of a linear analyser(a rotation is half delay) then the signal m_k recorded by an ideal sensor will be:

$$m_k = \frac{1}{2}(I + Q\cos(2\rho_k) + U\sin(2\rho_k)) \tag{3.16}$$

which in matrix form can be written as:

$$\begin{bmatrix} m_0 \\ m_1 \\ m_2 \end{bmatrix} = \frac{1}{2} \begin{bmatrix} 1 & \cos(2\rho_k) & \sin(2\rho_k) \\ 1 & \cos(2\rho_k) & \sin(2\rho_k) \\ 1 & \cos(2\rho_k) & \sin(2\rho_k) \end{bmatrix} \begin{bmatrix} I \\ Q \\ U \end{bmatrix} \tag{3.17}$$

3.2.2 Polarization of K corona

When an electromagnetic wave is incident on a charged particle, the electric and magnetic components of the wave exert a Lorentz force on this charge, setting it into motion. Since the wave is periodic in time, so it is the motion of the particle.

Thus, the particle is accelerated and, consequently, emits radiation. More exactly, energy is absorbed from the incident wave by the particle and re-emitted as electromagnetic radiation. Such a process is clearly equivalent to the scattering of the electromagnetic wave by the particle. Given a plane wave not polarized, Thomson scattering will produce light

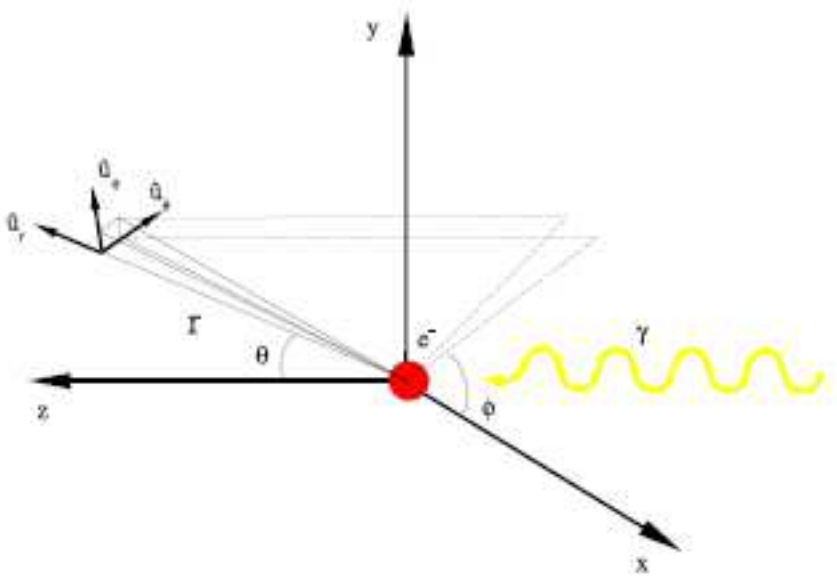

Figure 3.6: Diagram of Thomson scattering in which an electromagnetic wave coming along the z-axis impinges upon an electron at rest in the origin of the system of reference [Balboni, 2009].

partially linearly polarized, having a degree of polarization therefore zero for an observer along the z axis, and unit for an observer placed in the xy plane (Figure 3.6).
The light of the corona K, coming from the Thomson scattering, it is therefore polarized tangentially to the solar limb, but only partially: it is due to some geometrical factors, to diffusion processes and to the physical characteristics of the solar corona[van the Hulst, 1950]. The Sun is not a point source but has an angular size, for which the wave incident on the single electron is not flat; therefore it is not possible to identify a plane perpendicular to propagation direction of the incident beam in which the scattered radiation is completely polarized. Moreover, since the solar corona is optically thin, the radiation that reaches an observer from a given direction is the sum of contributions along the line of sight, each contribution with a different angle value θ and therefore different degree of polarization [Landi, 2008].

3.2.3 Polarization of E corona

Forbidden emission lines are magnetic dipole M1 transitions between levels of ground terms of ions of abundant elements of the third and fourth rows of the periodic table of elements.

The process of resonance fluorescence gives rise to coronal emission-line polarization. The scattering of radiation by resonance lines will in general lead to linearly polarized light, even in the absence of a magnetic field and an analysis of the resulting spectropolarimetric line profile provides information on the distribution of scatterers (Figure 3.7). The linear polarization vector of the E-corona emission-line is directed radially to the solar limb (magnetic dipole emission).

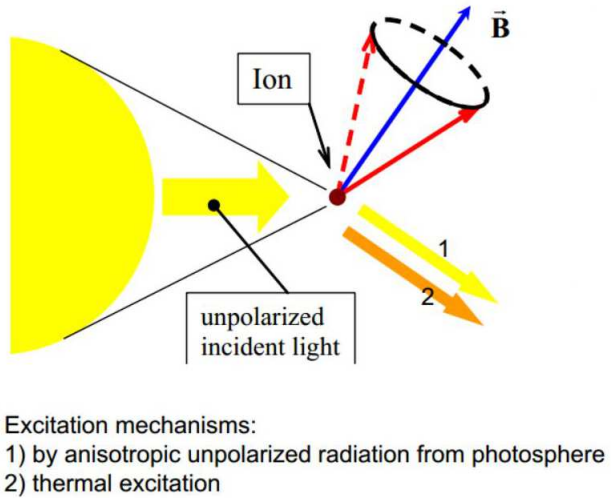

Figure 3.7: Coronal emission.

In the presence of a magnetic field, the well-known Zeeman effect can alter dramatically both the intensity and the polarization of the line emission.

However, a lesser known atomic process called the *Hanle effect* leads to a modification of the linear polarization arising from resonance-line scattering, in contrast to the circular polarization associated with the Zeeman effect. Moreover, the Hanle effect has sensitivities to magnetic field in the sub-kilogauss regime.

The discovery of the Hanle effect dates back to the early part of the twentieth century, when [Hanle, 1024] found that the change in the linear polarization of resonance-scattered radiation in the presence of a magnetic field was related to the radiative lifetime of the atomic transition. Atomic physicists have used the Hanle effect to derive transition probabilities by observing the response of the polarimetric signal to a known magnetic field.

The consequences of the Hanle effect for resonance-line scattering polarization can be explained in terms of the classical damped oscillator model for the scattering of radiation by a bound electron.

In the classical model, the absorption of light will induce oscillations of the atom in two orthogonal directions. The basic physics of the Hanle effect is that the components of the electron motion that are transverse to the magnetic field will be made to precess, owing to the Lorentz force on the electron. If there were no magnetic field present, the atomic oscillator would emit radiation at a fixed position angle, but with a magnetic field, the atom is caused to emit at a sequence of position angles. This precessional motion of the electron is called *Hanle precession.* For a free electron, the distribution of scattered light is a superposition of two orthogonal dipole oscillators. However, scattering by a resonance line differs from a free electron in that the scattering is partly dipolar (like a free electron) but also partly isotropic. For resonance lines the relative contributions depend on the j quantum number of the lower level and the Δj of the transition.

In order to describe the magnetic field dependence of the linear polarization in the "green line", it is convenient to distinguish between two magnetic field intensity regimes: the "Hanle effect sensitive"regime and the "saturated Hanle effect"regime.

In the Hanle effect sensitive regime, the linear polarization signal is affected by both the intensity and the direction of the magnetic field, while in the saturated regime the scattered linearly polarized radiation is insensitive to the magnetic field strength so only information on the orientation of the field vector in the plane of sky is retained [Krebs et al.,2009].

The Hanle diagnostic is most sensitive to the magnetic field strength at which the Larmor frequency ω_L is greater than the inverse lifetime of the excited state, γ, called also ″strong field‟. Thus in a strong field an ion precesses many times between the absorption and re-emission event. The critical field strength is given as:

$$\frac{\omega_L}{\gamma} = \frac{eB_c g_{eff}}{4\pi mc\gamma} = 1 \tag{3.18}$$

$$B_c = 3.6 \cdot 10^{-7} A/g_{eff} \tag{3.19}$$

where e, m, and c have their usual meaning and where A is the Einstein transition probability and g_{eff} is the "effective"Lande g-factor [Bueno et al., 2002].

For forbidden lines, A is on the order of 100 sec^{-1}, geff $\sim$ 1; thus the critical field is a few times 10^{-5} Gauss. For essentially all coronal regions we may, considering that that the typical value of the coronal magnetic field B_{cor} is 10–10^{-3} G and that the forbidden lines magnetic fied B_{FL} is less than B_{cor}, use the strong field approximation [House, 1974]. In this case the direction of linear polarization can be only parallel or perpendicular to the magnetic field projected in the plane of the sky, depending on the so called *Van Vleck effect*.

Van Vleck effect, completely depolarizes scattered radiation when the incident field lies at an angle of θ_{vv}=**54.7°**, called *Van Vleck* angle, to the magnetic field (the angular value is given from the condition $3\cos^2\theta_{vv}$-1=0, that is $\theta_{vv} = 1/\sqrt{3}$) .

Furthermore, after the Van Vleck angle is passed the polarization is negative, which means that the plane of polarization is perpendicular to the magnetic field (Figure 3.8).

It should be apparent that this effect can introduce difficulties into the interpretation of polarization data.

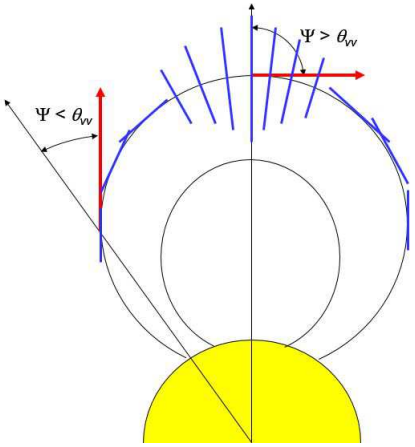

Figure 3.8: A schematic rapresentation of the Hanle effect. If the angle of the magnetic field (black arrow) with respect to normal to photosphere (red arrow) is larger or smaller of the Van Vleck angle,linear polarization(blue line) becames respectly perpendicular or parallel to the magnetic field direction [Lin, 2011].

Chapter 4

The CorMag instrument

4.1 Introduction

Coronal data analysed in this thesis were acquired by the INAF Turin Astronomical Observatory "CorMag"telescope during the total solar eclipse of 11/07/2010 in Tatakoto Atoll (French Polynesia).
The instrument was calibrated two times: before the eclipse (2010) and after the eclipse (2014).
One of the goal of my thesis is the post eclipse calibration of the CorMag and the control software implementation of the CorMag instrument, in view of its integration to the Lomnicky ZEISS coronagraph (Slovakia).
This chapter describes its technical characteristics and the results of the pre and post eclipse calibrations.

4.2 CorMag technical description

The CorMag (Coronal Magnetograph) instrument is a spectro-polarimeter telescope designed for the detection and the spectropolarimetry of the solar corona FeXIV emission line, 530.3 nm, during total solar eclipse observations.

In its optical layout (figure 4.1), starting from the left side, there are (for specifics see Table 4.1):

Figure 4.1: CorMag optical layout [Capobianco et al., 2011].

- An achromatic doublet of objective lens (O);
- a field stop (FS);
- a collimator triplet (COT);
- a Liquid Crystal Tunable Filter and Polarimeter(LCTP);
- a camera triplet (CaT);
- the detector focal plane (DFP).

To follow some specifics of the CorMag instrument:

Effettive focal	800 mm
Aperture	60 mm
F/♯	13.3
Platescale	6.2 arcsec/px

The *plate scale* is the the number of arcseconds that each pixel of the CCD spans.
The Liquid Crystal Tunable Filter (LCTF) is a device that exploits the properties of some nematic birefringent liquid crystal: oblong crystal molecules tend to align along the lines of an applied electric field, and in the absence of the latter, not parallel with each other.
The lamina of delay is composed of a cell of a few micrometers thick filled with the liquid crystal and delimited by two flat and parallel windows between them, made of molten silicon MK7.
On the inner face of the two windows is deposited a thin transparent conductive coating of indium and tin oxide (ITO), and a dielectric layer on top of this finely engraved along a direction.
The polarimetric block with the LCTF and the relay optics have a length of 282.9 nm.

The filter, used for CorMag, is a customized version of a standard product line of Meadowlark Optics (Figure 4.3). It is a bandpass filter with a full width at half maximum of 0.15 nm at a wavelength of 530.3 nm. The center wavelength of the bandpass is tunable in 0.01 nm steps from 528.64 nm to 533.38 nm. It is a four stage Lyot filter with all four stages wide-fielded using split elements with intervening half wave retarders.
The free spectral range between neighbouring transmission bands of the filter is more than 2.7 nm.
The filter is passively thermally compensated so that the wavelength change with temperature is less than 0.003 nm/℃ over the temperature range of approximately 21℃ to 26 ℃. The bandpass center wavelength is computer controlled using Meadowlark Optics standard filter controller with software modified to permit the fine-tuning steps required for this application.
The filter has an attached *linear polarization rotator (LPR)* that permits non mechanical user control of an input linear polarization direction over a 180° range using LCVRs (Figure 4.2).

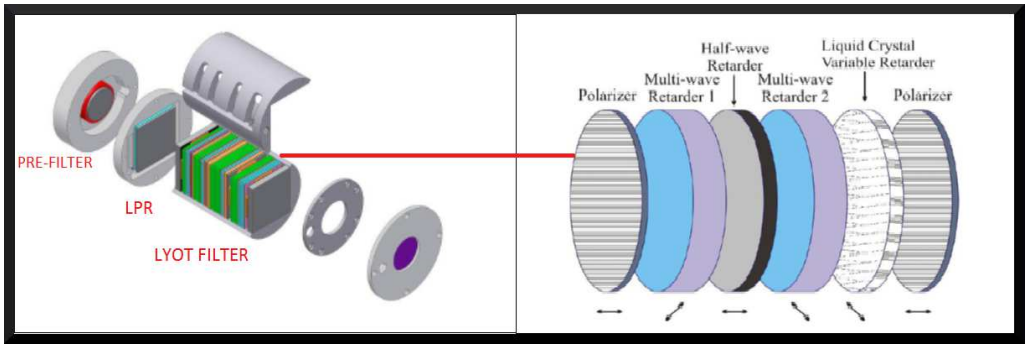

Figure 4.2: LCVR mechanical layout with a view of one Lyot filter stage [Capobianco et al., 2011].

The LPR is also controlled with the filter controller. There is also an attached pre-filter from Andover Corporation with a full width at half maximum of 1.89 nm and a center wavelength of 530.69 nm.
There is a small heater attached to the cell of this pre-filter to control its temperature to 23℃since it has a temperature wavelength shift of 0.017 nm/℃, much higher than the tunable filter.
The filter is 60 mm in diameter and 90 mm long with a clear aperture of 20 mm. The

Figure 4.3: The filter prior to adding the electrical connector for LCVR control [Fineschi et al., 2010b].

Mueller matrix of the LPR with included the is given by
$M_{LPR'} = M_{POL}(0) \cdot M_{LCP}(\delta) = M_{POL}(0) M_{LCVR}(\delta) \cdot M_{QWLR}(\pi/2)$ where [Shurcliff, 1962]

$$M_{POL}(0) = \begin{pmatrix} 1 & 1 & 0 & 0 \\ 1 & 1 & 0 & 0 \\ 0 & 0 & 0 & 0 \\ 0 & 0 & 0 & 0 \end{pmatrix} \tag{4.1}$$

is the Mueller matrix of the linear polarimeter,

$$M_{LCVR}(2\delta) = \begin{pmatrix} 1 & 0 & 0 & 0 \\ 0 & cos\delta & -sin\delta & 0 \\ 0 & 0 & 1 & 0 \\ 0 & sin\delta & 0 & cos\delta \end{pmatrix} \tag{4.2}$$

is the Mueller matrix of the LCVR and

$$M_{QWLR}(\pi/2) = \begin{pmatrix} 1 & 0 & 0 & 0 \\ 0 & 1 & 0 & 0 \\ 0 & 0 & 0 & 0 \\ 0 & 0 & -1 & 0 \end{pmatrix} \tag{4.3}$$

is the Mueller matrix of the quarter wave retarder layer.

$$M_{LCP}(\delta) = \begin{pmatrix} 1 & cos\delta & sin\delta & 0 \\ 0 & cos\delta & sin\delta & 0 \\ 0 & 0 & 0 & 0 \\ 0 & 0 & 0 & 0 \end{pmatrix} \tag{4.4}$$

Substituting $2\rho_k$ with the nominal LCVR retardance δ_K equation 3.17 becomes:

$$\begin{bmatrix} m_0 \\ m_1 \\ m_2 \end{bmatrix} = \frac{1}{2} \begin{bmatrix} 1 & \cos\delta_0 & \sin\delta_0 \\ 1 & \cos\delta_1 & \sin\delta_1 \\ 1 & \cos\delta_2 & \sin\delta_2 \end{bmatrix} \begin{bmatrix} I \\ Q \\ U \end{bmatrix} \tag{4.5}$$

CorMag instrument is blind to circular polarization, so we can ignore the V parameter.

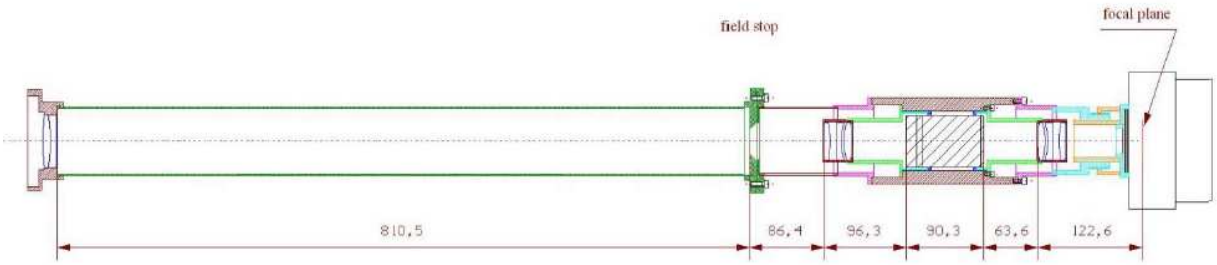

Figure 4.4: CorMag mechanical draw [Capobianco et al., 2011].

4.2.1 Filter test

The filter was tested at Meadowlark Optics on a 0.85 meter f/7.8 double Czerny Turner spectrometer. This instrument is a double grating 0.85-meter Czerny-Turner spectrometer.

The gratings are 1800 lines/mm with a clear aperture of 102 mm. They are blazed at 17 27 which corresponds to a wavelength of 330 nm in first order. The system has an f ratio of f/7.8.

Either a silicon photodiode or a photomultiplier are used as the detector at the exit slit. The entrance and exit slits are adjustable from a width of 10 microns to about 2.5 mm. The scale at the exit slit is 0.31 nm/mm.

The spectrum is scanned by a custom computer controlled stepper motor drive system

developed by Meadowlark Optics, which rotates the gratings in unison. The entrance and exit slits were set to 20 microns for most tests, which corresponds to about 0.005 nm spectral width since the plate scale is approximately 0.25 nm/mm. The intermediate slit width between the first and second gratings is 1 mm, which is a spectral bandwidth of 0.25 nm.

The filter was tested in a collimated beam from a quartz tungsten halogen light source preceding the entrance slit of the spectrometer. The full aperture of the filter was illuminated for the test results in this report except for the study of variation of the spectral bandpass with angle of incidence.

The wavelength calibration is checked using a neon line source with an emission line at 533.078 nm. Calibration is stable to ± 0.005 nm over a period of several weeks (Figure 4.7). The detector at the spectrometer exit slit is a Hamamatsu H5784-04 photomultiplier tube. Spectral measurements were made at a wavelength step interval of 0.004 nm.

Is is found a good agreement between our measurements and the modelled results (Figure 4.5). The measured full width at half maximum of the filter profile is 0.15 nm. The measured peak transmission of the filter is 29% for polarized light. The error on the peak transmission measurement is ± 3% because of the difficulty of avoiding walk-off of the beam on the spectrometer entrance slit when the filter is inserted in the collimated test beam.

As stated the filter center wavelength is tunable in steps as small as 0.01 nm from 528.64 nm to 533.38 nm. The tuning is non-mechanical using LCVRs. Additionally the filter has a fail state, zero voltage transmission profile centered at 530.34 nm (Figure 4.6) Tests show that the filter is quite stable over time and for a range of temperatures (figure 4.8).

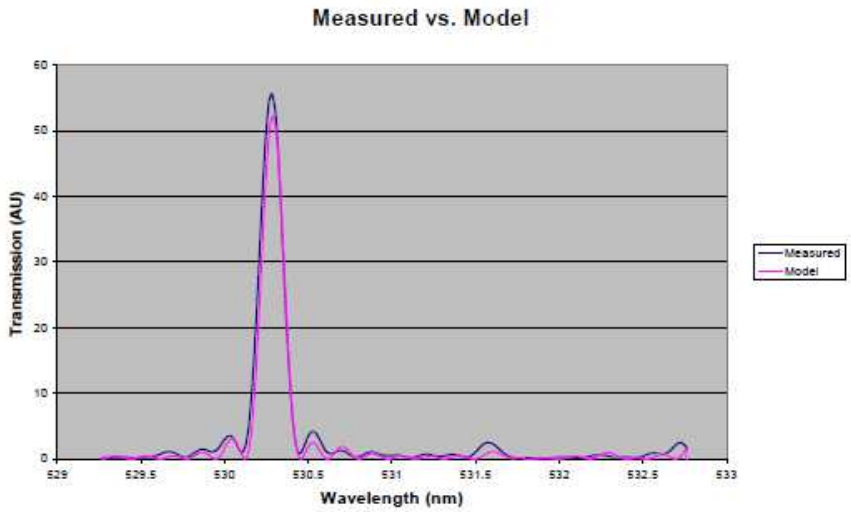

Figure 4.5: Comparison between the modeled and measured filter profile at a wavelength of 530.0 nm. The transmission scale is linear but is in arbitrary units [Fineschi et al., 2010b].

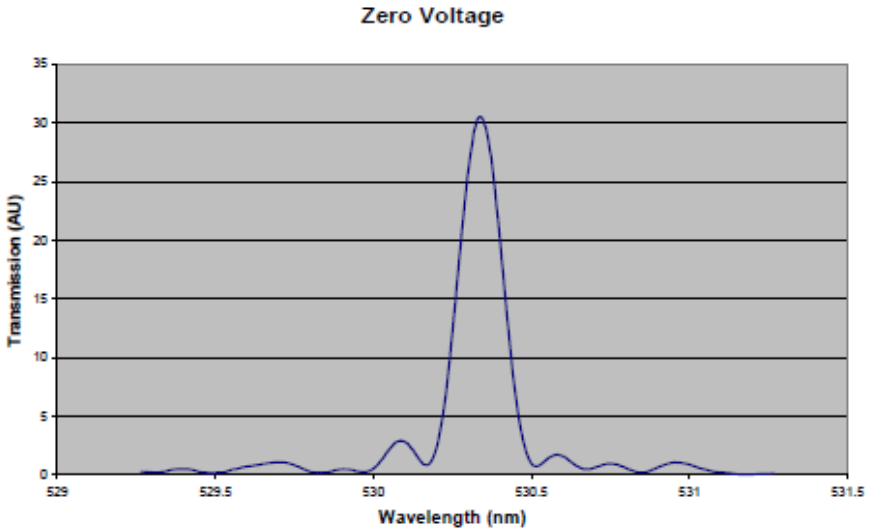

Figure 4.6: The fail state transmission profile of the filter. It centers at a wavelength of 530.34 nm [Fineschi et al., 2010b].

Although the tuning steps here are 0.02 nm, they can be as small as 0.01 nm using the Meadowlark controller. There is only a small change in the filter wavelength over angle of incidence (almost there are no changes for angles smaller than 6°).

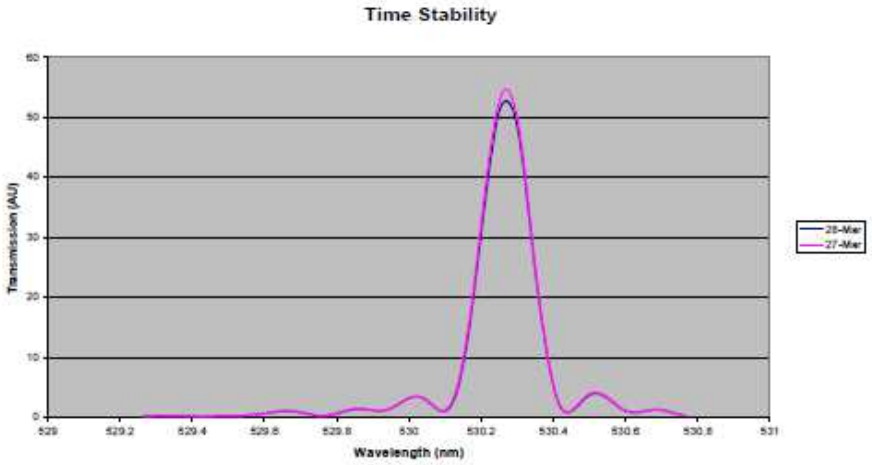

Figure 4.7: The filter profile measured on two successive days when electrically driven to a wavelength of 530.3 nm. [Fineschi et al., 2010b]

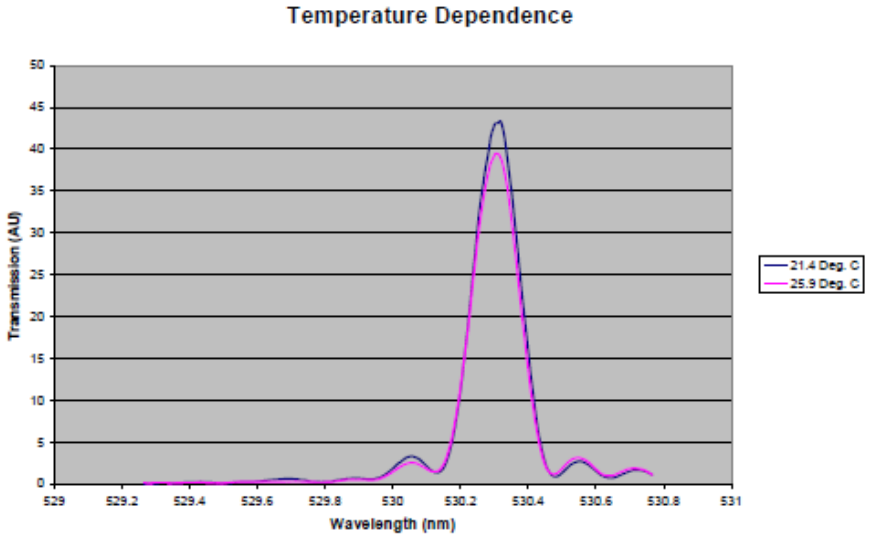

Figure 4.8: The thermal stability of the filter which uses a passive thermal compensation scheme [Fineschi et al., 2010b].

At 6°the shift is approximately 0.03 nm. The transmission change with angle of incidence is due to a test system efficiency change with angle of incidence and does not represent a real change in filter performance.

The transmission efficiency changes with angle of incidence because of beam walk on the spectrometer entrance slit. Figure 4.11 shows that there is a small difference between the requested(Ask) wavelength, using the filter controller and the measured wavelength. All

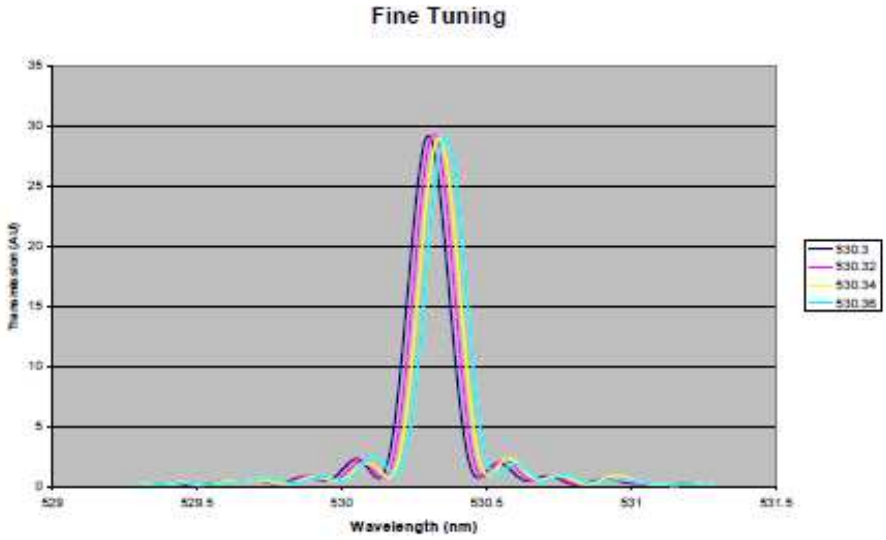

Figure 4.9: The fine tuning capability of the filter [Fineschi et al., 2010b].

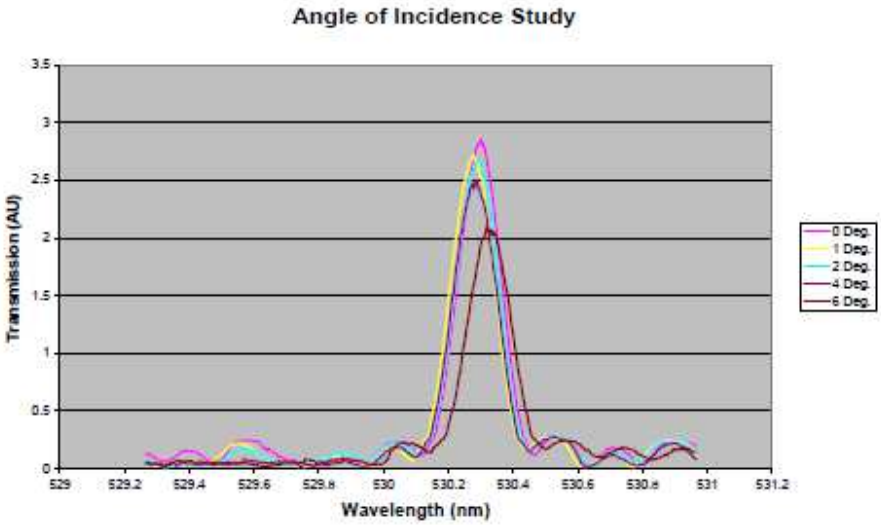

Figure 4.10: The small dependence of the filter center transmission wavelength on angle of incidence [Fineschi et al., 2010b].

units here are nm and the difference is less than 0.04 nm for all wavelengths checked.

4.3 The CorMag instrument control software (ICS)

The main objective of the CorMag instruments control software software is, as the name says, the control of the CorMag devices and the data acquisition.

Two operative mode are provided: the *manual* control and a *sequential* mode C&DAQ

Ask	Wavelength	Offset
529.8	529.762	-0.038
529.9	529.88	-0.02
530	529.989	-0.011
530.1	530.082	-0.018
530.2	530.179	-0.021
530.3	530.274	-0.026
530.4	530.39	-0.01
530.5	530.479	-0.021
530.6	530.589	-0.011
530.7	530.673	-0.027
530.8	530.804	0.004
531.3	531.295	-0.005

Figure 4.11: Wavelength offset (Tunable Filter Test Report,S. Fineschi,T.Baur and P. Wagner, 2010).

(control and data acquisition) that allow the user to run a script that sequentially configure the instrument and acquire the frame.
Instrumental devices controlled by PC are:

- The LCTP (Liquid Crystal Tunable-filter and Polarimeter)
- The CCD camera

CorMag ICS requires a desktop or laptop PC with the follows requirements:

- RAM: min 256 MB
- OS: Windows 2000/XP/Vista/7
- Software: NI LabVIEWTM 9.02 USB port

In Figure 1.12 is shown the screenshot of the main page of the CorMagICS software.
On the right side there are the buttons for *Manual Mode*, *Sequential Mode* and *Exit*. Below there is the log of the operations. In the middle there is the frame acquired and on the left side there are the current parameters for the LCTP and for the CCD camera.

4.3.1 Check and initialize device

After running the software, it automatically check if the two devices are connected and it is necessary to initialize the connected devices to these values: **1-CCD CAMERA**

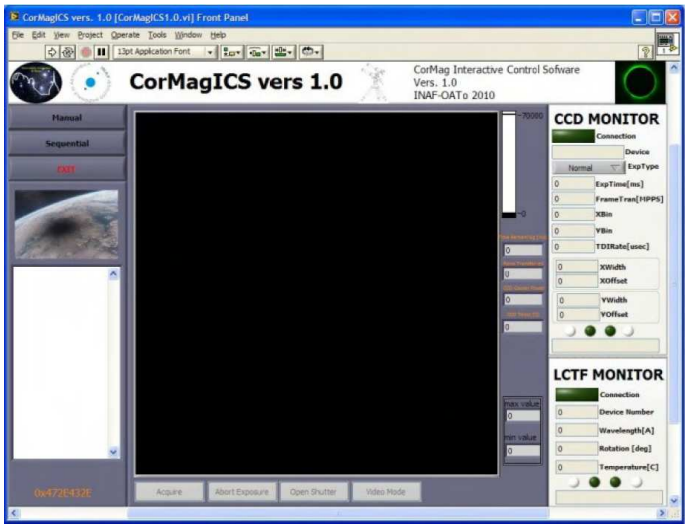

Figure 4.12: CorMagICS main page [Capobianco, 2010].

- Exposure type: Light frame;
- Exposure Time: 1000 ms;
- X Binning: 1;
- Y Binning: 1;
- X Width: 1024;
- X Offset: 0;
- Y Width: 1024;
- Y Offset: 0;
- TDI Rate: 0 μs;
- Frame Transfer: 3.3 MPPs;
- CCD Temperature: -30 ℃;
- Background Flush Sensor: Active;

2-LCTP

- Wavelength: 5303.0 Å

- LCTP Rotation: 0 deg.

The blue led indicator show when default values are applied to the devices.
After the initialization the software is ready for data acquisition and wait that the user select for one of the two operative modes (Figure 4.14):

- **Manual mode**

  The manual mode allows the manual control of the connected devices.In order to change the parameters, after the selection of new values, the *Change* button for LCTF or CCD Camera must be pressed. The commands for data acquisition are under the frame.

  Pressing the relative button is possible to start the acquisition (Acquire), abort the acquisition (Abort Exposure) and manually open/close the shutter (Open/Close Shutter).

- **Sequential mode** This modality allows the selection of a script used by the software to sequentially apply the relative parameters to the instrument and to acquire the data.

  By pressing the *Sequential* button in the main page, the user can select the script to be run. The script files need to have an extension .seq. This files are simply ASCII files.

  After the selection of the script, the software checks if this is compatible with the format required and after that it is ready to start with the sequence. Before starting the sequence, the software asks for an input from the user.

  The user can check the current values on the monitors of the CCD and of the LCTF. The maximum and the minimum counts of the last frame are also displayed.

All the acquired frames are automatically saved in fits file standard.
The filename is $CorMagImage\_YYYY.MM.DD.hh.mm.ss.fits$.
The frames are 1024x1024 pixels with depth of 16 bit.
The header of the fits files have the keywords reported in Figure 4.13 .
Recently some changes have been done to the software as:

- In the calibration mode it has been added a control for the pre-polarizer rotation;
- In the interface has been added a panel with the name of the operator;

```
SIMPLE  =                    T/Conform to FITS Standard          (Mandatory for fits standard)
BITPIX  =                   16/Number of bits per pixel          (Mandatory for fits standard)
NAXIS   =                    2/Number of axes in the image       (Mandatory for fits standard)
NAXIS1  =                 1024/Length of the first axis (columns)(Mandatory for fits standard)
NAXIS2  =                 1024/Length of the second axis (rows)  (Mandatory for fits standard)
EXTEND  =                    T/
FILENAME='CorMagImage_2010.07.'/Name of the fits file
INSTRUM =                CorMag/Instrument name
TELESC  ='Focal:800;Aperture:60/Telescope parameters in mm
DETECTOR=ProLine PL1001 FWRev:2/Detector description
HPIXSIZE=                   24/Horiz Pixel Size in micron
VPIXSIZE=                   24/Vert Pixel Size in micron
CCDTEMP =                  -37/Temperature of the ccd in C
OBSEQ   =                   31/Sequential number of data acquisition
EXPTIME =              8000,00/Exposure time in milliseconds
LCTFWAVE=              5303,00/LCTF Wavelength [A]
LCTFTEMP=                24,38/LCTF Temperature in °C
LCTFROT =              120,00/LCTF Rotation in deg
DATETIME= '2010/07/11 18:50:24'/Date/Time of file generation (UT)
XBINNING=                    1/Binning along X axis
YBINNING=                    1/Binning along Y axis
PREPOL  =               'None'/Position of prepolarizer
OPAL    =               'None'/Opal type
END
```

Figure 4.13: Header keywords [Capobianco, 2010].

- At the command *exit* the CCD temperature will be automatically set at 25°;
- The addiction of new keywords in the header for fits files;
- The request of a password for the manual mode.

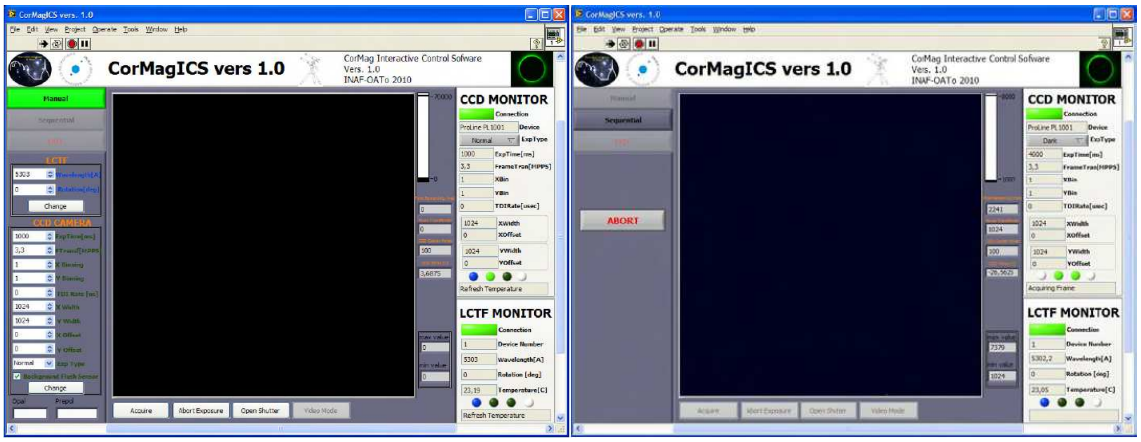

Figure 4.14: CorMagICS manual mode (left) and sequential mode (right) [Capobianco, 2010].

4.4 Post-eclipse calibration

4.4.1 The Lomnicky Stit project

After that the INAF-Turin team operated successfully the CorMag during the 2010 eclipse, the idea was to integrate this instrument to the Lomnicky Stit Observatory, Tatranska

Lomnica (SK), ZEISS coronagraph with a dedicated opto-mechanical interface developed by the Astronomical Institute of the Slovak Academy of Sciences (AISAS, Tatransk Lomnica, Slovakia) to measure with high cadence imaging spectroscopy the wave properties in corona and their possible contribution to the coronal heating, improving the understanding of the role of the coronal magnetic field as the leading driving mechanism for the heating.
Before the installation it was necessary a post-eclipse calibration, made the INAF-Turin team with my collaboration, in the OaTo optical laboratory, to verify the proper working of all CorMag components after four years from the eclipse.
The instrumentation, after the re-calibration phase which showed that all its components were still efficient, was integrated to the Zeiss coronograph in April 2014.

4.4.2 Camera calibration

The Cormag instrument is now equipped with a new CCD camera: ProLine PL1001E.
A CCD camera consists of a large number of light-sensing elements arranged in a two-dimensional array on a thin silicon substrate. The semiconductor properties of silicon allow the CCD chip to trap and hold photon-induced charge carriers under appropriate electrical bias conditions. Individual picture elements, or pixels, are defined in the silicon matrix by an orthogonal grid of narrow transparent current-carrying electrode strips, or gates, deposited on the chip. The fundamental light-sensing unit of the CCD is a metal oxide semiconductor (MOS) capacitor operated as a photodiode and storage device (Figure 4.15).
Electrons liberated by photon interaction are stored in the depletion region up to the full well reservoir capacity. When multiple detector structures are assembled into a complete CCD , individual sensing elements in the array are segregated in one dimension by voltages applied to the surface electrodes and are electrically isolated from their neighbours in the other direction by insulating barriers, or channel stops, within the silicon substrate.
The light-sensing photo-diode elements of the CCD respond to incident photons by absorbing much of their energy, resulting in liberation of electrons, and the formation of corresponding electron-deficient sites (holes) within the silicon crystal lattice. One electron-hole pair is generated from each absorbed photon, and the resulting charge that accumulates

in each pixel is linearly proportional to the number of incident photons. External voltages applied to each pixel's electrodes control the storage and movement of charges accumulated during a specified time interval. Initially, each pixel in the sensor array function as a potential well to store the charge during collection, and although either negatively charged electrons or positively charged holes can be accumulated (depending on the CCD design), the charge entities generated by incident light are usually referred to as photoelectrons. This discussion considers electrons to be the charge carriers. These photoelectrons can be accumulated and stored for long periods of time before being read from the chip by the camera electronics as one stage of the imaging process.

Image generation with a CCD camera can be divided into four primary stages or functions: *charge generation* through photon interaction with the device's photosensitive region, *collection* and *storage of the liberated charge*, *charge transfer*, and *charge measurement*.

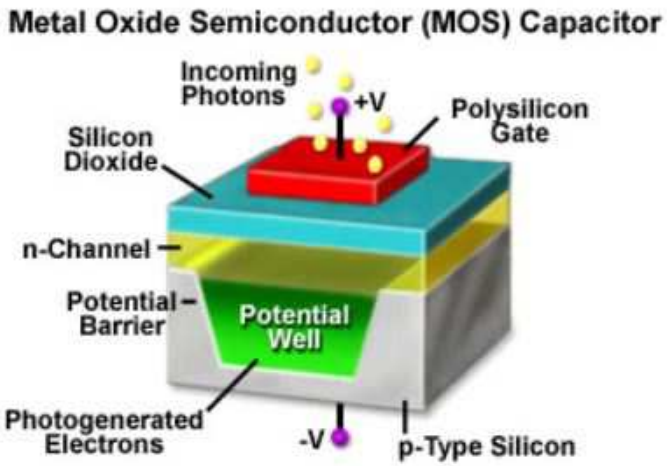

Figure 4.15: The electrode structure defining an individual CCD sense element.

The *photon transfer curve* (**PTC**) is one of the most commonly used measurement in characterizing CCD camera performance. For an array of pixels, the noise is plotted as a function of the average signal at different light levels or exposure time (Figure 4.16). PTC measurement are made initially in ADU(analog to digital unit) that will be converted to electron unit later. There are four distinct noise regimes in a PTC [Jenkins, 2010]:

1. The first regime, *read noise* (RON), represent the random noise measured under totally dark conditions.

2. With the increase, read noise gives way to photon *shot noise*, which represent the middle region of the curve. In a log-log plot this regime is characterised by a slope of 1/2.

3. The third regime is associated with pixels *fix pattern noise* (FPN), which is due to the non uniformly response of the pixels and has a typical slope of 1.

4. The fourth region occurs when the array reach the *full-well* regime. As the signal level increases we finally reach a point where the noise drops off as saturation is approached.

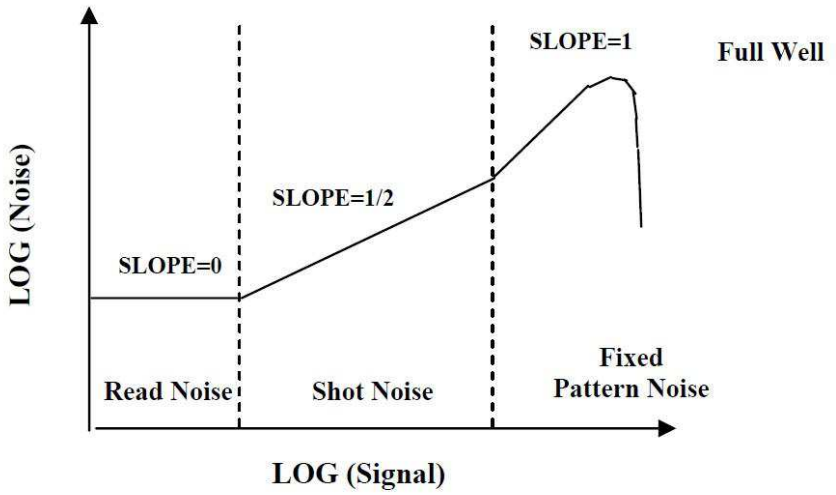

Figure 4.16: An ideal PTC response from a camera system exposed to a uniform light source [Jenkins, 2010].

The CCD camera used for laboratory calibration is, like said before, a PROLINE PL1001 with a single channel sensor, a 1025 $\times$ 1025 imaging array size and a 24 μm pixel size.
As source was used a lamp at 1.93 Watt.
For calibrations were taken sequentially 182 images of dark (shutter closed) and 182 ones with source on, all off them with a range of exposure time $\in [0s, 850s]$ with step of 50 ms.
The procedure used for calibration can be divided in three different steps:

1. To subtract from every image the corresponding one taken with the camera shutter closed;

2. To calculate the ADC Offset from the medium of the counts of a pixels column unexposed ;

3. To derive the medium intensity referred to a selected area of pixels for each frame and its standard deviation (total noise);

4. To make a plot of the signal medium intensity versus noise, both measured in ADU;

5. To remake the previous plot with a log-log scale;

6. To analyse plots and found the different contributes to the camera total noise.

All these operations have been applied to a square selection of the working area of the CCD of 500 x 500 pixels. For the measurement of PTC is also necessary to calculate the offset of the ADC, the average intensity of a column in a region little exposed and subtracting it from the average signal measured previously. The total noise, which includes read noise, shot noise and FPN, is found by the quadratic sum of the individual noise sources:

$$\sigma_{tot}(DN) = \sqrt{\sigma^2_{shot} + \sigma^2_{read} + \sigma^2_{FPN}} \tag{4.6}$$

$$\sigma_{shot}(DN) = \sqrt{S/K_{ADC}} \tag{4.7}$$

where K_{ADC} is the gain [electron/ADU];

$$\sigma_{FPN}(DN) = PN \times S \tag{4.8}$$

$$\sigma_{read}(DN) = \sigma^2_{tot} - (\sigma^2_{shot} + \sigma^2_{FPN}) \tag{4.9}$$

From the measurements taken it is possible to obtain (Figure 4.17):

1. noise vs signal plot

2. signal vs exposure time plot

The gain K_{ADC} can be found fitting the PTC curve (fig:4.16) with a line of slope 1/2 in the region of shot-noise. The signal intercept represent the value K_{ADC}. It also represents the conversion factor from DN to electrons.
The 1/PN factor can be found fitting the PTC curve with a line of slope 1 in the region of fix pattern-noise. The signal intercept represent the value 1/PN.

The parameters found are in reasonable agreement with those provided by the manufacturer at 3.3 Mpps:

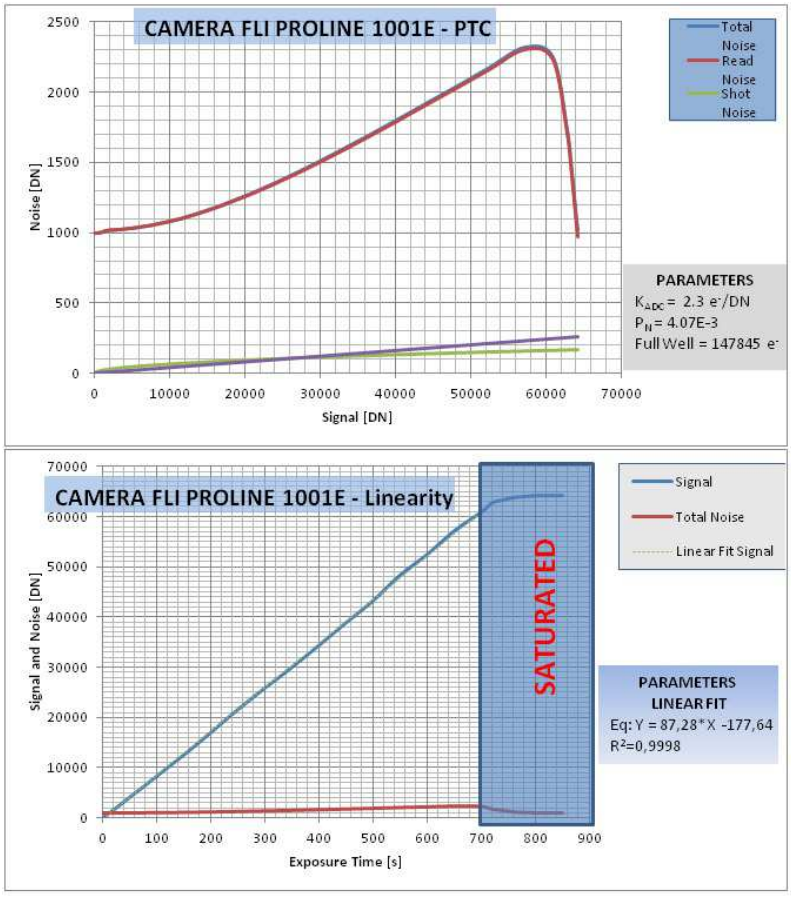

Figure 4.17: Proline PL1001E PTC and parameters (G.Capobianco, 2014).

SERIAL NUMBER	PL0291913
MODEL	PROLINE PL1001
GAIN	2.32 e^-/DN
BIAS	1007.5
RON	15.2
SATURATION	149702.6e^-

4.4.3 Other calibrations

Hot mirror

An hot mirror is a filter that prevents the passage of infrared radiation (Figure 4.18). The setup for the measure the filter trasmissivity (Figure 4.19) was the following:

Source (a 32 W lamp)$\rightarrow$ $opticfiber \rightarrow collimator \rightarrow filter \rightarrow lens \rightarrow spectrometer$

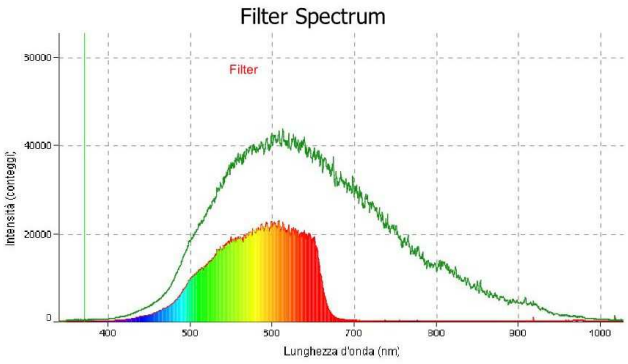

Figure 4.18: Pass-band interference filter spectrum (red) vs lamp (green)

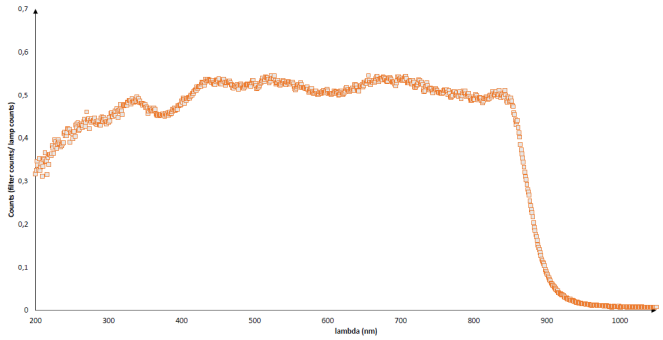

Figure 4.19: Filter transmissivity.

Trasmissivity in the range [500, 600] nm is 51.8 ⁒.

Monochromator calibration

For the monochromator calibration the sperimental setup (Figure 4.20) was the following: The source used was a Hg-Ne lamp mounted on the Oriel Fiber optic accessory with a

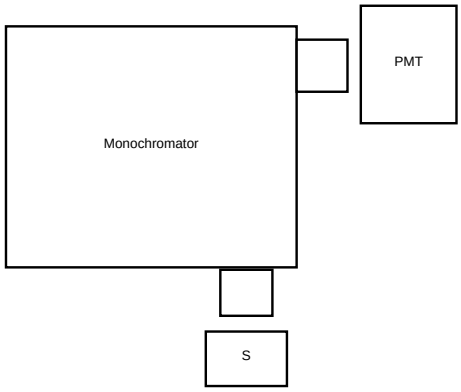

Figure 4.20: Monochromator calibration setup.

SMA adapter, the monochromator was a Oriel MS257 with a precision of 1 Å and the detector was a photomultiplier placed in front of the monochromator output slit.
Monocromator specifications are:

Slit in	28 $\pm 2\mu m$
Slit out	26 $\pm 2\mu m$
Grating	1800 p/mm
RD	21 nm/mm

The calibration has been done scanning the wavelength range of the monochromator between 425.00 and 550.00 nm with a resolution of 0.1 nm. A software that sequentially set a wavelength and after read the output light has been used.The experimental setup was appropriately shielded to reduce noise
After turning on the source its necessary to attend 30 minutes for the stability of the lamp. The first step of the data analysis is the subtraction of the dark and the evaluation of the continuum emission. Over plotting to the lamp data, the of the source provided by the manufacturer, we are able to know the offset and eventually the slope for the correct positioning of the monochromator. Detecting the wavelength of the local maximum in experimental data, plotting these versus the nominal ones (Figure 4.21-4.22) of the source

emission and fitting these data with a linear fit, we are able to evaluate the offset and the slope of our calibration (Figure 4.23).

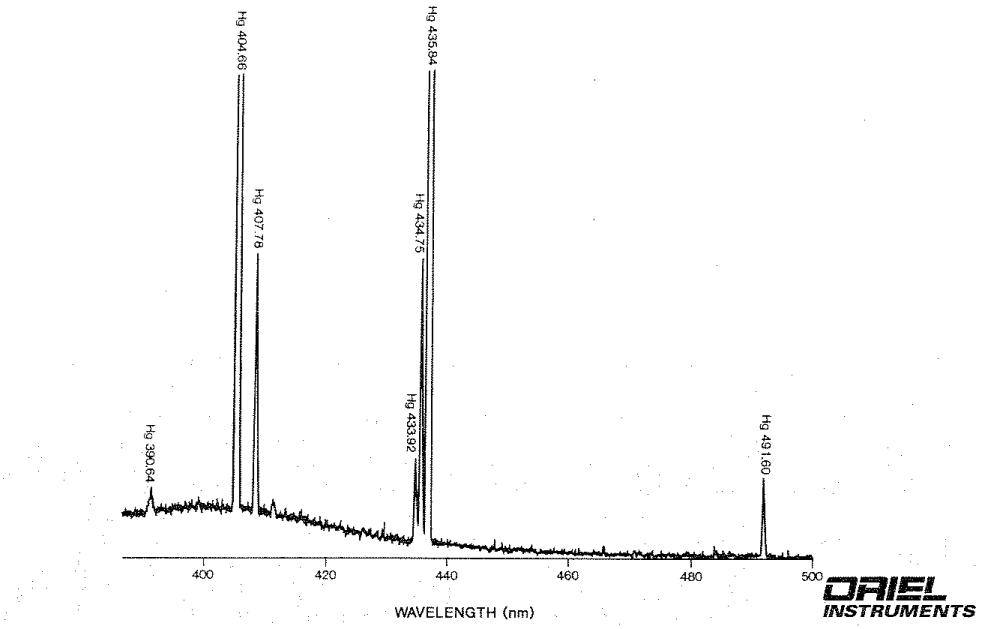

Figure 4.21: Typical line output of a 6034 mercury lamp.

The position to set the monochromator (P) in order to position to the nominal wavelength (N) is evaluated by the following equation:

$$N = (1.000449 * P) - 2.15445052 \tag{4.10}$$

where 1.000449 and 2.15445052 are, respectively, the slope and the off-set of the calibration fit.

LCTF scan

In Figure 4.24 is represented schematically the experimental setup. For the scan have been made 103 DAQ of the slit image from 5287 to 5338 Å, with steps of 0.5 Å each one with an exposure time of 60 s. The position of the monocromator was setted at 5284Å corrisponding to the nominal position of 5303.16 Å. After the dark removal, the mean

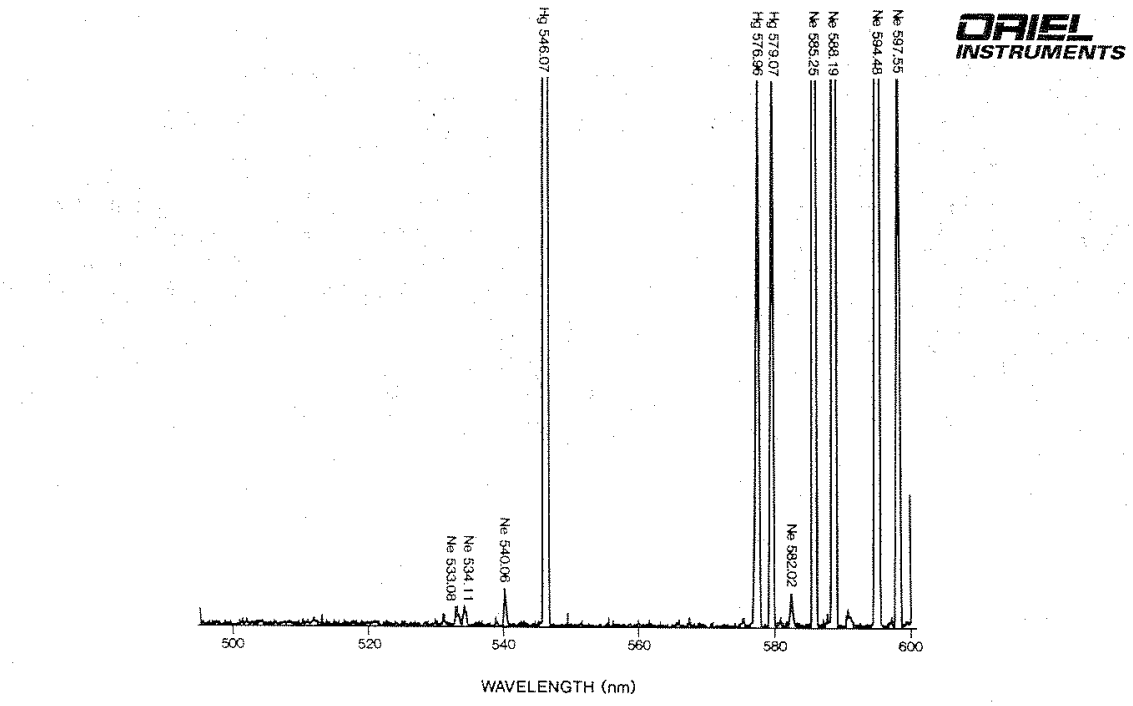

Figure 4.22: Typical line output of a 6034 mercury lamp.

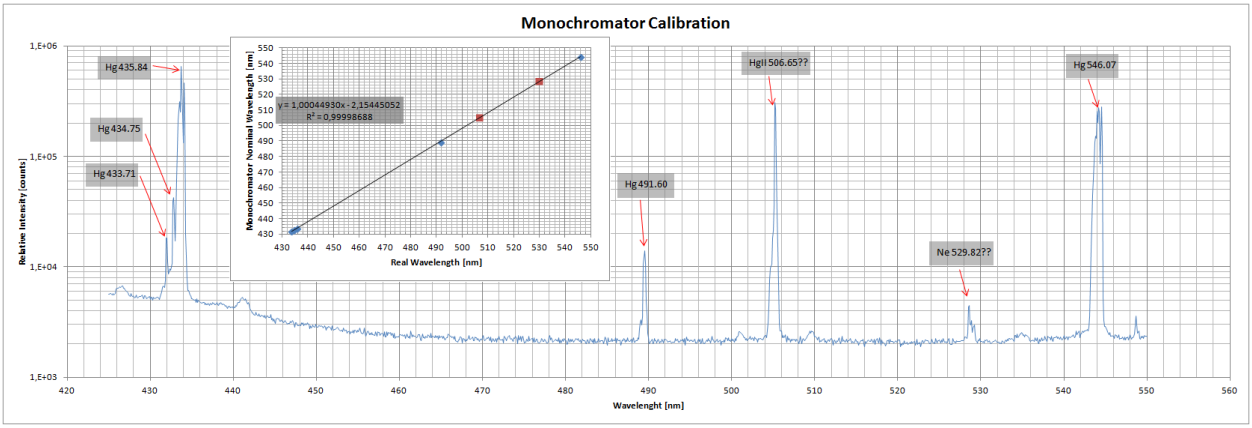

Figure 4.23: Measured line output of the 6034 mercury lamp.

intensity [counts] of each slit image was plotted as a wavelength function in order to find the peak of intensity (Figure 4.25).

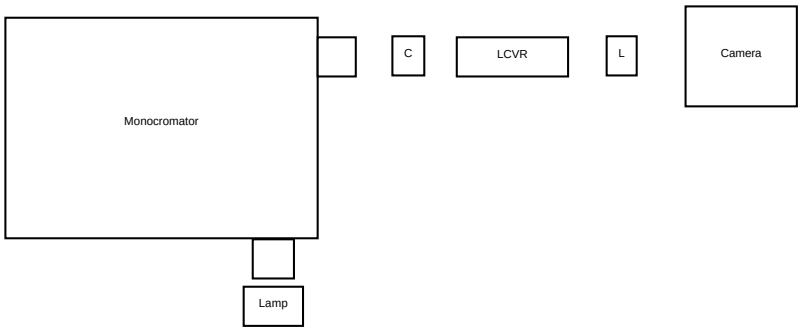

Figure 4.24: LCVR scan instrumental setup

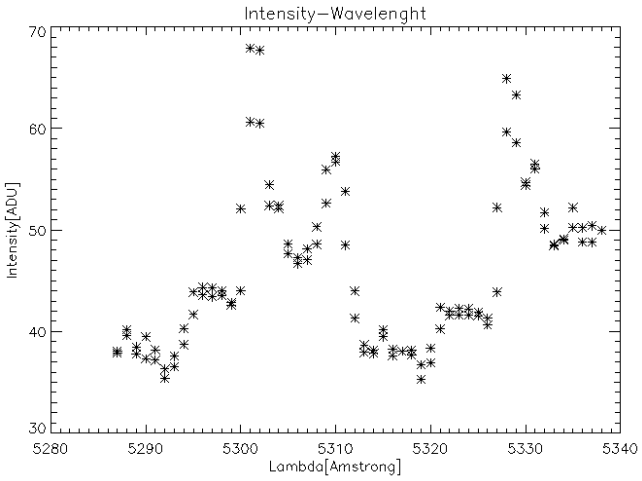

Figure 4.25: LCTF calibration scan with monocromator centred at 5284 Å with a resulting peak of intensity around 5303.16 Å.

Objective lens [O]	Focal length[mm]: 800	
	Diameter [mm]: 60	
	F/#: 13.3	
Collimator triplet [CoT]	Focal length [mm]: 100	
	Diameter [mm]: 50	
	Glasses: N-LAF21/SF10/N-LAK8	
	Achromatic designed by Optec	
Liquid Crystal Tunable Filter [LCTF]	**LCTF General**	Length [mm]: 90 Diameter [mm]: 60 Aperture [mm]: 20 Number of stages: 4 FSR [nm]: 2.7 FWHM [nm]: 0.15 Center wavelength [nm]: 528.64 – 533.38 Tuning step [nm]: 0.01
	Pre-filter	Manufacturer: Andover Corp. Center wavelength [nm]: 530.69 FWHM [nm]: 1.89
	LCPR	Manufacturer: MLO Rotation angles [deg]: 0 - 180
Camera triplet [CaT]	Focal length [mm]: 100	
	Diameter [mm]: 50	
	Glasses: N-LAF21/SF10/N-LAK8	
	Achromatic designed by Optec	
Detector [D]	Type: CCD Camera FLI Proline 1001E	
	Sensor: Kodak KAF-1001E	
	Frame size [pixels]: 1024x1024	
	Pixel size [µm]: 24	
	A/D Conversion [bit]: 16	

Table 4.1: Instruments specifications [Capobianco et al., 2011].

Chapter 5

Observations

5.1 Introduction

This chapter provides an overview on the total solar eclipse of the 11/07/2011, the identification of frames acquired with the CorMag instrument, affected marginally or not by the presence of clouds that covered the sky for part of the event and explained the criteria by which this was done.

5.2 11/07/2010 Solar Eclipse

On Sunday, 2010 July 11, a total eclipse of the Sun was visible from within a narrow corridor that traverses Earth's southern Hemisphere.
A total solar eclipse occurs when the Moon's apparent diameter is larger than the Sun, blocking all direct sunlight, turning day into darkness. Totality occurs in a narrow path across the surface of the Earth, while a partial solar eclipse will be visible over a region thousands of kilometres wide (Figure 5.1).

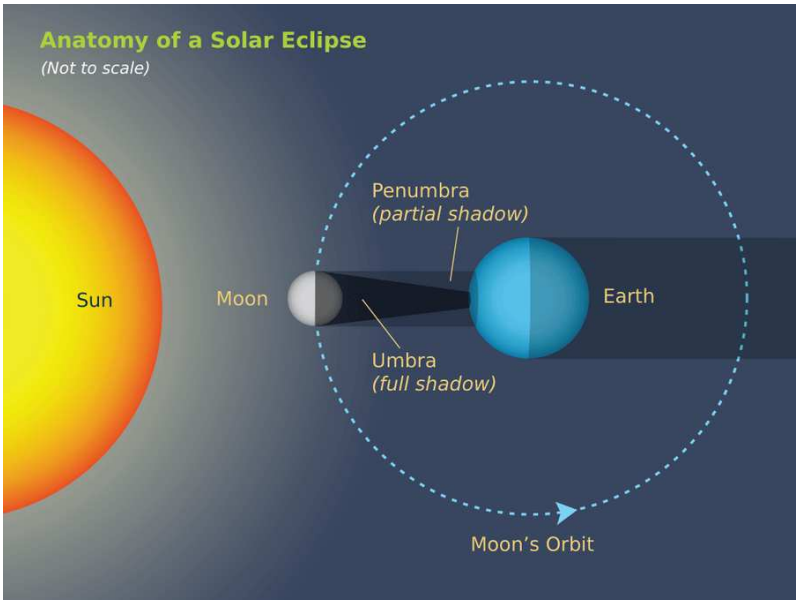

Figure 5.1: A schematic representation of a solar eclipse.

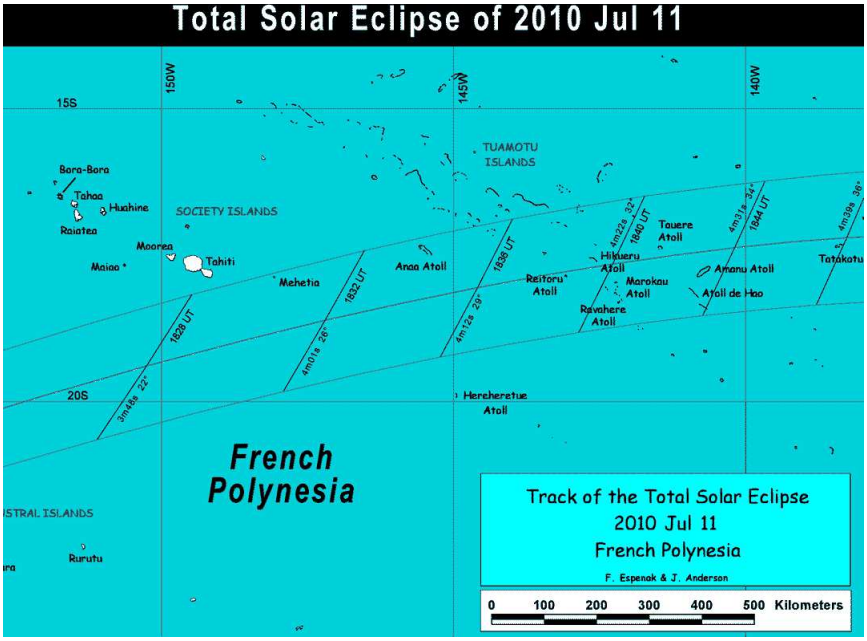

Figure 5.2: Solar eclipse path over French Polynesia.

The path of the Moon's umbral shadow crossed the South Pacific Ocean where it made no landfall except for Mangaia (Cook Islands) and Easter Island (Isla de Pascua). The path

of totality ended just after reaching southern Chile and Argentina. The Moon's penumbral shadow produced a partial eclipse visible from a much larger region covering the South Pacific and southern South America (Figures 5.2-5.3).

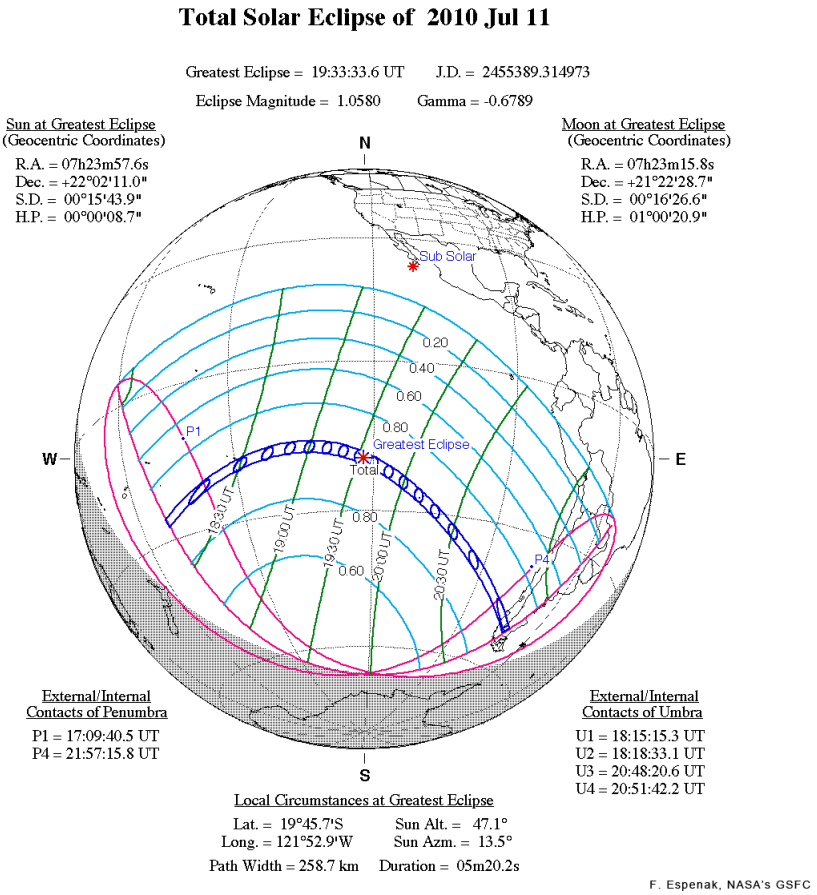

Figure 5.3: 11/07/2010 solar eclipse path [Espenak et al., 2008].

5.3 Evaluation of the cloudiness effects

Due to the transit of clouds during the occurrence of the solar eclipse (Figure 5.4) for data analysis were chosen only images in which the impact of the clouds was negligible.

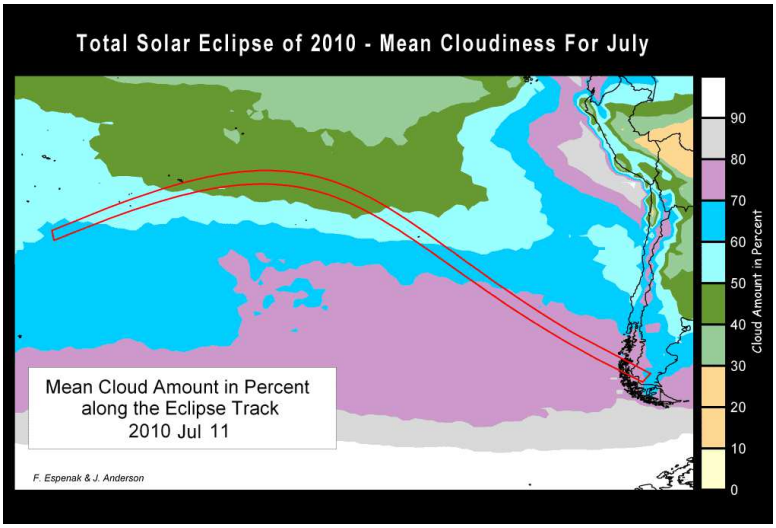

Figure 5.4: Clouds ammount over the eclipse path [Espenak et al., 2008].

A quantitative study seems to be very difficult, because the effects of the clouds are not the same. White clouds diffuse coronal light while dark ones reduce the its intensity. The exposure times of the CorMag are quite long (8 seconds) to present a combination of both these two effects. It is possible only a qualitative study, identifying the frames that appear to be little influenced by the effects of clouds. The situation is made even more difficult by the fact that the scattered light is polarized, then this has obvious effects on measures. About 50% of the measurements is "unwrapped "from this analysis (Figure 5.7). For each acquired image dark current is subtracted, saturated pixels are discarded and averaged over the whole frame (except for the saturated pixels) and then normalized per pixel and per second of exposure. Next to this value, is also calculated the average over a square (40x40 pixels) of the "black "disc of the moon (Figure 5.5).

These values are then expressed in function of the time at which the image was captured. Rejected images are those that have values of normalized intensity substantially greater or less than the average (Figure 5.6).

In particular, the criterion for images selection provides the following thresholds for normalized counts on the whole frame:

Max: 28000 ADU

Min: 9550 ADU

Furthermore, the variation of the average intensity with that on the Moon must be less than 37%.

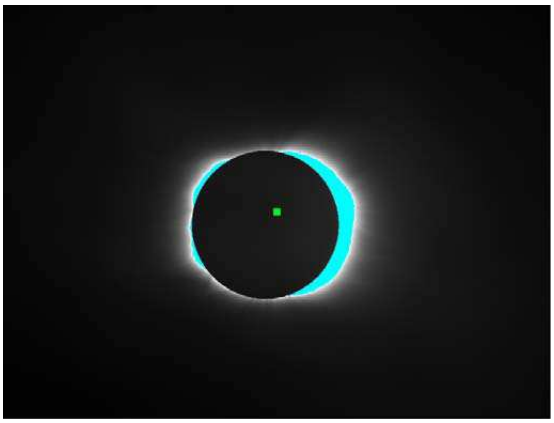

Figure 5.5: Example of the selected areas for the calculation of the averages (in the blue part the excluded ones from the calculation of the average over all the frame and in green the area used for the calculation of the average on the Moon) [Capobianco, 2011].

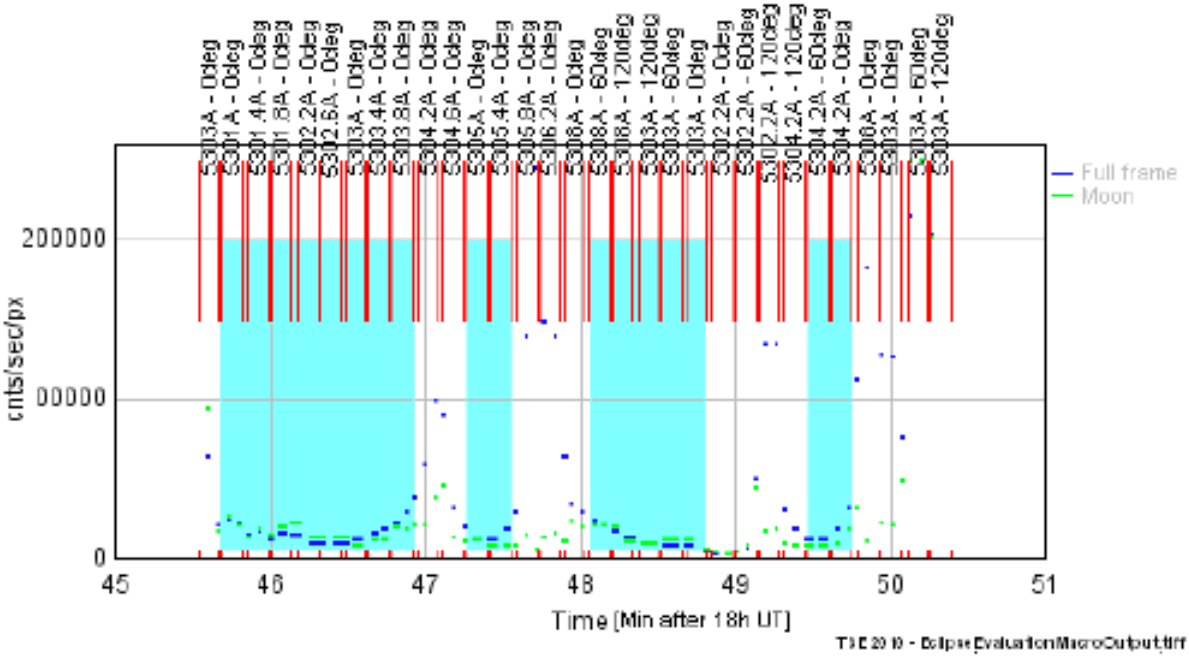

Figure 5.6: CorMag data selection. Only pictures that fall in the blue rectangle are selected [Capobianco, 2011].

Figure 5.7: Example of corrupted image for the presence of clouds [Capobianco, 2011].

5.4 Data selection

The data acquired with the CorMag instrument are digital images saved in fits format. The frame size is 1024x1024 pixels with a depth of 16 bit. Each file has a size of 2.051 KB (2 MB).

Among the 31 acquired eclipse images, after the identification of clouds corrupted frames, only two sets of three off-band and in-band images were selected for the polarimetric analysis(Figure 5.8 and 5.9).

They are respectively:

Off-band images (K corona):

Image	File Name	Wavelenght[Å]	Pol. Angle [deg]
Image 1	CorMagImage_2010.07.11.18.48.03.fits	5308	0°
Image 2	CorMagImage_2010.07.11.18.48.12.fits	5308	60°
Image 3	CorMagImage_2010.07.11.18.48.21.fits	5308	120°

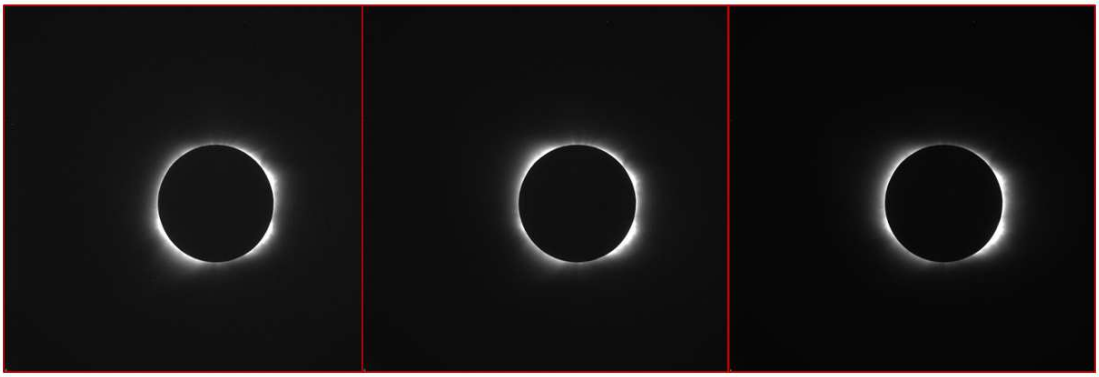

Figure 5.8: Out-band level 0 images at 0°, 60 °, 120 °[Fineschi et al., 2010a].

Total band images (E+K corona):

Image	File Name	Wavelenght[Å]	Pol. Angle [deg]
Image 1	CorMagImage_2010.07.11.18.46.38.fits	5303	0°
Image 2	CorMagImage_2010.07.11.18.49.09.fits	5302.2	60°
Image 3	CorMagImage_2010.07.11.18.48.40.fits	5303	120°

Figure 5.9: Total-band level 0 images at 0°, 60 °, 120°[Fineschi et al., 2010a].

The image at 5303 Åat 60°was not selected for data analysis because from an analysis of pixels counts emerged a greater presence of noise signals respect to the one at 5302.3 Å. The last one can be still considered within the in-band range because σ_{instr} is equal to 1.5 Å.

Chapter 6

Data reduction

6.1 introduction

Camera sensitivity, in terms of the minimum detectable signal, is determined by both the photon statistical (shot) noise and electronic noise arising in the CCD. Once accumulated in collection wells, charge arising from noise sources cannot be distinguished from photon-derived signal. Most of the system noise results from readout amplifier noise and thermal electron generation in the silicon of the detector chip. The approach to ensure the best possible SNR ratio is to a) develop a sensor with the highest possible quantum efficiency and b) reduce the various sources of noise to a minimum. Quantum Efficiency (QE) is related to the ability of the sensor to respond to the incoming photon signal and the conversion of it to a measurable electron signal. Clearly greater is the number of photoelectrons produced for a given photon signal higher is the QE. This parameter represents the effectiveness of a CCD imager in generating charge from incident photons, and is therefore a major determinant of the minimum detectable signal for a camera system, particularly when performing low-light-level imaging. No charge is generated if a photon never reaches the semiconductor depletion layer or if it passes completely through without transfer of significant energy. The nature of interaction between a photon and the detector depends upon the photon's energy and corresponding wavelength, and is directly related to the detector's spectral sensitivity range. To reduce camera noise signals in level 0 images was followed this procedure:

1. Dark removal

2. Flat field correction

3. Bias removal

4. Moon centring

At the end of the reduction process level 0 images have been transformed in level 1 ones, ready for data analysis. All operations on eclipse images were made using the IDL (Interactive Data Language) SolarSoft.
SolarSoft is a set of integrated software libraries, data bases, and system utilities which provide a common programming and data analysis environment for Solar Physics. The SolarSoftWare (SSW [SolarSoft web page http://www.lmsal.com/solarsoft/]) system is built from Yohkoh, SOHO, SDAC and Astronomy libraries and draws upon contributions from many members of those projects. It is primarily an IDL based system, although some instrument teams integrate executables written in other languages.

6.2 Dark removal

Dark current arises from thermal energy stored within the silicon lattice comprising the CCD. Electrons produced are captured by the CCD's potential wells and counted as signal. Additionally, this increase in signal also has a statistical fluctuation known as dark current noise. To reduce the effect of dark current CCDs can be cooled either with thermoelectric coolers (TECs) or liquid nitrogen .
The dark current in CCDs is usually very stable and it increase with the exposure time. For eclipse data, dark frame were acquired for each image and then subtracted to the correspondent one.

6.3 Flat field correction

Telescopes usually do not illuminate the detector homogeneously. Dust on optical surfaces leads to further shadowing of detector areas. The quantum efficiency of the CCD itself is not necessarily the same for all pixels. All these effects are improved by correcting for the flat image (Figure 6.1), which is an exposure of a homogeneously illuminated area. This can be a flat square or an evenly illuminated screen on the wall (domeflats), or just the

sky in zenith some minutes after sunset (skyflat, or twilight flat).
The data for the flat field calibration were acquired mounting the opal 5B, with a neutral density of $7.7 \cdot 10^{-7} B/B_{\odot}$ in front of the telescope. An example of radiometric frame is the follow: This flat field correction can be applied to each eclipse image taking the

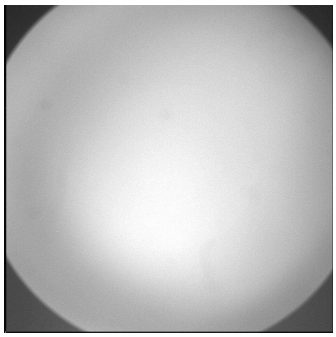

Figure 6.1: Example of flat field image, obtained with a 5B opal ([Fineschi et al., 2010a]).

maximum value of the flat field image, normalazing the flat image for this value and at the end subtracting this image from the eclipse one.

6.4 Bias removal

A bias exposure is an image acquired with the shutter closed and the shortest possible exposure time. The bias shows the electronic noise of the camera and its possible systematics. It's possible to remove its contribution from a frame considering the average counts of one of its own not exposed pixels column.

6.5 Moon centring

For centring eclipse images, was used as reference the centre of the Moon disk.
Plotting the mean intensity of the rows (columns) of every image its possible to obtain from the average of the positions of the two peaks the ordinate (abscissa) of the lunar disk photo-centre (Figure 6.2). This way images can be centred with respect to the centre of the lunar disk.
This moon centring procedure is sufficient for the data analysis because comparing the obtained Moon centre coordinates with the Sun centre one deduced from the 5-parameters fit discussed by [Balboni, 2009] (page 72-74) are not very different ($\pm$ 2 px).

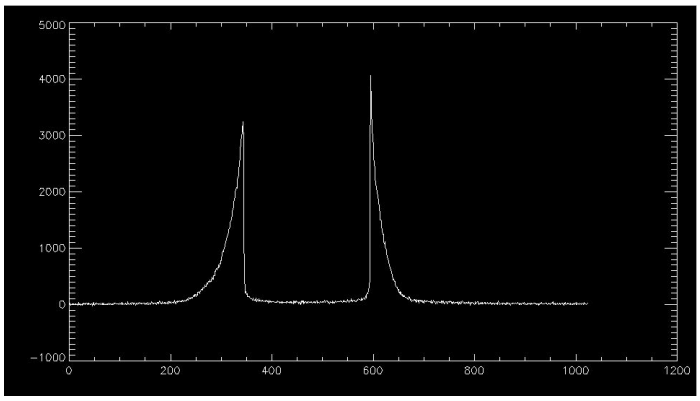

Figure 6.2: Example of mean intensity of columns.

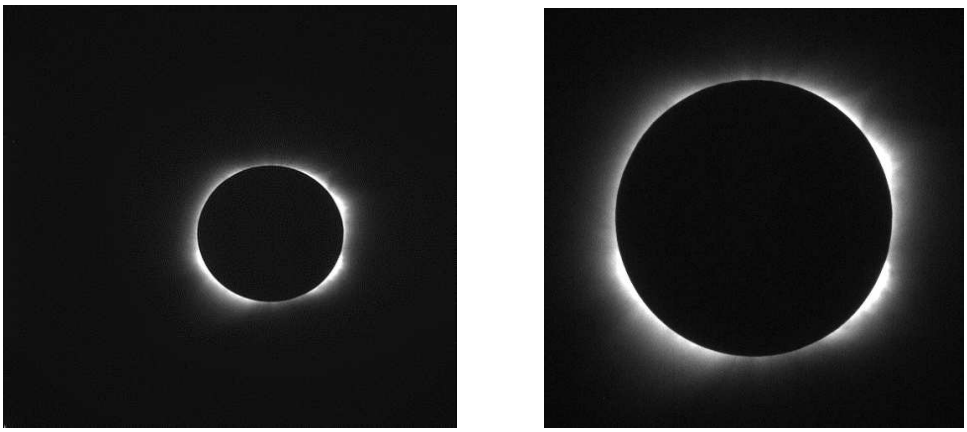

Figure 6.3: Comparison between level 0 (left) and level 1 (right) image.

Chapter 7

Data analysis

7.1 Introduction

The linear polarization of the FeXIV forbidden emission interpreted in terms of "saturated"Hanle effect, like said in chapter 3.2.3, can be used as a diagnostics tool of the coronal magnetic field.

By scattering, the polarization vector of the K-corona continuum emission is insensitive to the magnetic field and it is tangent to the solar limb. This property of the Thompson-scattered emission was used to calibrate out all the instrumental and environmental background from polarized acquired images. The linear polarization vector of the E-corona emission-line is instead directed radially. As predicted by the Hanle effect theory, variations from radial direction of the linear polarization vector are due to the presence of the magnetic field.

The most direct diagnostic of the coronal magnetic field, that is currently used, is the measurement of polarization in the forbidden spectral emission lines in the wavelength range of visible-light [Judge et al., 2007].

The linear polarization gives informations on the direction of the field as projected on the plane of the sky through the "saturated Hanle effect ". The circular polarization of the forbidden emission lines is sensitive to the field strength trough the Zeeman effect. Starting from level 1 K and (E+K) coronal images it's possible to obtain, using Eq. 4.5, the correspondent Stokes parameters in an ideal reference system in which the analyser is parallel to the vertical axes (Figure 7.1).

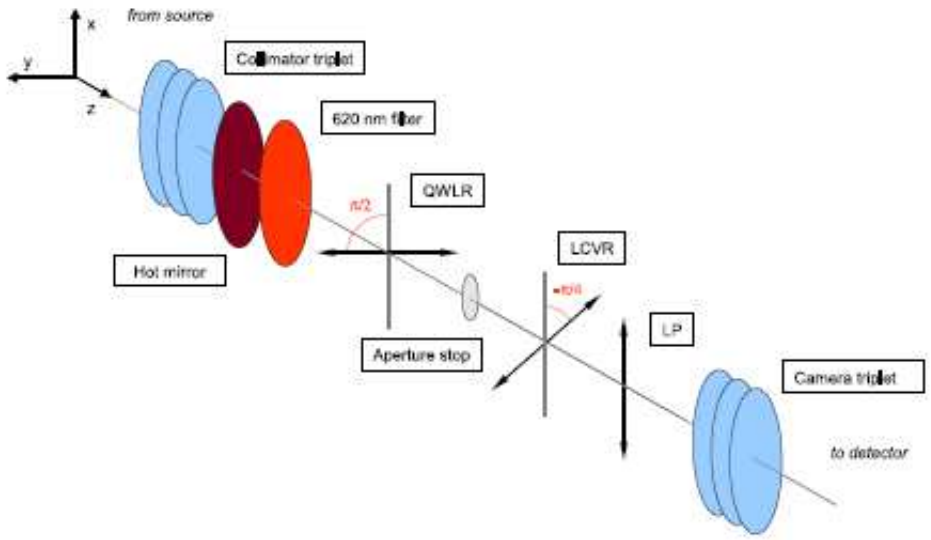

Figure 7.1: Optic scheme with the analyzer parallel to x-axis [Balboni, 2009].

Considering our three LCVR dalays (0°, 120°, 240°) Eq. 4.5 can by written as:

$$\begin{bmatrix} m_0 \\ m_1 \\ m_2 \end{bmatrix} = \frac{1}{2} \begin{bmatrix} 1 & 1 & 0 \\ 1 & -1/2 & \sqrt{3}/2 \\ 1 & -1/2 & -\sqrt{3}/2 \end{bmatrix} \begin{bmatrix} I \\ Q \\ U \end{bmatrix} \tag{7.1}$$

This way, inverting the modulation matrix, we have :

$$\begin{bmatrix} I \\ Q \\ U \end{bmatrix} = 2 \begin{bmatrix} 1/3 & 1/3 & 1/3 \\ 2/3 & -1/3 & -1/3 \\ 0 & 1/\sqrt{3} & -1/\sqrt{3} \end{bmatrix} \begin{bmatrix} m_0 \\ m_1 \\ m_2 \end{bmatrix} \tag{7.2}$$

From which Stokes parameters are given by:

$$I = 2(m_0 + m_1 + m_2)/3 \tag{7.3}$$

$$Q = 2(2m_0 - m_1 - m_2) \tag{7.4}$$

$$U = -\frac{2}{\sqrt{3}}(m_2 - m_1) \tag{7.5}$$

7.2 K Corona Stokes parameters

Applying equations 7.3-7.4 to each pixel of K-Corona (off-band) level 1 image, it's possible to determinate its Stokes parameters *I, U, Q* profiles. From U and Q, the polarization angle β is given by equation 3.12 and the polarized brightness pB (where pB $\equiv$ pI) is given by Eq. 3.11. Starting from the physical guide thesis that polarization in K corona is directed tangentially to the solar limb, the observation of the U and Q parameters modulation highlighted a swing below zero and not around it, as expected by the physics of the Thompson scattering (Figure 7.2) . This condition was probably due to a certain off-set, variable with the radial distance from the solar limb, attributable to a background not removed present in one of the three images.

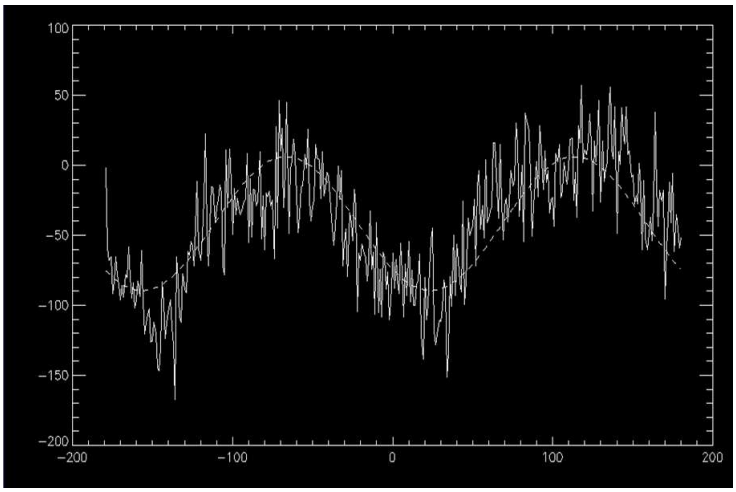

Figure 7.2: Modulation of the Stokes parameter U at a fixed radial diatance (1.2 $R_\odot$).

After a check of K corona images pixels counts this offset was attached to the m_3 image at δ=120°.

From the analysis of this offset, at different radial distances,from 1 to 1.5 $R_\odot$, was then created a synthetic image (Figure 7.3), called m_{offset}, in order to subtract this one from m_3.

Applying Eq. 6.21-6.23 to m_1, m_2 and to m_3' ($m_3' = m_3 - m_{offset}$) was found a new set of Stokes parameters.

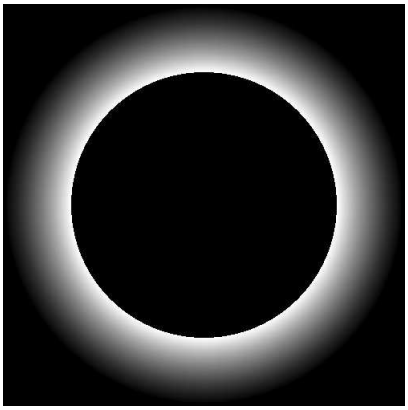

Figure 7.3: Offset synthetic image in logarithmic (log) scale.

To follow their images obtained with the application of the NRGF filter (Figures 7.6-7.7). *The normalizing radial-graded filter* (NRGF) is a simple and accurate method to look at the large-scale structure of the corona. It calculates the average and standard deviation of brightness as a function of height within an image and uses these values to normalize the brightness at each height. The view of coronal structures in a NRGF-processed image is equivalent to comparing a large set of normalized latitudinal profiles simultaneously [Habbal et al., 2011]; [Morgan et al., 2006a] and [Morgan et al., 2006b].
The reference system of the acquired frame is the following (Figure 7.4):

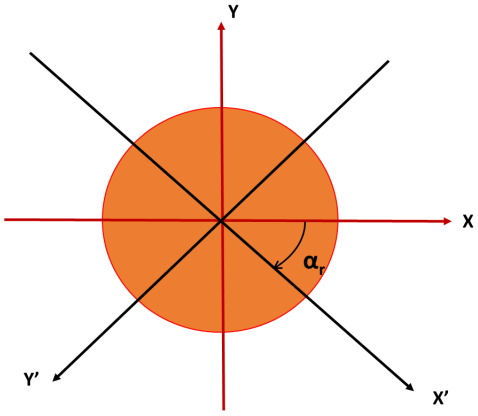

Figure 7.4: Frame coordinate system (Red) and analyzer reference system (Black). The second one is rotated of α_r= 43°with respect to the first.

The angular rotation α_r of the X' axis, that is parallel to the analyser, with respect

to X axis was verified with the 5-parameters fit of [Balboni, 2009] (page 72-74) and [Elmore et al., 2000] Eq. 10. In the fit the Sun centre coordinates were kept fixed, leaving free the delay angle δ. All Stokes parameters images in this chapter are represented with respect to the X'-Y' axis. At the end of the data analysis all images were rotated vertically, respect to the X axis, to take into account their reversal by the optics of the instrument (Figure 7.5).

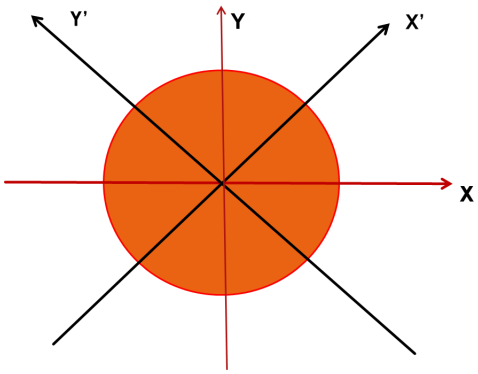

Figure 7.5: Frame coordinate system (Red) and analyzer reference system (Black) rotated vertically around the X axes.

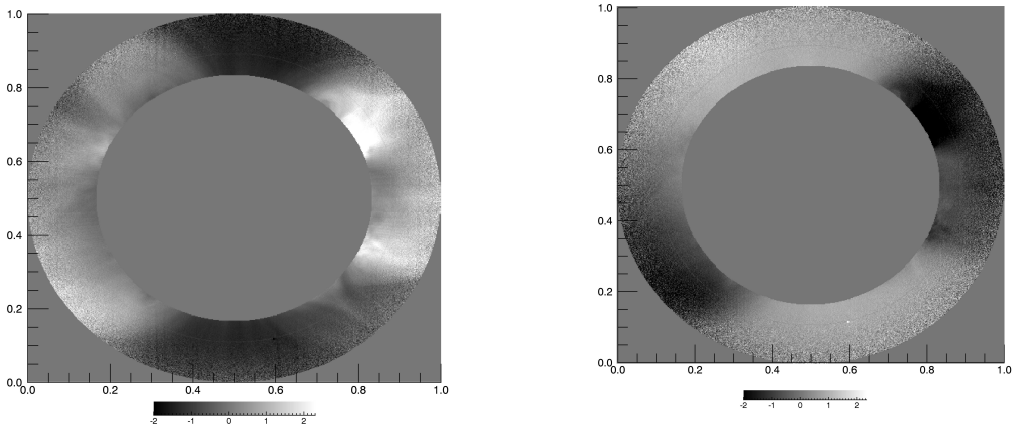

Figure 7.6: Image of K-corona Stokes parameter I (left) and Q (right), with the application of the NRGF filter (colours bar units are arbitrary).

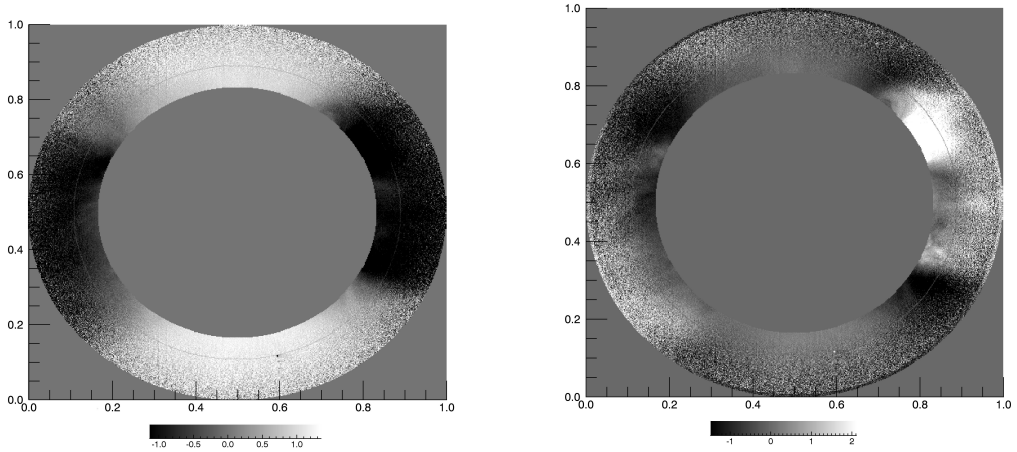

Figure 7.7: Image of K-corona Stokes parameter U (left) and pB (right), with the application of the NRGF filter (colours bar units are arbitrary).

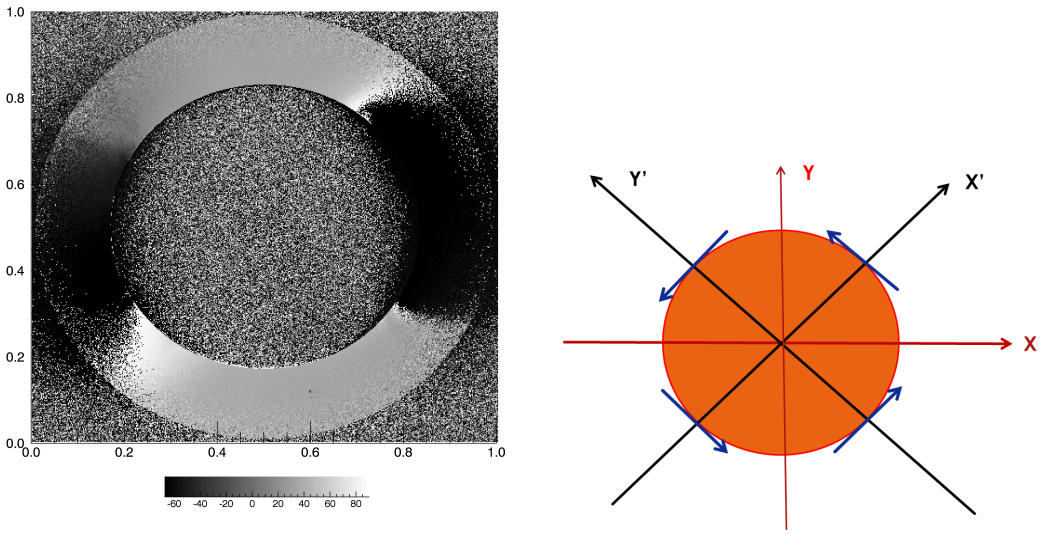

Figure 7.8: Image of K-corona polarization angle β (left), in degree, with the application of the NRGF filter (colours bar unit are arbitrary) and a diagram with the orientation of the polarization vector (blue arrows) in K corona (right). β is the angle between direction of the polarization vector and the direction of the analyser (X').

Obtained CorMag K corona total intensity image it's interesting to compare the coronal structures that are visible in, with the ones present in the high resolution white light image of the K corona (for the same eclipse), processed with the *Adaptive Circular High-pass*

Filter (ACHF)[1], developed by Druckmüller [Druckmuller et al., 2006] in order to highlight their differences and similarities (7.9).

CorMag instrument spatial resolution is lower ($\backsimeq$ 12.4 arcsec/px) than the Druckmuller ones ($\backsimeq$ 1 arcsec/px).

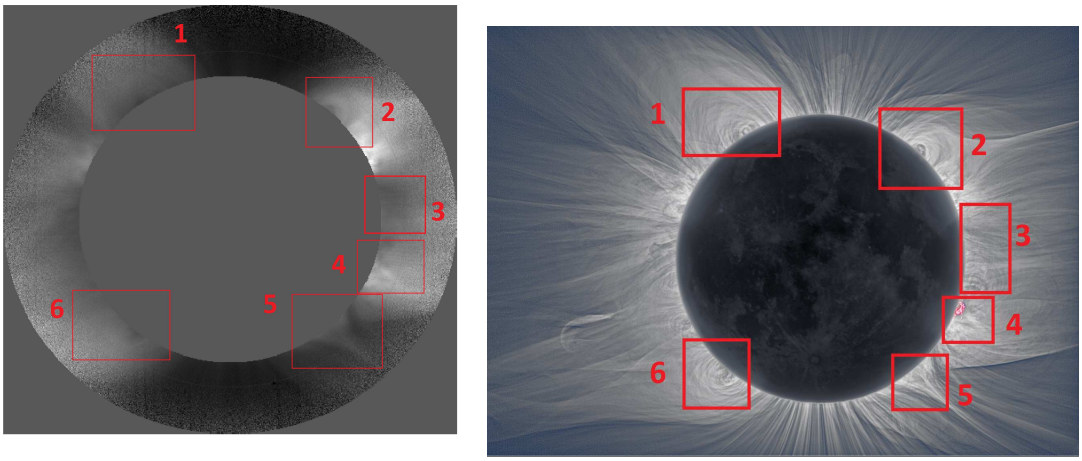

Figure 7.9: Comparison between structures present in the K corona image obtained by the CorMag instrument(left) and the high resolution one (right) by M. Druckmuller [Habbal et al., 2011].

[1] The Adaptive Circular High-pass Filter enhance the high spatial frequencies and to attenuate the low spatial frequencies in such a way that the resulting image is very close to what the human eye sees.

From the comparison of these two images it's possible to notice a good correspondence between the various structures.
In order to verify the tangentiality to the solar limb of the angle of linear polarization β (Eq. 3.11), it was plotted, at a certain radial distance from the limb, as a function of the polar angle α rotated of 43°(α_r), in order to refer to the reference system of the analyser (X-Y') (Figure 7.10).

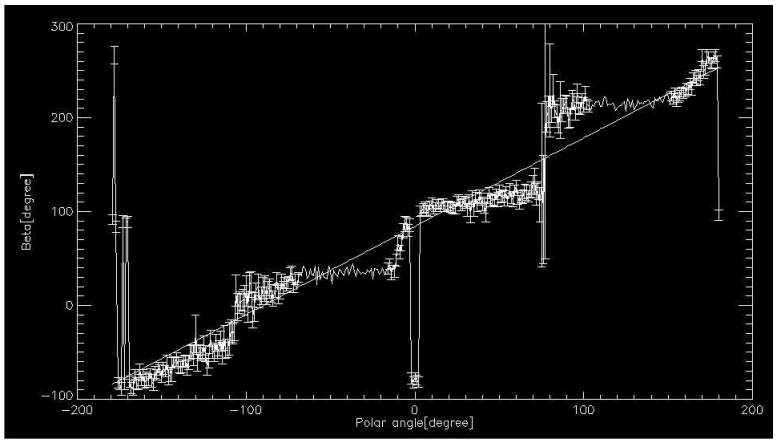

Figure 7.10: Plot of β as a function of the polar angle α,in the reference system of the analyser (X-Y'), both measured in degree at 1.2 $R_\odot$. For the determination of the error bars see par. 7.2.1.

From this plot (Figure 7.10) it is possible to observe the presence of a predominant tangentiality with a residual modulation. This last one can be removed from figure 7.10 (Figure 7.13), creating a synthetic image (Figure 7.12) from a sinusoidal fit of β -α_r-90°at different radial distances from 1 to 1.5 $R_\odot$(Figure 7.11), where α_r is the polar angle α rotated of 43°(analyser direction) and where 90°have been subtracted in order to match the zero value of both polarization and polar angle in their reference systems.

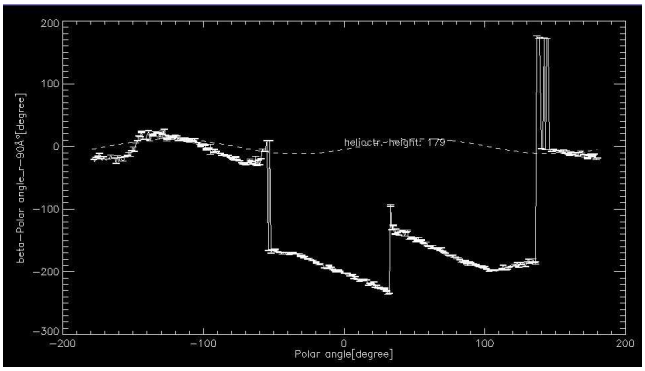

Figure 7.11: Plot of β -α_r -90°as a function of the polar angle α at 1.1 $R_\odot$,in the reference system of the analyser (X-Y'), with over-plotted errors bars and the fit function. For the determination of the error bars see par. 7.2.1.

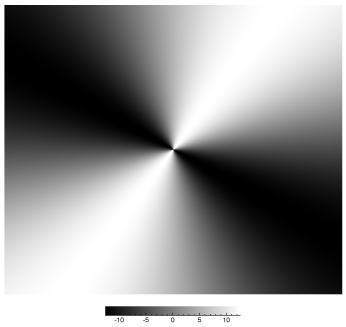

Figure 7.12: Synthetic modulation image.

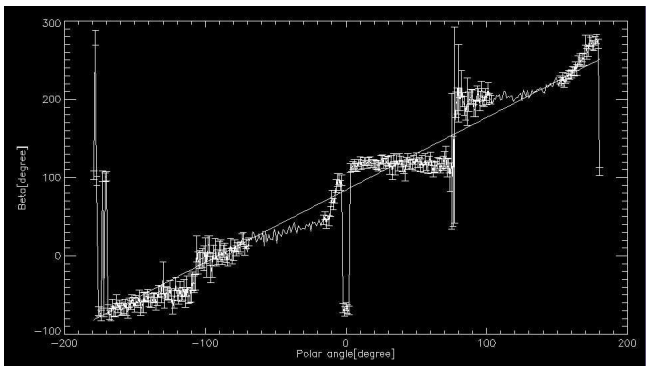

Figure 7.13: Plot of β as a function of the polar angle in the reference system of the analyser (X-Y'), both measured in degree, with residual modulation removed. For the determination of the error bars see par. 7.2.1.

7.2.1 Determination of the polarization angle β error.

The polarization angle β is given by Eq. 3.11, so from the error propagation of this equation the error on β is obtained it the following way:

$$\sigma_\beta^2 = (\frac{\partial\beta}{\partial U})^2\sigma_U^2 + (\frac{\partial\beta}{\partial Q})^2\sigma_Q^2 \tag{7.6}$$

defined a=$\frac{U}{Q}$ and $b = \frac{a}{1+a^2}$

$$\sigma_\beta = \sqrt{\frac{b^2}{4}(\frac{\sigma_U}{U})^2 + (\frac{\sigma_Q}{Q})^2} \tag{7.7}$$

from the errors propagation of Eq. 7.4 and 7.5 :

$$\sigma_U \propto \sqrt{\sigma_{m2}^2 + \sigma_{m3}^2} \tag{7.8}$$

$$\sigma_Q \propto \sqrt{\sigma_{m1}^2 + \sigma_{m2}^2 + \sigma_{m3}^2} \tag{7.9}$$

where

$$\sigma_{m1} = \sqrt{K_{ADC}S_1}$$
$$\sigma_{m2} = \sqrt{K_{ADC}S_2}$$
$$\sigma_{m3} = \sqrt{K_{ADC}S_3}$$

K_{ADC} is the gain of the camera (Chap. 4.4) and S is the image number of counts for each pixel. In polar regions there are not error bars because there the *signal to noise ratio* (SNR),the ratio of signal power to the noise power corrupting the signal, is too low to be considered.

7.3 (E+K) Corona Stokes parameters

In-band measures are still influenced by the presence of K corona, so it is necessary to remove these contributes. The procedure for the determination of (E+K) corona Stokes parameters is the same used for K corona. Stokes profiles obtained from the application of Eq. 7.21-7.23 to in-band level 1 images (Figures from 7.14 to **??**), rotated vertically around the X axes (Figure7.5)), are the following:

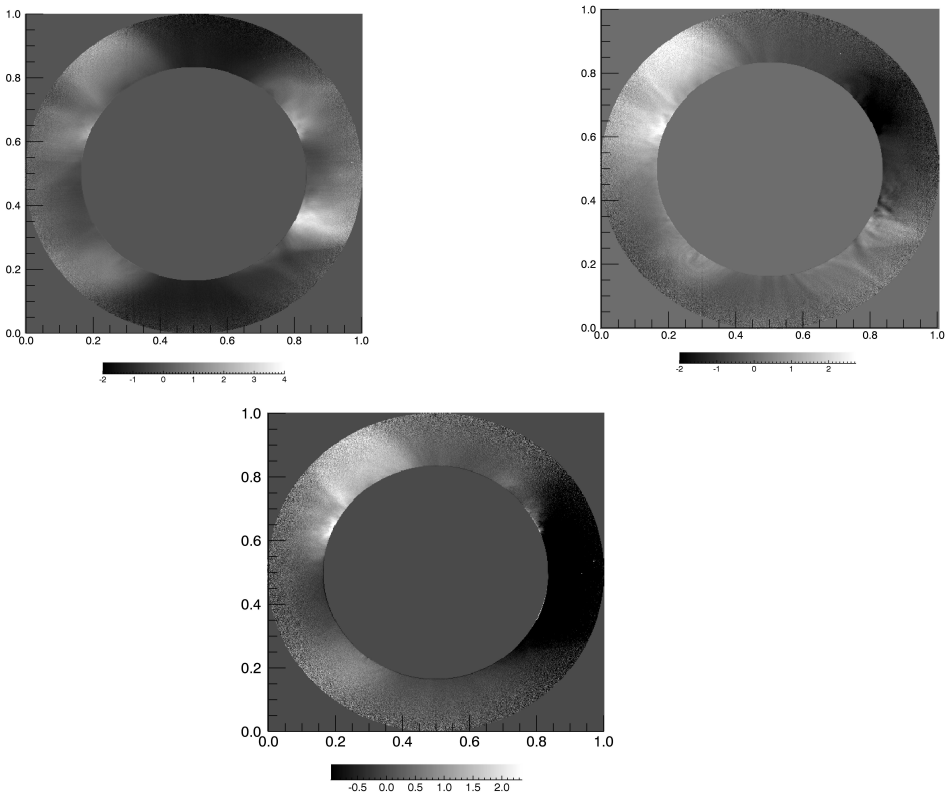

Figure 7.14: Image of (E+K) corona Stokes parameter I (left) and Q (right) and $\mathbf{U}$ (bottom) with the application of the NRGF filter (colours bar units are arbitrary).

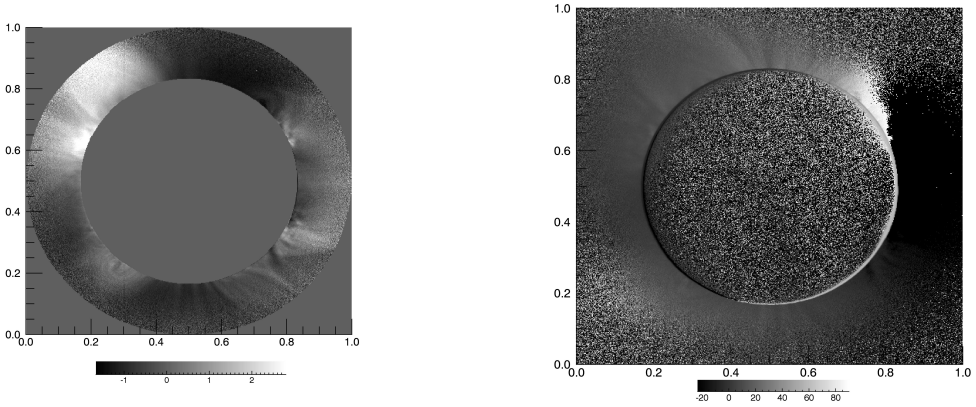

Figure 7.15: Image of (E+K) corona Stokes parameter pB (left) with the application of the NRGF filter (colours bar units are arbitrary) and the polarization angle β in degree (right).

7.4 E Corona Stokes parameters

From (E+K) and K corona level 1 images it's possible to obtain E corona ones, just removing the contribute of K corona in the following way:

$$image1_{(E)} = image1_{(E+K)} - image1_{(K)} \tag{7.10}$$

$$image2_{(E)} = image2_{(E+K)} - image2_{(K)} \tag{7.11}$$

$$image3_{(E)} = image3_{(E+K)} - image3_{(K)} \tag{7.12}$$

In the case of $image2_{(E)}$, because it's used a (E+K) image centred at 5302.2 Å, it's necessary to take into account its shift from the nominal line wavelength in the following way:

$$image2(E) = (image2_{(E+K)} - image2_{(K)})/c \tag{7.13}$$

where c is a factor given by the ratio between the intensity of the line profile at 5303 and the one at the selected wavelength.
For a line profile of Gaussian shape, with intensity distribution [Mierla et al., 2008]

$$I(\lambda) = \frac{1}{2\sqrt{\pi}} e^{-\frac{(\Delta\lambda)^2}{2\sigma^2}} = I(\lambda_0) e^{-\frac{(\Delta\lambda)^2}{2\sigma^2}} \tag{7.14}$$

the standard deviation, σ, is related to the full with at half maximum, FWHM, through

$$\sigma = \frac{FWHM}{2\sqrt{2\ln 2}} \tag{7.15}$$

Considering the convolution of both instrumental and line σ (respectively FWHM≅1.5 Å[Fineschi et al., 2011] and FWHM ≅ 1 Å[Mierla et al., 2008])we have:

$$c = \frac{I(\lambda_0)}{I(\lambda)} \frac{1}{e^{-\frac{(\Delta\lambda)^2}{2(\sigma_{st}^2 + \sigma_{st}^2)}}} \tag{7.16}$$

Applying Eq. 7.3-7.5 to $image1_{(E)}$, $image2_{(E)}$ and $image3_{(E)}$ it's easy to obtain E corona Stokes parameters (Figures 7.16-7.18-7.19), with respect to the reference system of figure 7.5.
CorMag E corona total intensity image (Figure 7.16) can be compared with the correspondent high resolution one, processed with the ACHF, developed by Druckmüller [Druckmuller et al., 2006] to compare large and small scale[2] structures.

[2] About 1 arcmin ∼ 40M.

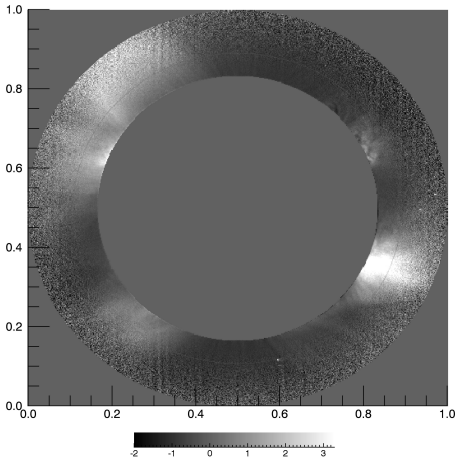

Figure 7.16: Image of E corona Stokes parameter I with the application of the NRGF filter (colours bar units are arbitrary).

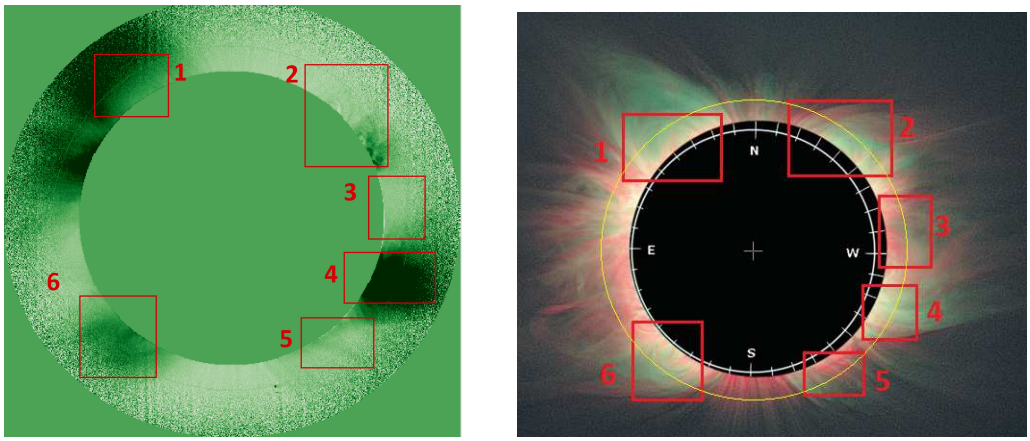

Figure 7.17: Comparison between structures present in the E corona I image, on the left, obtained by the CorMag instrument (spatial resolution $\backsimeq$ 12.4 arcsec/px) and on the right the high resolution one (spatial resolution $\backsimeq$ 1 arcsec/px) by M. Druckmuller (July 2010). Overlay of FeX (red) and FeXIV (green). The same amount of these colors is yellow.

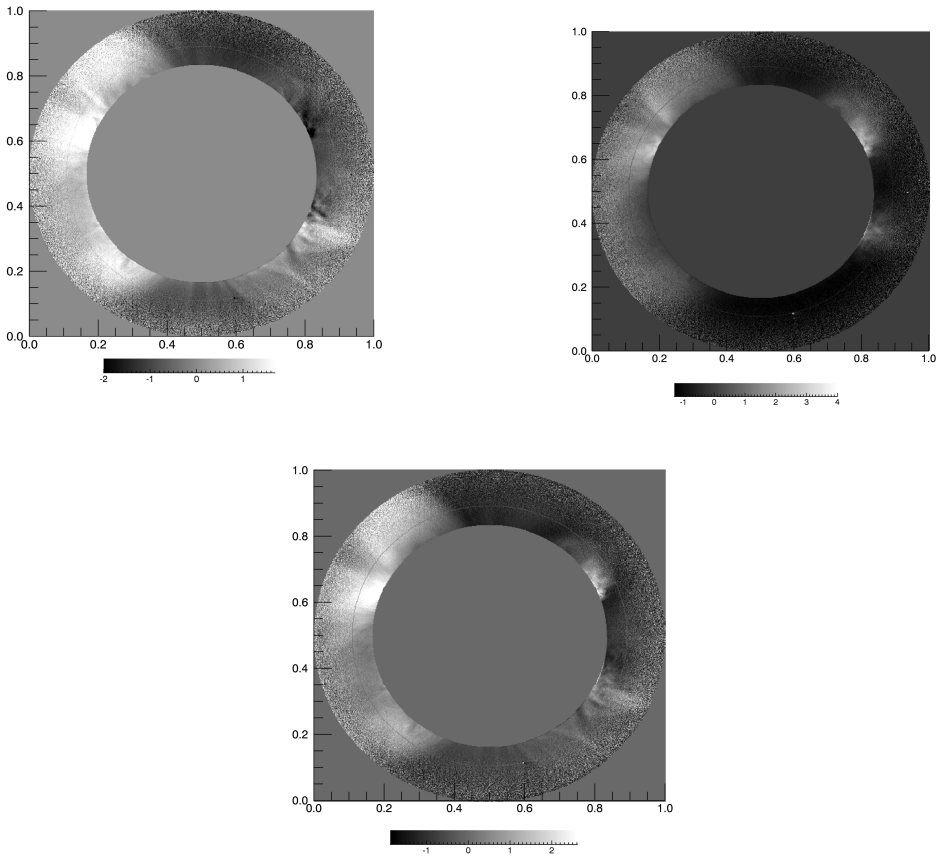

Figure 7.18: Image of E corona Stokes parameters Q (left), U (centre) and pB (right) with the application of the NRGF filter (colours bar units are arbitrary).

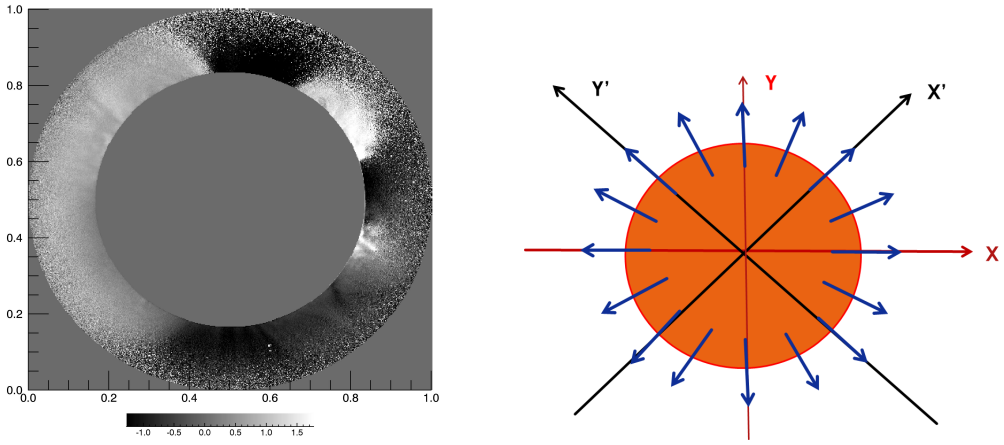

Figure 7.19: Image of E corona the polarization angle β in degree (left) and a digram (right) of the direction of the polarization vector in E corona (blue arrows). β is the angle between direction of the polarization vector and the direction of the analyser (X').

In the case of the *Emission* corona the physical thesis is that the polarization vector is directed radially. To verify graphically this statement and highlight areas with significant variations from radiality, it was made a plot of the E corona polarization angle β in function of the polar angle α, both in degree (Figures 7.20-7.21), where the dotted line is the polarization vector direction in the zero field case. The rotation of the polarization vector is induced by the Hanle effect (Par. 3.2.3).

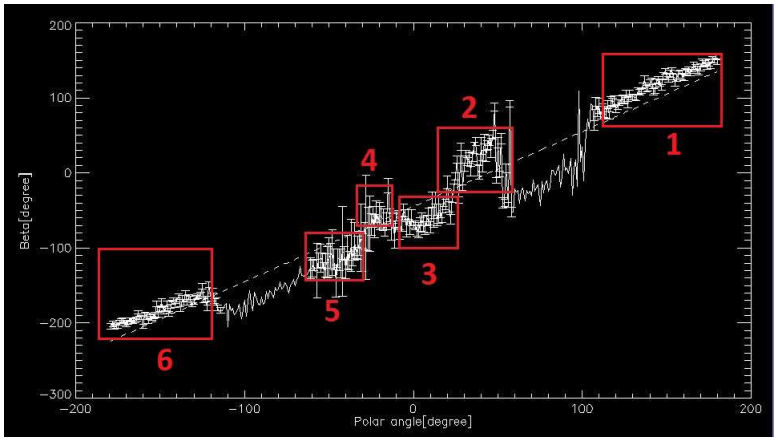

Figure 7.20: E corona polarization angle modulation at 1.2 $R_{\odot}$. Differences from radiality are due to the Hanle effect. Area numbered in red correspond to the different structures present in Figure 7.17. For the determination of the error bars see paraghraph 7.2.1.

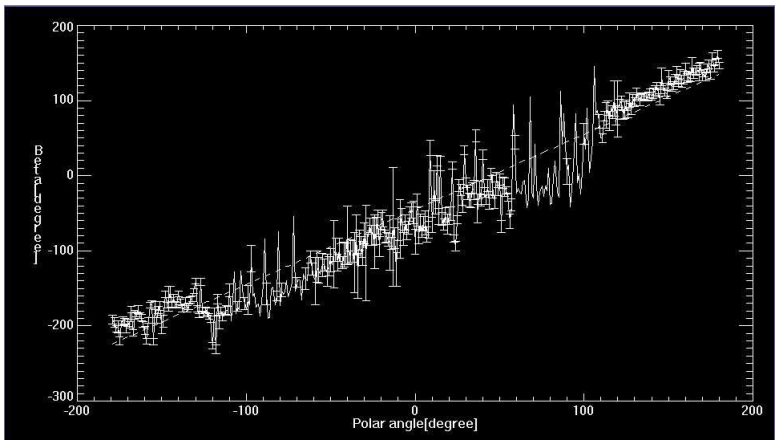

Figure 7.21: E corona polarization angle modulation at 1.3 $R_{\odot}$.

In the plot of figure 7.20 and figure 7.21 is evident a radial mood with five areas, numbered in red, in which is present a variation from radiality. This variation becomes less significant with the increase of radial distance for the decrease of the contribution due to the E corona (Figure 7.21). One way to emphasize visually this trend its to change the colour scale in the polarization angle image(Figure 7.22):

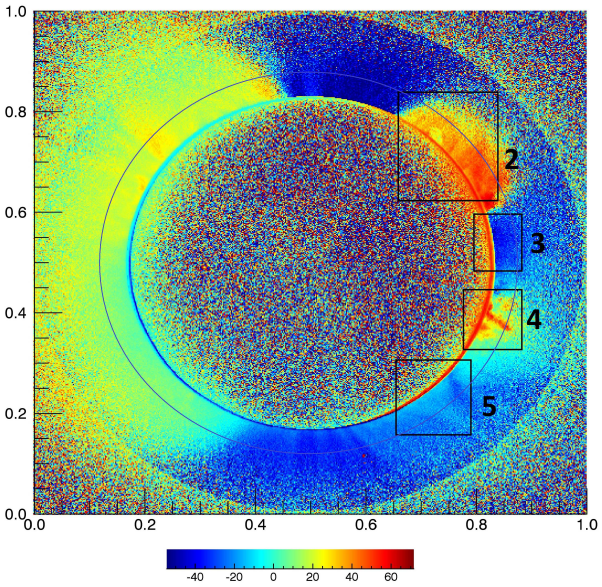

Figure 7.22: Image of E corona polarization angle β (in degree) in a blue-red colour table.

From figure 7.22 areas characterized by significant variation of the polarization angle are placed in correspondence of magnetic structure (regions 3 and 2 of figure 7.23)
In the region number 2 (corresponding to the north-west limb) of both figure 7.9and figure 7.17 is present a coronal structure called *cavity*. These structure is highlighted better in figures 7.24 and 7.26.
Cavities are elliptical regions of rarefied density commonly observed as part of a CME, but may also exist before eruption [Gibson et al., 2006]. Such quiescent cavities appear as dark, semi-circular or circular regions, often surrounding a central prominence (relatively

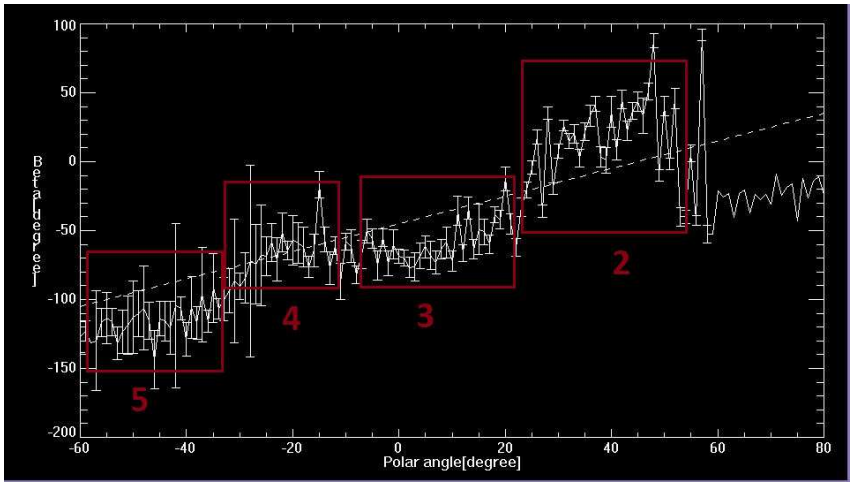

Figure 7.23: Focus on the regions with variation from radiality in E corona β modulation plot (Figure 7.20) at 1.2 $R_{\odot}$ that are also highlighted in figure 7.22.

cool and dense plasma suspended in the solar corona), and embedded in a helmet-shaped white-light streamer. They are ubiquitous: several may be visible on a given day; and can be long-lived (on the order of months): either reforming or only partly erupting in CMEs [Gibson et al., 2010];[Fan et al.,2006] . They provide clues to magneto hydrodynamic equilibrium states of the solar corona and to the processes which can destabilize these equilibria and drive coronal mass ejections.

One model for a cavity, both in the CME and as a precursor structure in conjunction with a quiescent prominence, is that of a magnetic flux rope of twisted field lines winding about an axial field line. However, the question of whether the flux rope is formed during the eruption, or whether the flux rope existed prior to the eruption, remains controversial.

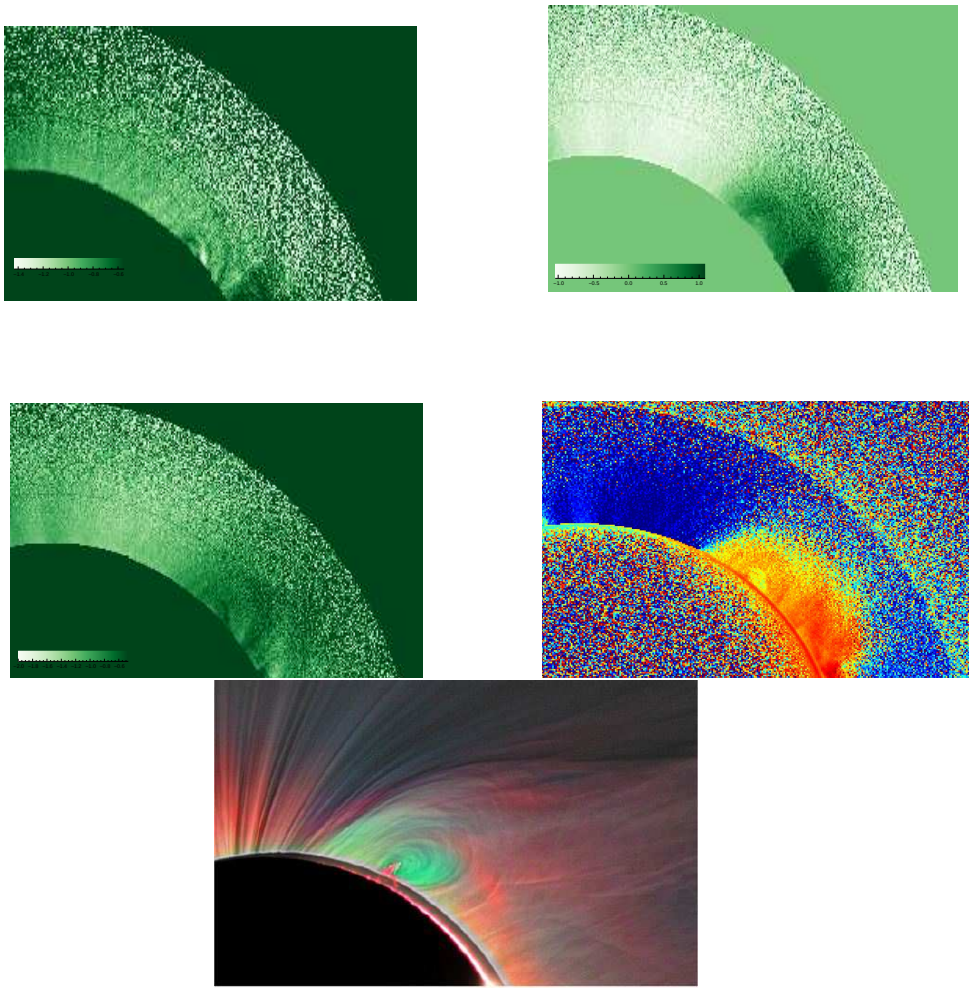

Figure 7.24: Focus on the observed (box 2 Fig.7.17) coronal cavity in FeXIV line: CorMag, from left to right I, U, Q (in the green scale, whith the application of the NRGF filter)(spatial resolution $\backsimeq$ 12.4 arcsec/px) and β (in the blue red scale)-High resulution by M. Druckmuller (right)(spatial resolution $\backsimeq$ 1 arcsec/px)(July 2010).

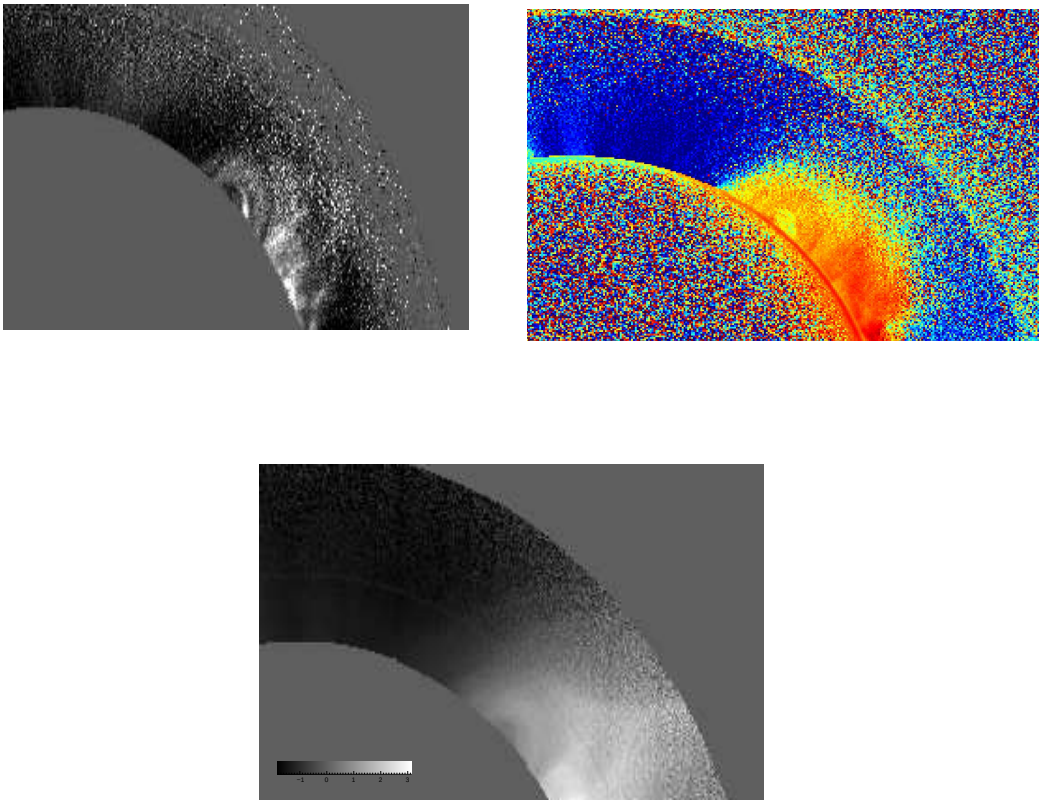

Figure 7.25: Focus on the observed coronal cavity (box 2 Fig.7.17): CorMag E (left) and K corona (bottom) p images(with the application of the NRGF filter)and E corona polarization angle β (right) image (spatial resolution $\backsimeq$ 12.4 arcsec/px). The polarization angle is represented in a blue-red colours scale.

Figure 7.26: Focus on the observed coronal K coronal cavity (box 2 Fig.7.9): CorMag image on the left(spatial resolution $\backsimeq$ 12.4 arcsec/px) and the high resulution by M. Druckmuller (July 2010) on the right (spatial resolution $\backsimeq$ 1 arcsec/px).

7.5 SDO/AIA EUV observations

The Atmospheric Imaging Assembly (AIA) for the Solar Dynamics Observatory (SDO) is designed to provide an unprecedented view of the solar corona, taking images that span at least 1.3 solar diameters in multiple wavelengths nearly simultaneously, at a resolution of about 1 arcsec and at a cadence of 10 seconds or better. The AIA will produce data required for quantitative studies of the evolving coronal magnetic field, and the plasma that it holds, both in quiescent phases and during flares and eruptions. The AIA science investigation aims to utilize these data in a comprehensive research program to provide new understanding of the observed processes and, ultimately, to guide development of advanced forecasting tools. The AIA instrument consists of four generalized Cassegrain telescopes that are optimized to observed narrow bandpasses in the EUV in order to observe solar emissions from the transition region and corona. The AIA design makes use of metal entrance filters at the aperture of each telescope and in a filter wheel located in front of each focal plane. The filters suppress unwanted UV, visible, and IR radiation for the EUV channels [Lemen et al., 2011].
To follow AIA observations of the day of the eclipse (Figure 7.28) with different filters, corrisponding to different temperatures (Figure 7.27):

Channel name	Primary ion(s)	Region of atmosphere*	Char. log(T)
white light	continuum	photosphere	3.7
1700Å	continuum	temperature minimum, photosphere	3.7
304Å[f]	He II	chromosphere, transition region	4.7
1600Å[f]	C IV+cont.	transition region + upper photosphere	5.0
171Å[f]	Fe IX	quiet corona, upper transition region	5.8
193Å[f]	Fe XII, XXIV	corona and hot flare plasma	6.1, 7.3
211Å[f]	Fe XIV	active-region corona	6.3
335Å[f]	Fe XVI	active-region corona	6.4
94Å[f]	Fe XVIII	flaring regions (partial readout possible)	6.8
131Å[f]	Fe VIII, XX, XXIII	flaring regions (partial readout possible)	5.6, 7.0, 7.2

Figure 7.27: AIA filters properties (∗ Absorption allows imaging of chromospheric material within the corona; f in baseline program) [Lemen et al., 2011].

Also in AIA observations is present the same coronal cavity, above the north-west limb, observed by the CorMag instrument(Figures 7.29- 7.30).

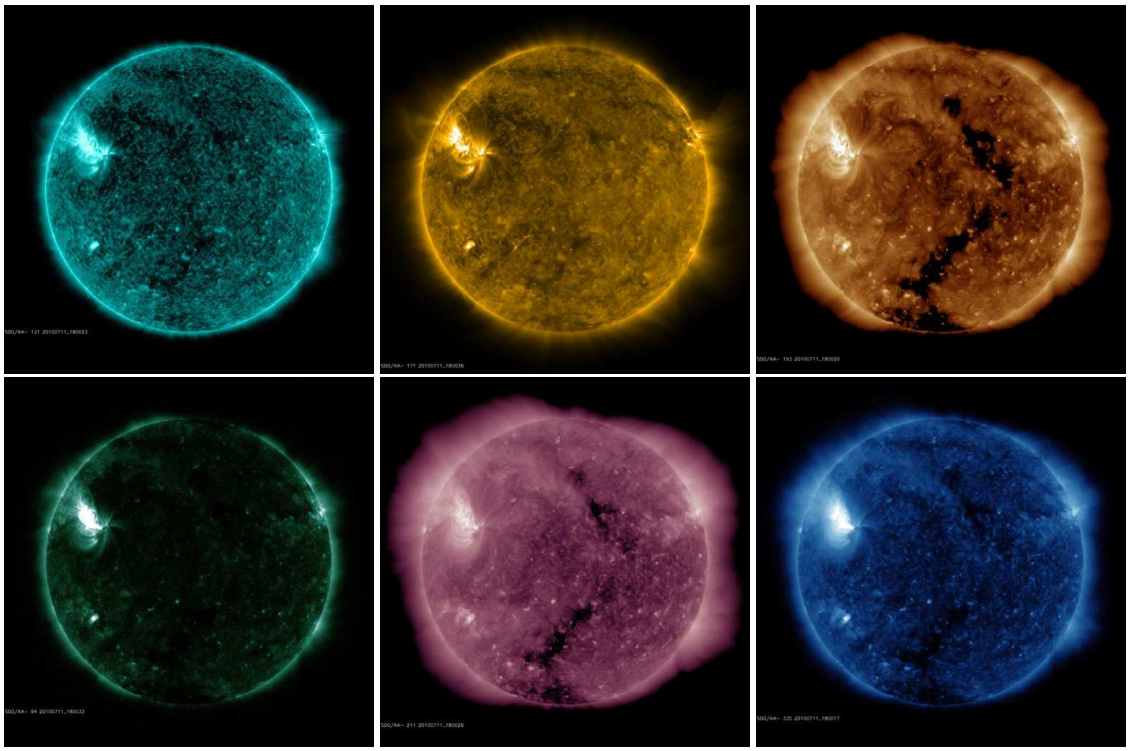

Figure 7.28: AIA EUV observation at the time and date of the eclipse with differt filters, respectly from left to right: 131, 171, 193, 94, 211, 335 (spatial resolution $\backsimeq$ 1.5 arcsec/px, [Lemen et al., 2011]). (Credits: NASA/SDO).

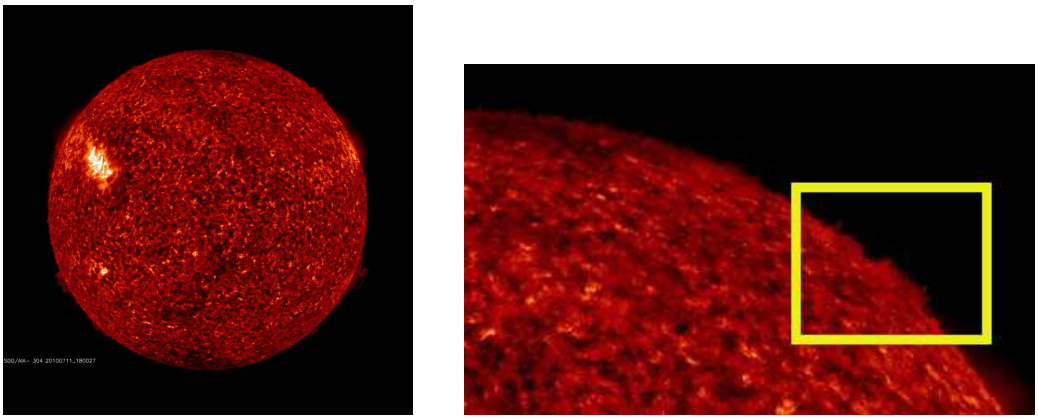

Figure 7.29: SDO/AIA observation of the day of the eclipse with the 304 filter (HeII) on the lefth. On the right a focus on the region above the north-west limb (box 2 Fig.7.17) were is highlighted the protuberance wich generates the coronal cavity Figure 7.25.

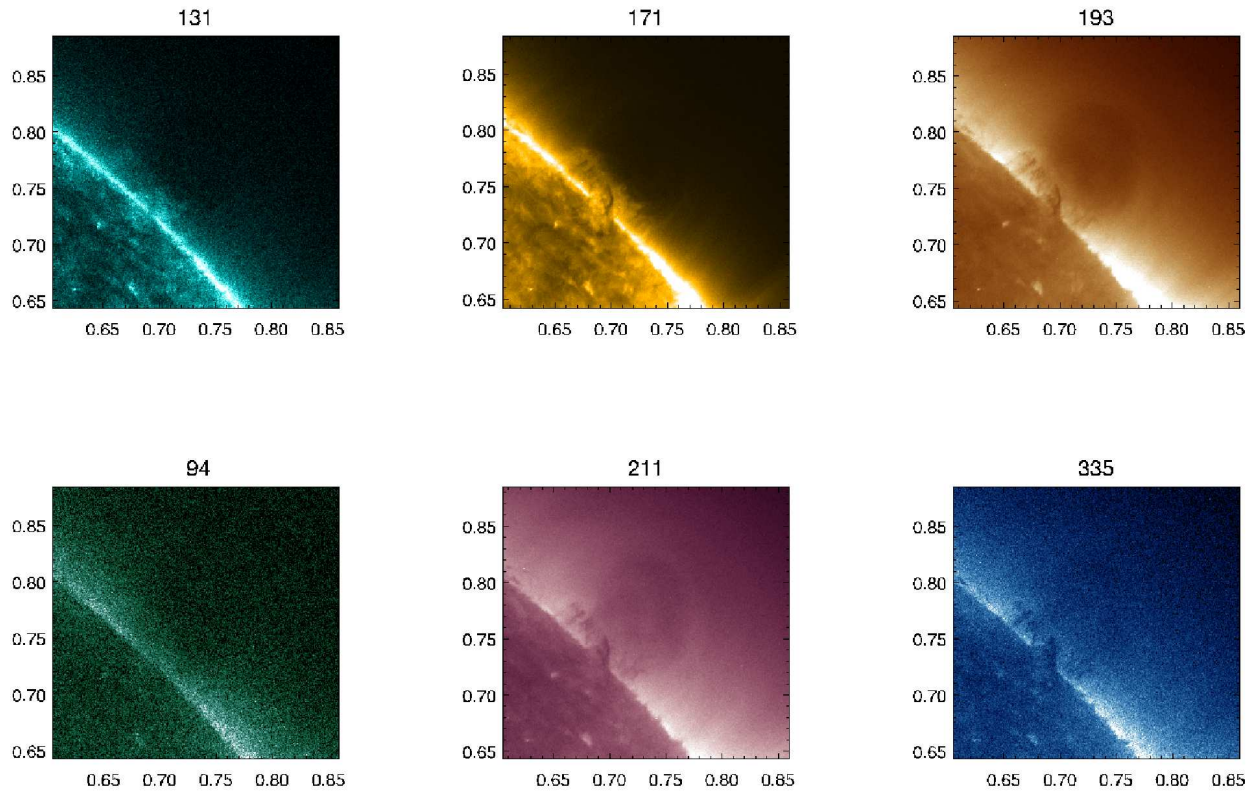

Figure 7.30: Coronal cavity (box 2 Fig.7.17) observed by SDO/AIA, with different filterS, the day of the eclipse, in the the region above the north-west limb [Bemporad,2014].

Chapter 8

Numerical simulations

The last decade has seen a considerable increase in the sophistication of models of the solar corona. Improved present models are able to use solar observations directly as boundary conditions on the calculations and can model the evolving solar corona. Despite these advances, some of the fundamental theoretical questions in solar physics still remain unsolved. Continued comparisons of model predictions and observations will led to answer these key questions and provide new insights into the physics of the solar corona.

8.1 Forward simulations

Coronal observables depend upon density, temperature, velocity and magnetic field, all of which are important constraints on theoretical models. Comparing models to data is not straightforward. Forward-modeling is the process of taking a model-defined three-dimensional distribution of coronal plasma properties and performing line of sight integrals specific to a given coronal observable's dependence on these properties. S. Gibson[1] and her team are working to construct modular Forward-model codes in IDL Solarsoft, to enable the community to compare model predictions and data. A suite of forward modeling software is now being tested by HAO and other community users. This "FORWARD tree"includes a set of magnetohydrodynamic models and is capable of reproducing a broad range of observables, from white light to EUV to CoMP Stokes parameters.
The FORWARD suite of SolarSoft IDL codes computs the expected E-line emission using an analytic model represented by a *data cube*. The Forward modelling can be compared

[1]High Altitude Observatory of the National Center for Atmospheric Research.

to observations. Observables such as extreme ultra violet, soft X-ray, white light, and polarization images can be simulated. The codes outputs the results in a variety of forms in order to easily create movies, Carrington maps, observable information at a particular point in the plane of the sky, etc. Simulations of solar corona structure are based on "force free "extrapolation of the photospheric magnetic field for the solution of the coronal MHD equations in the steady state considering the interaction of the solar wind with local plasma.

Turbulent Alfvén waves emanating from the chromosphere were suggested as a possible mechanism to both accelerate the solar wind and heat the plasma in the solar corona [Alazraki et al.,1971]. The source of such wave energy is assumed to be the constant reconfiguration of the magnetic field in the photosphere and chromosphere [Oran et al, 2013].

The basic procedure of Forward technique is to calculate the Stokes vector produced along a given Line of sight (LOS) in a magnetic and atmospheric model and build an image from a grid of sight lines. The magnetic field, temperature, density, and velocity for the model are given at every location along each LOS . Given this information, the level populations and the emitted polarization profiles for the selected transition are given at each location using the publicly available Fortran code (FORCOMP). FORCOMP first calculates the statistical-equilibrium equations based on the location and the local plasma parameters from the model: height above the solar surface [h], density [ρ], temperature [T], magnetic field [B], and velocity [v]. Using standard atomic data, the statistical-equilibrium equations determine the relevant level populations of the atomic system for the transition in question. Then FORCOMP solves the radiative-transfer equations to calculate the polarization of the reemitted radiation in the direction of the observer. Signals are then integrated over wavelength into a single number for each pixel (or LOS) and are assembled into an image [Rachmeler et al., 2013].

The benefit of using of FORWARD simulations is that it make easy to calculate the simulated polarization signals from a theoretical model of a magnetic system, compare the resulting images with observations and compare models themselves.

8.1.1 Results of Forward simulations

Through the IDL Solar Software, after installing the latest version of FORWARD codes (http://people.hao.ucar.edu/sgibson/FORWARD/TARS/), it's possible to run it from the

command line writing: "IDL>for_widget ". There are generally three widgets: TOP (upper left), MODEL (lower left), and OPTIONS (upper right). The model used for these coronal simulations is called "**NumCube**" because it use a data cube which contains informations about coronal plasma physical parameters (height above the solar surface [h], density [ρ], temperature [T], magnetic field [B], and velocity [v] , physical). After selecting the model and loading the data cube it's possible to set the exact data and time of the eclipse, to tune options about the fields of view, the line of sight,resolution, etc.. , setting the physical observable we are interested in and at the end starting the simulation. The output is a bi-dimensional matrix which contains the values of selected parameter so it's possible to represent it like a bi-dimensional image. To follow the obtained Forward output, for E and K corona (Figures from 8.1 to 8.6)

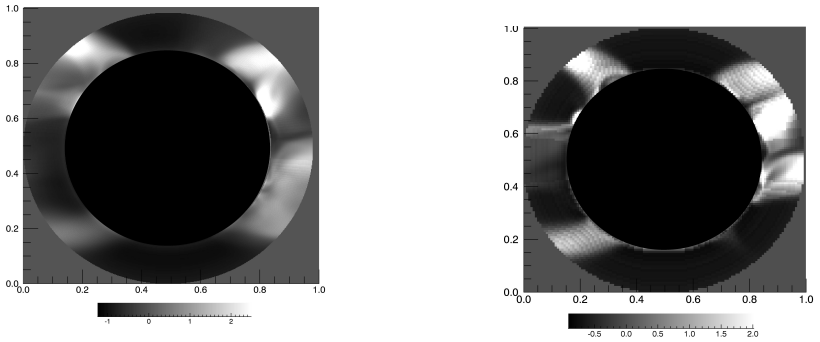

Figure 8.1: Comparison beetween E corona Stokes parameter I obtained by Forward simulation integrated along the LOS (left) and along the POS (right), both images with the application of the NRGF filter (colours bar units are arbitrary)

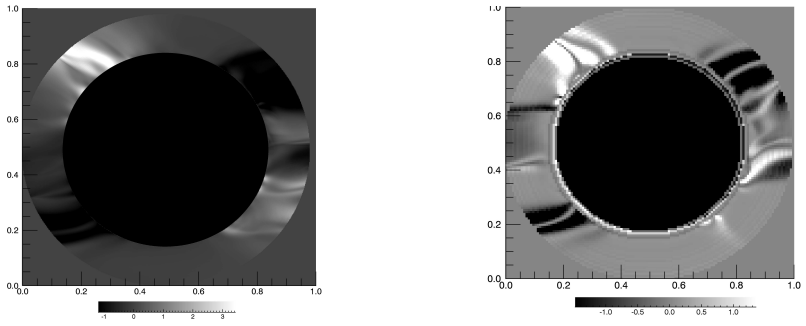

Figure 8.2: Comparison beetween E corona Stokes parameter U obtained by Forward simulation, integrated along the LOS (left) and along the POS (right), both images with the application of the NRGF filter (colours bar units are arbitrary).

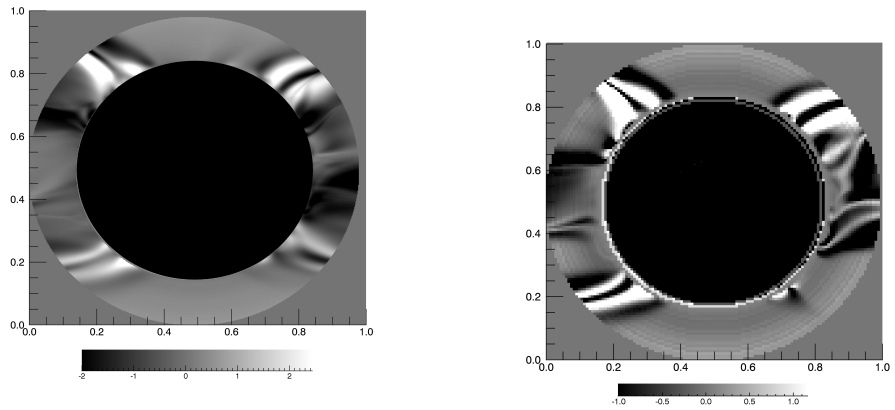

Figure 8.3: Comparison beetween E corona Stokes parameter Q obtained by LOS Forward simulation, (left) and by the POS (right), both images with the application of the NRGF filter (colours bar units are arbitrary).

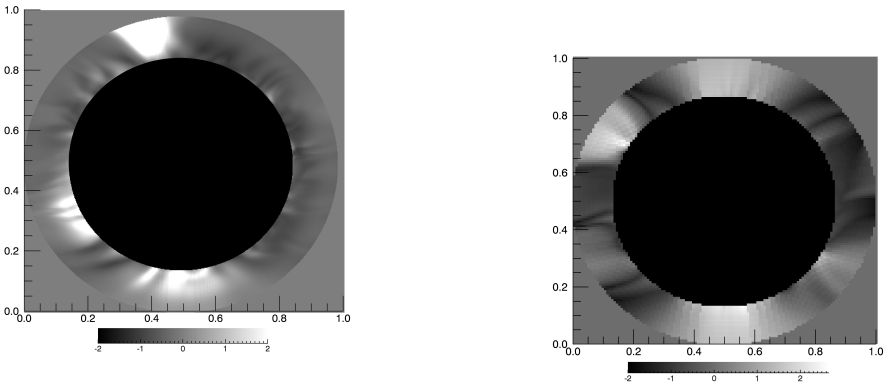

Figure 8.4: Comparison beetween E corona linear polarization p obtained by Forward simulation, integrated along the LOS (left) and along the POS (right), both images with the application of the NRGF filter (colours bar units are arbitrary.

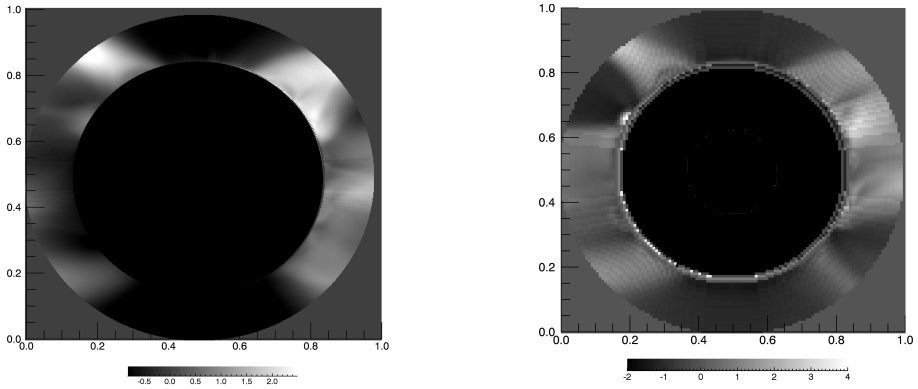

Figure 8.5: Comparison beetween K corona linear polarization p obtainted by Forward simulation, integrated along the LOS (left) and along the POS (right), both with the application of the NRGF filter (colours bar units are arbitrary).

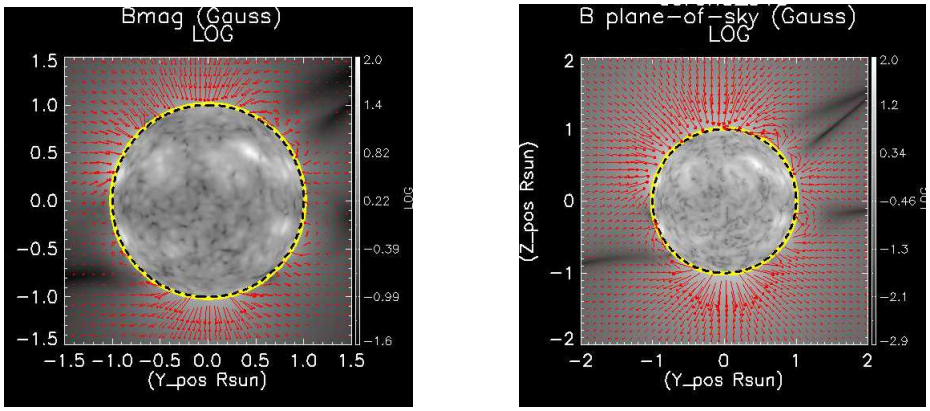

Figure 8.6: Magnetic field lines rappresented by Forward simulation, integrated along the line of sight (left) and along the plane of sky (right).

8.1.2 MHD Model of the Solar Corona

The structure of the solar corona is determined by the outward extension of the Sun's magnetic field. To better understand the large-scale structure of the solar corona and inner heliosphere, it is necessary to map in detail the photospheric magnetic field into the corona and beyond. The Predictive Science team (Predsci web page http://www.predsci.com) are trying to do this working in the large-scale and long-wavelength interaction of the plasma and magnetic fields. The goal of the Predictive science develop research is to bring MHD computations that can not only be used in theoretical studies but as a tool for the analysis of solar and heliospheric data. A self-consistent description of the large-scale solar corona requires the coupled interaction of magnetic, plasma, and solar gravity forces, including the effect of the solar wind.

A *polytropic model*, in which an adiabatic energy equation with a reduced polytropic index γ , is a crude way of modelling the complicated thermodynamics in the corona with a simple energy equation. The primary motivation for using a reduced γ is the fact that the temperature in the corona does not vary substantially [Mikic et al.,1999]. Detailed comparisons of model results with coronal observations indicate that while this one matches many features of the corona , it is not accurate enough to quantitatively reproduce the properties of the corona and solar wind. The MHD model used by the Predsci team includes the physical mechanisms that describe the transport of energy in the corona and solar wind, with the inclusion, in energy equation,of the effects of parallel thermal conduction, radiation loss, parametrized coronal heating and a self-consistent model for Alfven wave acceleration. By comparing MHD solutions with observations it will be possible to test different coronal heating models, and, eventually, after a better understanding coronal heating process, to relate the its source to physical quantities. To develop a realistic model, photospheric magnetic field data during the time of interest is used to specify the boundary condition on the radial magnetic field (Br). Synoptic charts are generated from measurements at the Wilcox Solar Observatory or the National Solar Observatory at Kitt Peak. They plan in the future to use data from the SOI/MDI instrument aboard the SOHO spacecraft. The measured photospheric magnetic field, together with a uniform assumed density and temperature at the photosphere, is used to solve the MHD equations to steady state in the corona, expressing the self-consistent interaction of the solar wind with the coronal plasma. The three-dimensional simulation

is carried out on a Cray YMP/C90 supercomputer. Predsci gives a prediction of the properties of the coronal plasma (magnetic field, density, temperature, and flow velocity). The distribution of pB in the plane of the sky is proportional to the line-of-sight integral of the product of the electron density and a scattering function. Using the plasma density from their model, they generate a pB image to simulate an eclipse image. These images can then be compared to the observative data. To predict the structure of the corona prior to an eclipse, they typically use magnetic field data that is about a month old. During solar minimum, the magnetic field on the Sun changes relatively slowly daily so a prediction of the large-scale structure of the solar corona a month can to provide a quite reasonable forecast of the solar corona.

8.1.3 Prediction of the Structure of the Solar Corona during the July 11, 2010 Total Solar Eclipse

In prevision of the eclipse on July 2nd, 2010, Predictive Science started an MHD computation of the solar corona. The Predsci group used a photospheric magnetic field data for Carrington rotation 2097, measured up to June 16, 2010, using the MDI magnetograph aboard the SOHO spacecraft and also magnetic field measurements from the Wilcox Solar Observatory at Stanford University and the National Solar Observatory SOLIS vector magnetograph at Kitt Peak. They used their MHD model for the first time to predict the structure of the corona prior to the March 29, 2006 total solar eclipse.

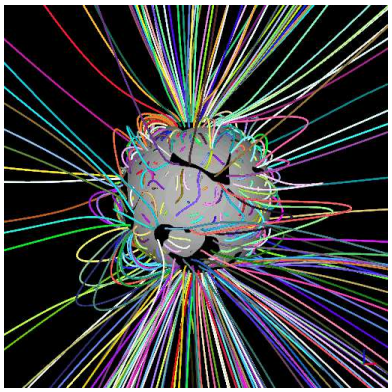

Figure 8.7: Predicted magnetic field lines in the solar corona for the eclipse expected on July 11, 2010 with also surface lines.

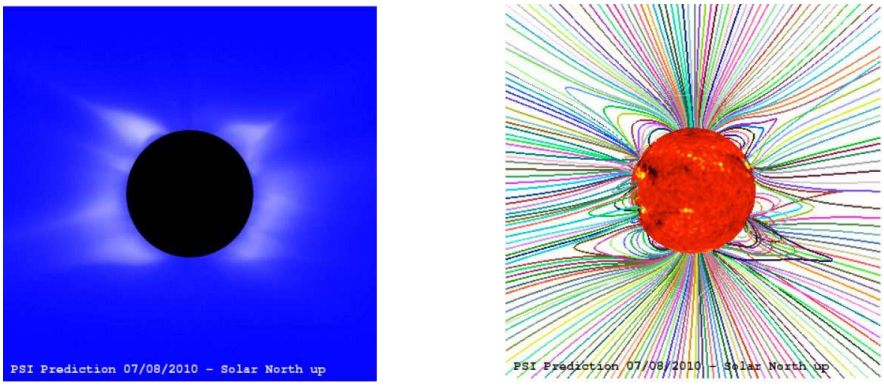

Figure 8.8: Predicted K corona polarization brightness (top) together with traces of the magnetic field lines in the solar corona (bottom) for the eclipse expected on July 11, 2010 at 19:33 UT (with terrestrial north up). The Sun's surface shows color contours of the radial component of the measured photospheric magnetic field from the MDI magnetograph.

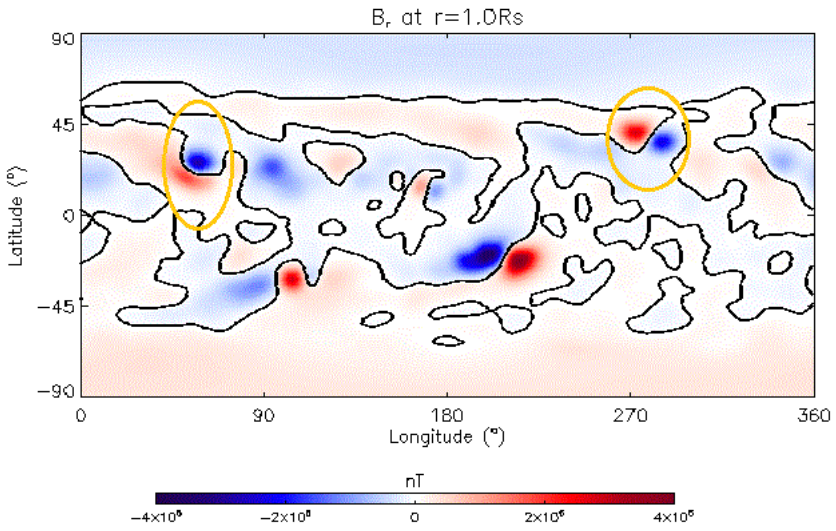

Figure 8.9: Predicted surface magnetogramm in the solar corona for the eclipse expected on July 11, 2010 at 18:00 UT.

The location of the active regions highlighted in the magnetogramm (Figure 8.9) correspond to the one of the two regions visible in SDO/AIA images (Figure 7.28).

8.1.4 Simulations of SDO/AIA observations

The same model was used for global MHD simulations relevant to the SDO mission. Simulations are all based on a specific Carrington[2] rotation. Photospheric magnetic field synoptic map is built up from a sequence of observations centered at central meridian over a 27 day period. This map forms the fundamental boundary condition at the surface of the Sun, and is supplemented with auxiliary boundary conditions that approximate the plasma density and temperature. The MHD model used for these simulations (Figures from 8.10 to 8.12)is called hmi_mast_std_0101. It is based on the heating model of [Lionello et al., 2009]in this model coronal holes are wider/more open than in others one and active regions aren't as visible due to the properties of the magnetic maps and heating model itself at this resolution.

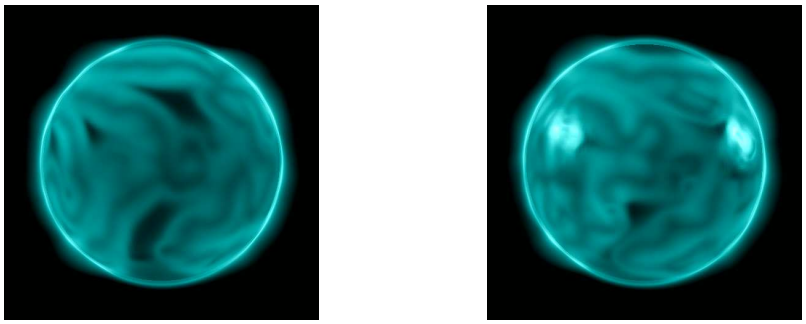

Figure 8.10: Predsci simulation of AIA 131 observation at the Carrigton rotation 2098 of the day of the eclipse(left) and at the next one (right).

[2]The number of rotations of the Sun's surface (as seen from the Earth) since November 9, 1853. The mean period for a single rotation of the Sun as seen from the Earth is 27.2753 days.

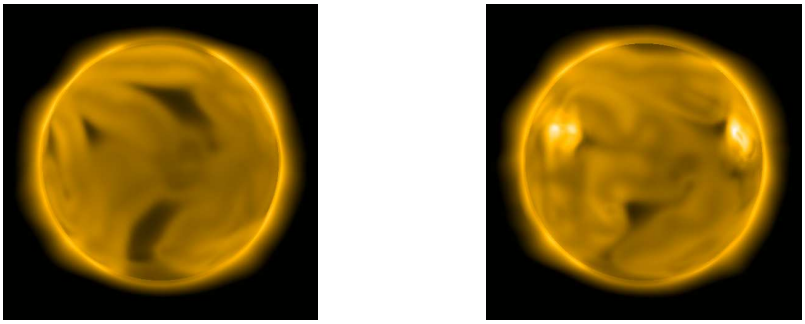

Figure 8.11: Predsci simulation of AIA 171 observation at the Carrigton rotation 2098 of the day of the eclipse(left) and at the next one (right).

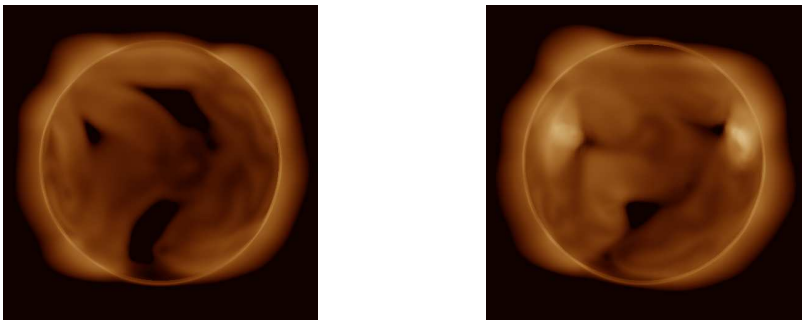

Figure 8.12: Predsci simulation of AIA 193 observation at the Carrigton rotation 2098 of the day of the eclipse(left) and at the next one (right).

Chapter 9

Comparison between observations and simulations

9.1 Introduction

As mentioned in the previous chapter, the use of numerical simulations allows to the testing of new theories against an observable that is directly sensitive to the magnetic field in the corona. Additionally, numerical simulations permits comparison between the models themselves.
In this chapter differences and similarities between simulations and observational eclipse images and between simulations themselves will be analysed . In particular:

- CorMag E and K corona Stokes' profiles vs Forward simulations;
- CorMag K corona Pb image vs Predsci simulation;
- Forward representation of magnetic field lines vs Predsci simulations;
- SDO/AIA observations vs Predsci simulations.

9.2 CorMag data vs Forward simulations

In order to compare observation data with images obtained by the Forward simulation it's necessary to consider that in the CorMag LCTF the analyser is not parallel to the x axis,

as in the ideal case discussed in chapter 7, but tilted by 43° with respect to the x axes (Figure 9.1), so the modulation matrix is not the same of Eq. 4.5.

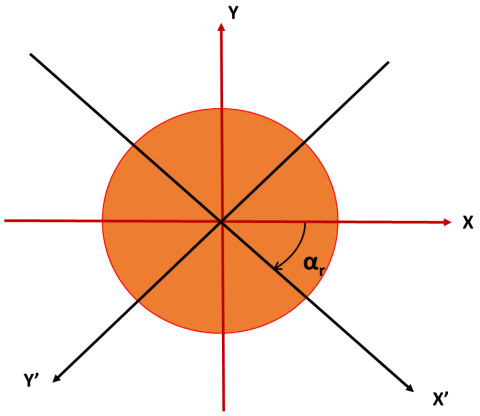

Figure 9.1: Frame coordinate system (Red) and analyzer reference system (Black). The second one is rotated of α_r= 43°with respect to the first.

This way, in order to prepare observational data for the comparison with simulation, its necessary to follow this procedure:

1. Calculate the Mueller matrix for the rotated LCP'(with included first LCTF polariser):

$$M_{LCTF}(\delta) = M_{rot}(-2\theta) \cdot M_{LCP'}(\delta) \cdot M_{rot}(2\theta) =$$
$$M_{rot}(-2\theta) \cdot [M_{POL}(0) \cdot M_{LCP}(\delta)] \cdot M_{rot}(2\theta) =$$
$$= M_{rot}(-2\theta) \cdot [M_{POL}(0) \cdot M_{LCVR}(\delta) \cdot M_{QWLR}(\pi/2)] \cdot M_{rot}(2\theta)$$

   where

$$M_{rot}(2\theta) = \begin{pmatrix} 1 & 0 & 0 & 0 \\ 0 & cos(2\theta) & sin(-2\theta) & 0 \\ 0 & -sin(-2\theta) & cos(2\theta) & 0 \\ 0 & 0 & 0 & 1 \end{pmatrix} \tag{9.1}$$

   is the Mueller matrix of a rotating element,

From equations 4.1-4.4 and 9.1 $M_{LCTF}(\delta)$ is given by:

$$M_{LCTF}(\delta) = \begin{pmatrix} 1 & -sin\delta & cos\delta & 0 \\ 1 & -sin\delta & cos\delta & 0 \\ 0 & 0 & 0 & 0 \\ 0 & 0 & 0 & 0 \end{pmatrix} \tag{9.2}$$

2. Replace the first row of Mueller matrix obtained in the previous step $[1, -sin\delta, cos\delta, 0]$ in the nominal modulation matrix (Eq. 4.5), with δ=0°,-120°,-240°.
   We consider the first row because the only direct measure we made with the CorMag instrument is the intensity of the incident radiation.

3. Obtain Stokes' parameters images from the new modulation matrix, following the same procedure of Eq. 7.1-7.2-7.4-7.5 and then the polarization angle β (Eq. 3.12) and the degree of linear polarization p given by equation 3.13, where pB $\equiv$ pI;

4. Rotate the image around the x-axis (Figure 9.1), to take into account their reversal by the optics of the instrument;

To follow Stokes' s parameters images obtained with the this procedure (Figures from 9.2 to 9.4):

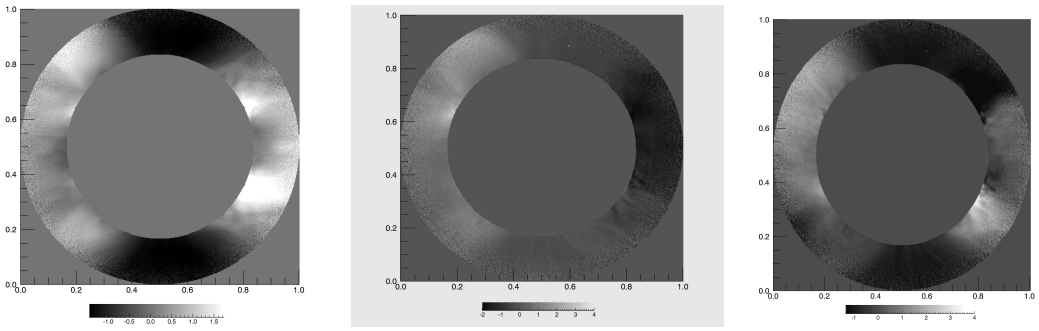

Figure 9.2: E corona Stokes' parameter I (left), Q (centre) and U (right), all images with the application of the NRGF filter (colours bar units are arbitrary).

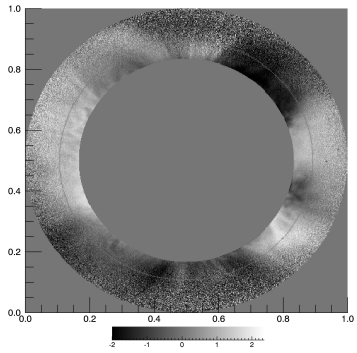

Figure 9.3: E corona polarized brightness, with the application of the NRGF filter (colours bar units are arbitrary).

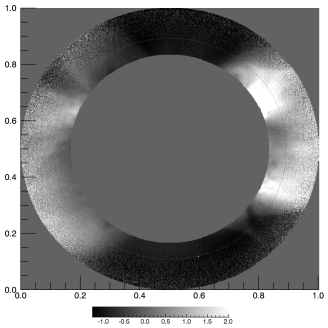

Figure 9.4: K corona polarized brightness, with the application of the NRGF filter (colours bar units are arbitrary)..

Now it's possible to compare them with the corresponding the forward simulations outputs (Figures from 9.5 to 9.9):

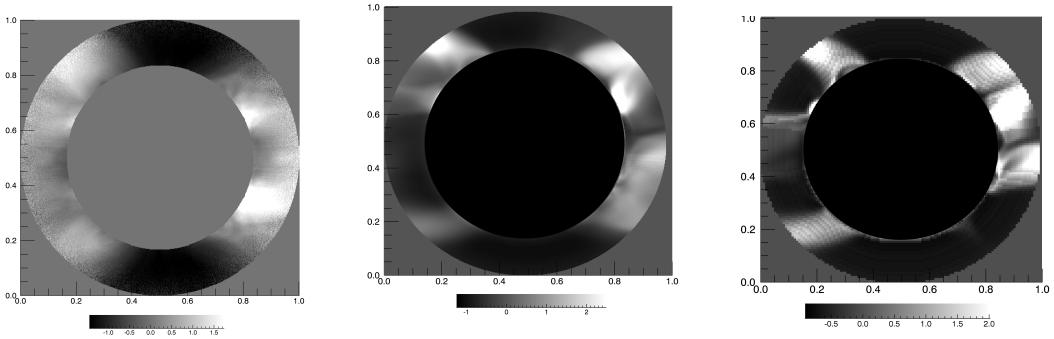

Figure 9.5: E corona Stokes' parameter I: CorMag (left), FORWARD LOS (centre), FORWARD POS (right), with the application for each image of the NRGF filter (colours bar units are arbitrary).

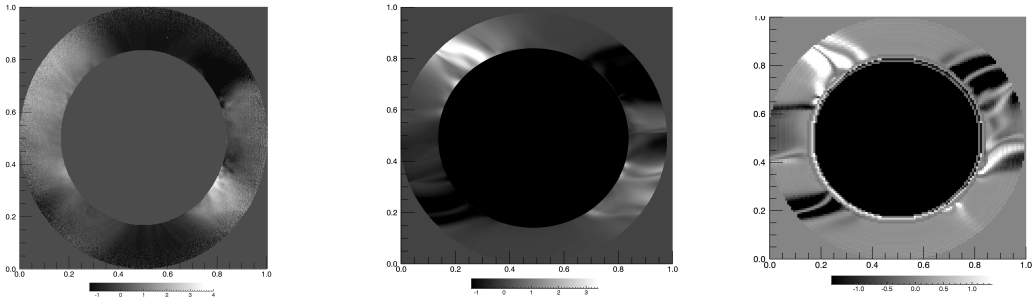

Figure 9.6: E corona Stokes' parameter U: CorMag (left), FORWARD LOS (centre), FORWARD POS (right), with the application for each image of the NRGF filter (colours bar units are arbitrary).

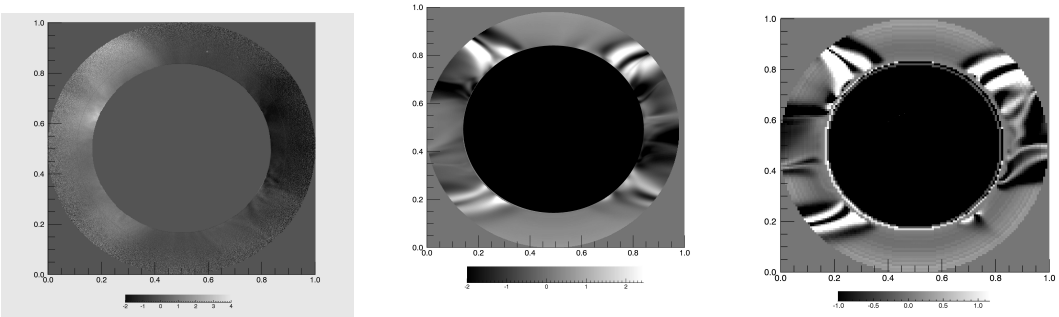

Figure 9.7: E corona Stokes' parameter Q: CorMag (left), FORWARD LOS (centre), FORWARD POS (right), with the application for each image of the NRGF filter (colours bar units are arbitrary).

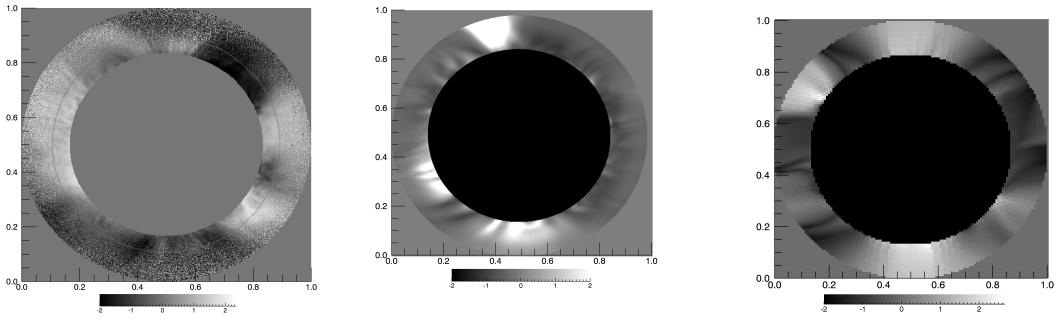

Figure 9.8: E corona polarized brightness: CorMag (left), FORWARD LOS (centre), FORWARD POS (right), with the application for each image of the NRGF filter (colours bar units are arbitrary).

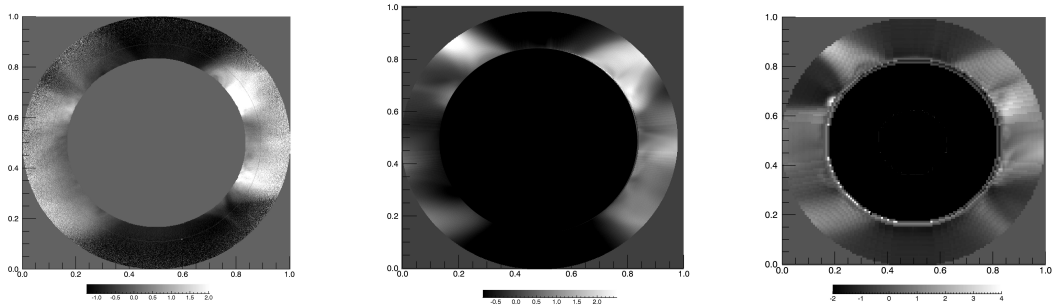

Figure 9.9: K corona polarized brightness: CorMag (left), FORWARD LOS (centre), FORWARD POS (right), with the application for each image of the NRGF filter (colours bar units are arbitrary).

It's evident, from these comparisons that there is an accord between observations and simulations, for large scale morphologies, especially using the integration along the light of sight.

With this kind of integration (LOS) the model is able to reproduce better large scale structure than small scale ones[1]. Model improving are needed for small scale structures.

The observed coronal cavity, just above the north-west limb, is not reproduced in Forward simulations because NumCube model oes not include transient (i.e., less then a solar rotation, 27 days) structures like coronal cavities around prominences (Figure 9.10).

[1] About 1 arcmin $\sim$ 40M.

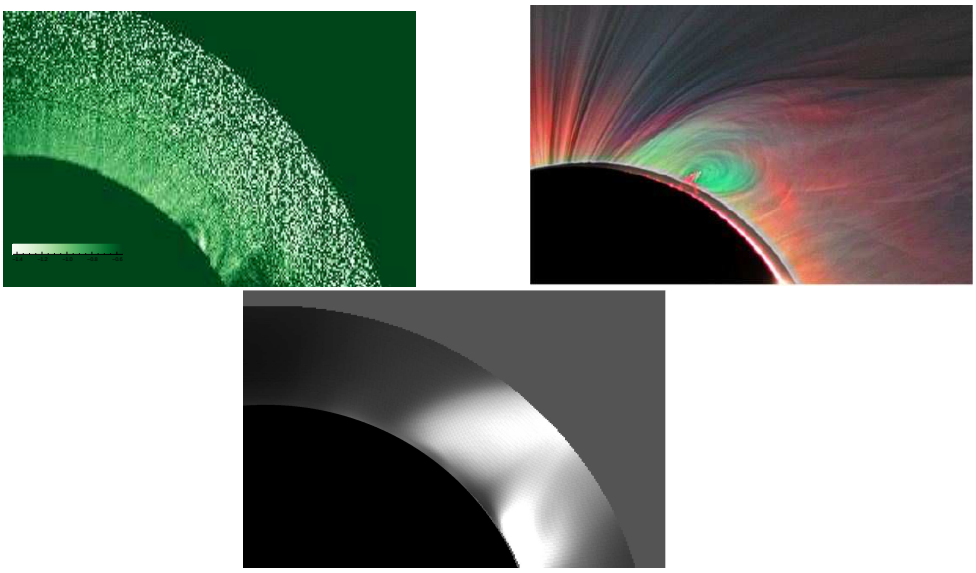

Figure 9.10: Focus on the observed region above the north-west limb in FeXIV line (box 2 Fig.7.17): Cormag E corona I image (top-left),high resolution E corona I image (top-right), FORWARD I image output (bottom).

9.3 CorMag K corona polarized brightness vs Predsci predictions.

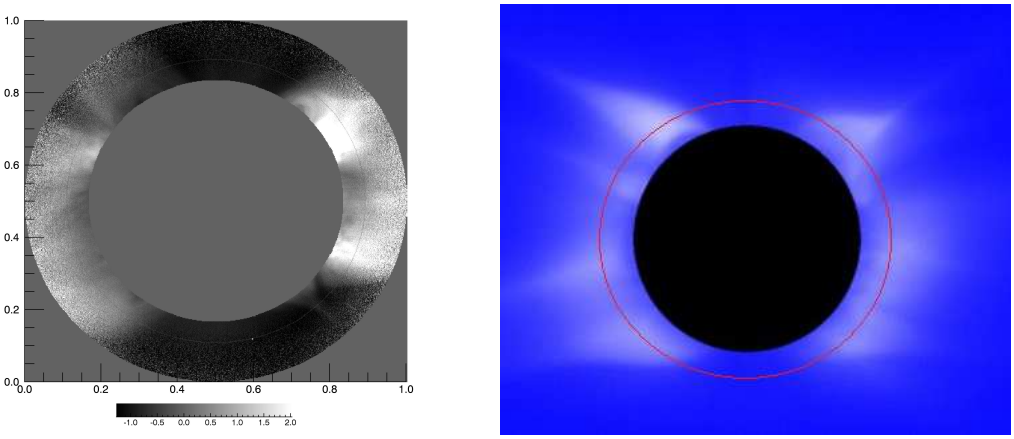

Figure 9.11: K corona polarized brightness: CorMag (left), Predsci(right).

This two images (Figure 9.11)show a reasonable agreement between observation and simulation especially for large scale structures.

9.4 Forward vs Predsci magnetic field lines representation.

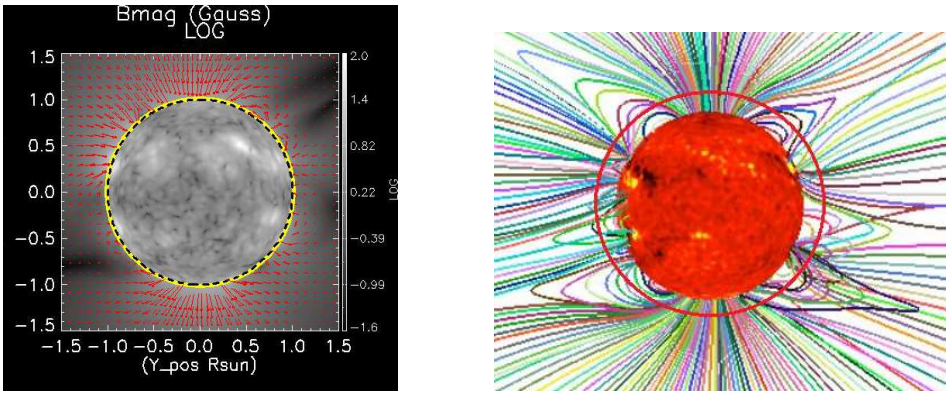

Figure 9.12: K corona polarized brightness: CorMag (left), Predsci(right).

The two different representations of the same magnetic field model (Figure 9.12), respectively FORWARD and PredSci, show a good agreement on the large scale trend of the magnetic field lines. In both simulations are present closed field lines in correspondence of the cavity and of the active regions.

9.5 SDO/AIA observations vs Predsci predictions.

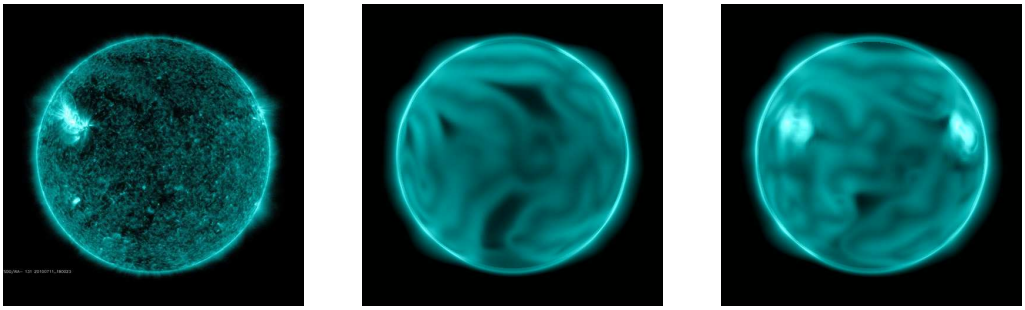

Figure 9.13: Comparison between: AIA 131 observation of the day of the eclipse (left), Predsci simulation at the Carrigton rotation 2098(centre) and at the next one rotation (right),.

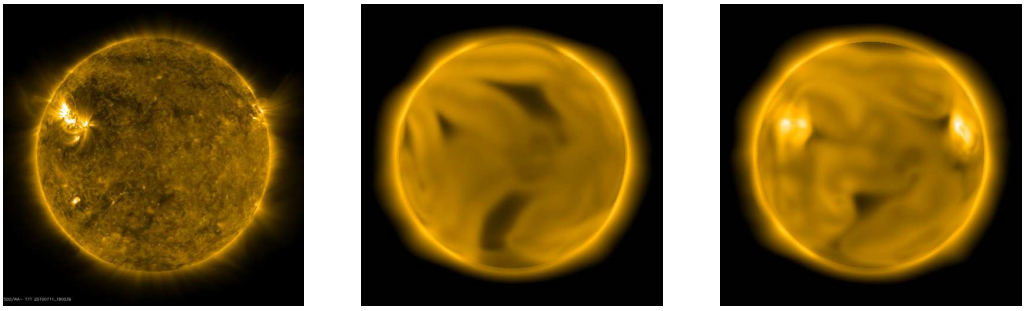

Figure 9.14: Comparison between: AIA 171 observation of the day of the eclipse (left), Predsci simulation at the Carrigton rotation 2098(centre) and at the next one rotation (right).

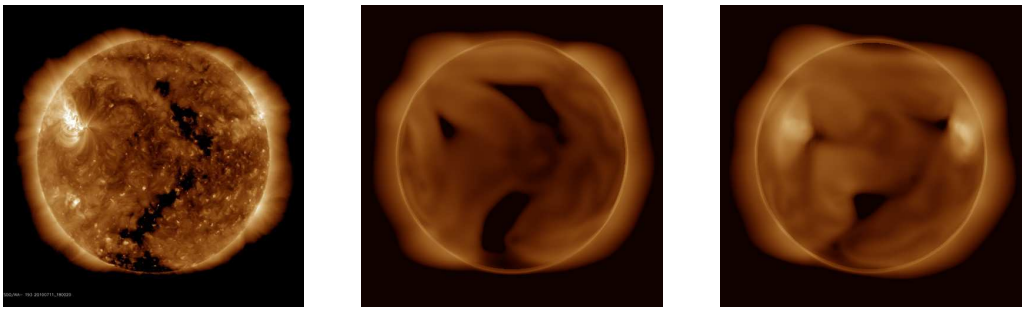

Figure 9.15: Comparison between: AIA 193 observation of the day of the eclipse (left), Predsci simulation at the Carrigton rotation 2098(centre) and at the next one rotation (right).

From the comparison between observations and simulations in figures from 9.13 to 9.15 it is possible to highlight some important things, probably due to the heating model used [Lionello et al., 2009]:

- Coronal holes positions in SDO/AIA observations match quite well with the ones in Predsci simulations at the Carrington rotation 2098 (rotation of the day of the eclipse).
- In Predsci simulations at the Carrington rotation 2098 there are no active regions.
- In the simulation at the Carrington rotation 2099 are present two active regions placed in correspondence of the ones observed in SDO/AIA data, but coronal hall are less extended then during the previous Carrington rotation.

Conclusions

The work of this thesis consisted in the analysis of the polarimetric observations of the line-emission from Fe^{+13} ions in corona: the coronal "green line", FeXIV 530.3 nm.
The observations where carried out during the total solar eclipse of 2010 July 11, with a coronal Magnetograph (CorMag). Polarimetric observations of coronal emission lines such as the "green line", is an important tool for the diagnostics of the coronal magnetic field. The polarization by resonance scattering of the coronal emission lines is modified, through the Hanle effect, by the presence of the magnetic field.
From the analysis of the 2010 eclipse polarimetric images of the Fe XIV coronal line, the results of this thesis work shows:

- The presence of the Hanle effect in the line-emission of the Fe^{+13} ions in coronal plasma surrounding a prominence.

This thesis reports the first detection of the Hanle effect in a coronal forbidden line-emission observed during an eclipse with an electro-optical spectro-polarimeter.
SDO/AIA observations, for the day of the eclipse, show the presence of a coronal cavity (Figure 7.30), above the north-ovest limb, in correspondence with the one observed by the CorMag instrument (Figures 7.9-7.17). Different SDO/AIA filters corresponds to different temperatures (Figure 7.27).
Addictional results:

- The comparison of the low resolution (12.6 ") K and E corona CorMag images with the high resolution (1") shows a good agreement between large scale structures (Figures 7.9 and figure 7.17).

- Forward-modelling numerical simulations are in reasonable agreement with the observed global coronal morphology of the magnetic field. Interesting differences between forward modelling and observational data in small scale coronal structures (about 1 arcmin $\sim$ 40Mm) suggest the presence of a non force-free magnetic fields in those structures (e.g.,"cavities")(Figure 7.17).

The data reduction yielded observational parameters that can be used, such as the line emission polarization vector direction, to constrain theoretical models of the magnetic field of small scale structures .

- In the forward-modelling simulations, the coronal cavity, highlighted in CorMag and SDO/AIA observations above the north-west limb is not reproduced. Models does not include transient (i.e., less then a solar rotation, 27 days) structures like coronal cavities around prominences (Figure 9.10).

- The presence of two active regions on the surface of Sun at the time of the eclipse (Figure 7.28), is also reproduced by the Predictive Science surface magnetogramm (Figure 8.9). In this magnetogramm there are two other active regions that are not visible in the eclipse in that are on the anti-meridian view. It's also important to remember that the extrapolated photopheric magnetic field employs as boundary condition a magnetogram averaged over a Carrigton rotation (par. 8.1.3), so it does not represent the same configuration at the moment of the eclipse.

Future works

The quite-good agreement between simulated coronal structure and observations on a global scale represent a significant validation of the forward-modelling approach to interpret the observations of the Hanle effect. This approach will be refined in future work where forward-modelling of line emission polarization from small scale structures, such as cavities, will be used to test different magnetic field models against the polarimetric parameters derived in this thesis work from the eclipse observations.

Ringraziamenti

Vorrei ringraziare il mio relatore, il dott. S. Fineschi, per avermi guidata pazientemente durante questo anno di lavoro di tesi, permettendomi di accrescere di giorno in giorno le mie conoscenze e le mie competenze professionali.
Ringrazio inoltre i miei correlatori, il dott. A. Bemporad ed il dott. G. Capobianco per i loro indispensabile supporto, la loro disponibilità e per i consigli che mi hanno dato.
Un ringraziamento particolare va anche a G. Massone per il suo aiuto prezioso in laboratorio ed a tutto lo staff OaTo per la gentilezza mostrata in questi mesi e per avermi fatta sentire fin da subito parte del gruppo.
Il mio grazie va alla mia amata famiglia per avermi sempre permesso di seguire le mie ambizioni, nonostante mi abbiano portato lontano da casa e per tutto l'amore ed il sostegno che riesce a darmi ogni giorno.
Un altro enorme grazie va ad Emanuele per essere stato sempre al mio fianco in questa lunga avventura, aiutandomi a rialzarmi ed a combattere nei momenti difficili.
Ringrazio i miei amici e compagni di viaggio Daria e Lorenzo che mi hanno aiutato ad affrontare questi anni di studio con il sorriso sulle labbra e tutte le persone meravigliose che questa esperienza torinese mi ha dato la fortuna di incontrare.
Grazie ai miei carissimi amici Alessandra, Christian, Emanuele, Emilio, Gianvito, Giuseppe, Mariarita e Sonia, voi con il vostro continuo appoggio ed incoraggiamento siete stati per me la dimostrazione che l'amicizia è più forte della distanza e del tempo.
Ed infine grazie a chi non c'è più, ma è sempre presente nel mio cuore.

Bibliography

Alazraki, G. and Couturier, P., 1971, "Solar Wind Accejeration Caused by the Gradient of Alfvn Wave Pressure", Astron. Astrophys., 13, 380389.

Alissandrakis, C.E., 1981, "On the Computation of Constant Force-free Magnetic Field", Astron. Astrophys., 100, 197200.

Avrett Eugene H.,"Introduction to Non-LTE Radiative Transfer and Atmospheric Modeling", Harvard-Smithsonian Center for Astrophysics, 2008.

Balboni E.,"Corona Solare: Parametri fisici derivati dalle osservazioni svolte durante l'eclisse del 26/03/2006", Tesi di laurea magistrale, 2009.

Bemporad A., Presentation for the 3rd-ISSI Team Meeting, Bern, 2014.

Bineau, M., 1972, "On the Existence of Force-Free Magnetic Fields", Commun. Pure Appl. Math., 25, 7784.

Bland-Hawthorn J., W. van Breugel,P. R. Gillingham, I. K. Baldry and D. H. Jones, "A Tunable Lyot Filter at Prime Focus: a Method for Tracing Supercluster Scales", The Astrophysical Journal, 563:611–628, 2001 December 20.

Bogdan, T. J., Carlsson M., Hansteen V. H., McMurry A., Rosenthal C. S., Johnson M., Petty-Powell S., Zita E. J., Stein R. F., McIntosh S. W., Nordlund A,"Waves in the Magnetized Solar Atmosphere. II. Waves from Localized Sources in Magnetic Flux Concentrations", APJ, 2003

Bueno J. T., Ramos A. and Shchukina N., "The Hanle Effect in Atomic and Molecular Lines: A New Look at the Suns Hidden Magnetism"arXiv preprint astro-ph/0612678, 2006.

Bueno J. T, Asensio Ramos A. and Shchukina N., "The Hanle Effect in Atomic and Molecular Lines: A New Look at the Suns Hidden Magnetism", ASP Conference Series, Vol. 358, pages 269–292, 2006.

Bueno J. T, "Atomic polarization and the Hanle effect ", arXiv preprint astro-ph/0202328, 2002.

Capobianco G., "Valutazione degli effetti della nuvolosit sui dati acquisiti durante leclisse totale di Sole dell11 luglio 2010 ", Technical Report nr.150, 2011.

Capobianco G., Massone G., Fineschi S. , "Technical description of the CorMag Instrument ",Technical Report nr.153, 2011.

Capobianco G., "CorMagICS 1.0 CorMag Instrument Control Software", OATo Technical Report nr. 142, 2010.

Capobianco G., Massone G., Zangrilli L., Fineschi S.,"High precision monochromator calibration in the visible region ot the wavelength spectra ", Technical Report nr. 130, 2010.

Casini R. and Judge P. G., "Spectral Lines For Polarization Measurements Of The Coronal Magnetic Field. Consistent Treatment Of The Stokes Vector For Magnetic-Dipole Transitions.",THE ASTROPHYSICAL JOURNAL, 522:524–539, 1999 September 1.

Chiu Y.T. and Hilton H., 1977, "Exact Greens function method of solar force-free magnetic-field computations with constant α. I. Theory and basic test cases", Astrophys. J., 212, 873885.

Druckmuller M., Rusin V. & Minarovjech M., 2006, Contrib. Astron. Obs. Skalnate Pleso,36,3.

The identification of coronal lines, 1954.

Elmore D. F.,Card G. L., Lecinski A. R., Lites B. W. , Streander K. V. and Tomczyk S.,"Calibration Procedure for the Polarimetric Instrument for Solar Eclipse 98", Proceedings of SPIE Vol. 4139 (2000).

Espenak, F. and Anderson J., Annular and Total Solar Eclipses of 2010, NASA TP2008-214171, Goddard Space Flight Center, Greenbelt, MD, 2008.

Fan Y. and Gibson S. E. (2006),"On the nature of the x-ray bright core in a stable filament channel", Astrophys. Journ. Lett., 641, 149

Feng W. , Ji Y., Chen L., "The impact of signal–noise ratio on degree of linear polarization measurement",Optik 124 (2013) 192–194.

Ferrari A. "Stelle, galassie e universo ",Springer-Verlag Italia, 2011.

Fineschi S., Capobianco G., Massone G., Baur T., Bemporad A., Abbo L., Zangrilli L., Dadeppo V., "Liquid Crystal Lyot Filter for Solar Coronagraphy",Proc. of SPIE Vol. 8148, 2011.

Fineschi S., Massone G., Capobianco G., Benna C., Calcidese P., Romoli M.,Casetti L., Abbo L., Bemporad A., "Total Solar Eclipse of July 11th, 2010: Data Log and Raw Images ", Report 144, 2010.

Fineschi S., Baur T. and Wagner P."Tunable Filter Test Report", 2010.

Fuller J., Gibson S. E., "A SURVEY OF CORONAL CAVITY DENSITY PROFILES", The Astrophysical Journal, 700:1205–1215, 2009 August 1

Gary G.A., 2001,"Plasma beta above a solar active region: Rethinking the paradigm", Solar Phys., 203, 7186.

Gibson S. E., Kucera T. A., Rastawicki D., Dove J., de Toma G., Hao G., Hill S., Hudson H. S., Marque H. S., McIntosh P. S., Rachmeler L., Reeves K. K. , Schmieder1 B., Schmit D. J., Seaton D. B., Sterling A. C., Tripathi D., William D. and Zhang M.,"Three–Dimensional Morphology Of A Coronal Prominence Cavity", The Astrophysical Journal, 724:1133–1146, 2010 December 1

Gibson S. , Foster D., Burkepile J., de Toma G.and Stanger A., "The Calm before the Storm: The Link between Quiescent Cavities and Coronal Mass Ejections", The Astrophysical Journal, 641:590–605, 2006 April 10.

Golub L., Pasachoff Jay M., "The Solar Corona ",Cambridge University Press, 2010. Phys., 138, 233

Grotrian W., Zur Frage der Deutung der Linien im Spektrum der Sonnenkorona. Naturwissenschaften, 1939.

Habbal S. R., Druckmuller M., Morgan H., Ding A., Johnson J., Druckmullerova H., Daw A., Arndt M. B., Dietzel M. and Saken J., "Thermodynamics Of The Solar Corona And Evolution Of The Solar Magnetic Field As Inferred From The Total Solar Eclipse Observations Of 2010 July 11 ", The Astrophysical Journal, 734:120 (18pp), 2011 June 20.

Hanle W., "The magnetic influence on the polarization of resonance fluorescence", Z. Physik 30, 93 (1924).

Hecht E., Theory and problems of optics, 1975

Holman G. ,"What goes up, first comes down",2005-11-21.

House L., "The Theory Of The Polarization Of Coronal Forbidden Lines",Pub. Astron. Soc. Pacific, Volume 86, August 1974.

Ignace R., Cassinelli J. P. and Nordsieck K. H., "The Hanle effect as a diagnostic of magnetic fields in stellar envelopes: some theoretical results for resolved line profiles ", AJ, 520:335–346, 1999 July 20.

Jenkins J. L., "The Sun and How to Observe it", Springer-Verlag Italia 2010.

Janesick J. R., "Photon transfer DN to λ", The Society of Photo-Optical Instrumentation Engineers, 2007.

Judge P. G., Low B. C. and Casini R., "Spectral Lines For Polarization Measurements Of The Coronal Magnetic Field. V. Information Content Of Magnetic Dipole Lines", The Astrophysical Journal, 662:677–690, 2007 June 10.

Judge L.P. G., Casini R., Tomczyk S., Edwards D. P. and Francis E., "Coronal magnetometry: A feasibility study", High Altitude Observatory, National Center for Atmospheric Research, 2001.

Judge P. G.,"Spectral Lines For Polarization Measurements Of The Coronal Magnetic Field. I. Theoretical Intensities",THE ASTROPHYSICAL JOURNAL, 500:1009 –1022, 1998 June 20

Krebs O., Maletinsky P., Amand T., Urbaszek B.,Lematre A., Voisin, Marie X. and Imamoglu A.,"Anomalous Hanle Effect in Quantum Dots : Evidence for Strong Dynamical Nuclear Polarization in Transverse Magnetic Field", arXiv:0910:1744vl, 2009.

Kucera A., Ambroz J., Glomory P., Kozak M. and Rybak J. "CoMP–S the Coronal Multi-Channel Polarimeter for Slovakia", Contrib. Astron. Obs. Skalnate Pleso 40, 135–138, (2010).

Lagg A., Woch J., Krupp N., and Solanki S. K.,"Retrieval of the full magnetic vector with the He I multiplet at 1083 nm :Maps of an emerging flux region", A&A 414, 1109–1120 (2004).

Landi Degli Innocenti E., "Fisica Solare ",Springer-Verlag Italia, Milano 2008.

Lemen J. et al., "The Atmospheric Imaging Assembly (AIA) on on the Solar Dynamics Observatory (SDO) ", Solar Physics, January 2012, Volume 275, Issue 1-2, pp 17-40.

Lin H., Solar-C Science Definition Meeting,"Observations and Observational Test of Coronal Magnetic Fields", ISAS, JAPAN Solar Dynamics Observatory (SDO) , 22 April 2011.

Lionello R., Linker J. A., & Mikic Z., 2009, ApJ, 690, 902

Mierla M., Schwenn R., Teriaca L., Stenborg G. and Podlipnik B., "Analysis of the Fe X and Fe XIV line width in the solar corona using LASCO-C1 spectral data", A&A 480, 509–514 (2008).

Mikic Z., Linker J. A., Schnack D., Lionello R., and Tarditi A.,"Magnetohydrodynamic modeling of the global solar corona", PHYSICS OF PLASMAS, 1999.

Morgan H., Habbal S. R., "Solar maximum streamers as thin twisting sheets", International Symposium on Solar Physics and Solar Eclipses (SPSE), 2006.

Morgan H., Habbal S. R. and R. Woo, "The depiction of coronal structure in white-light images", Solar Physics, vol. 236, no. 2, pp. 263272, 2006.

Moran T. G.,"Solar And Heliospheric Observatory/Large Angle Spectrometric Coronagraph Polarimetric Calibration ",Solar Physics (2006) 237: 211–222.

Oran R., van der Holst B., Landi E., Jin M., Sokolov I. V. and Gombosi T. I.,"A global wave driven magnetohydrodynamic solar model with a unified treatment of open and closed magnetic field topologies ", The Astrophysical Journal, 778:176 (20pp), 2013 December 1.

Peter H.,"On the nature of the transition region from the chromosphere to the corona of the Sun", A&A 374, (2001)

Predictive Science web page http://www.predsci.com

Rachmeler L. A. , Gibson S. E., Dove J. B., Devore C. R., and Fan Y., "Polarimetric Properties of Flux Ropes and Sheared Arcades in Coronal Prominence Cavities,"Solar Physics, vol. 288, no. 2, pp. 617636, Dec. 2013.

Shurcliff W. A.,"Polarized Light", Cambridge, Massachusetts, 1962.

Sivaramakrishnan A. et al., "Ground-based Coronagraphy with High-order Adaptive Optics", The Astrophysical Journal, 552:397–408, Nonlinear Processes in Geophysics, 2001 May 1.

SolarSoft web page http://www.lmsal.com/solarsoft/

Stenflo J. O., "What can we learn about the corona from polarization measurement?", ASP Conference Series, Vol. 205, 2000.

van the Hulst,"The electron density of the solar corona ", Astronomical Institutes of the Netherlands, 1950.

Wiegelmann T., Sakurai T., "Solar Force-free Magnetic Fields",Living Rev. Solar Phys., 9, (2012), 5.

Withbroe G. L.and Noyes R. W.", Mass and Energy Flow in the Solar Chromosphere and Corona", Annual Review of Astronomy and Astrophysics Vol. 15: 363-387 (Volume publication date September, 1977).